Forschungszentrum Karlsruhe
in der Helmholtz-Gemeinschaft

Wissenschaftliche Berichte
FZKA 7440

Calibrated Measurements of the Radio Emission of Cosmic Ray Air Showers

S. Nehls

Institut für Kernphysik

November 2008

Forschungszentrum Karlsruhe

in der Helmholtz-Gemeinschaft

Wissenschaftliche Berichte

FZKA 7440

Calibrated Measurements of the Radio Emission of Cosmic Ray Air Showers

Steffen Nehls

Institut für Kernphysik

Von der Fakultät für Physik der Universität Karlsruhe (TH) genehmigte Dissertation

Forschungszentrum Karlsruhe GmbH, Karlsruhe

2008

Forschungszentrum Karlsruhe GmbH
Postfach 3640, 76021 Karlsruhe

Mitglied der Hermann von Helmholtz-Gemeinschaft
Deutscher Forschungszentren (HGF)

ISSN 0947-8620

urn:nbn:de:0005-074409

Calibrated Measurements of the Radio Emission of Cosmic Ray Air Showers

Zur Erlangung des akademischen Grades eines
DOKTORS DER NATURWISSENSCHAFTEN
bei der Fakultät für Physik der
Universität Karlsruhe (TH)

genehmigte

DISSERTATION

von

Dipl. Phys. Steffen Nehls
aus Osterburg

Tag der mündlichen Prüfung: 04.07.2008
Referent: Prof. Dr. J. Blümer, Institut für Experimentelle Kernphysik
Korreferent: Prof. Dr. W. de Boer, Institut für Experimentelle Kernphysik

Zusammenfassung

Kalibrierte Messungen der Radiostrahlung von Luftschauern der Kosmischen Strahlung

Die vorliegende Arbeit untersucht die Eigenschaften der Radiostrahlung von Luftschauern, im Besonderen durch die Rekonstruktion der Lateralverteilung der Radiostahlung von Schauer zu Schauer. Das LOPES Experiment mißt die Radiostrahlung im Frequenzbereich von 40–80 MHz im Koinzidenzbetrieb mit dem Luftschauerexperiment KASCADE-Grande. Für die präsentierte Analyse wurde ein Datensatz verwendet, der mit Ost-West orientierten Radioantennen aufgenommen wurde. Durch Auswahl der höchstenergetischen Luftschauer können die eintreffenden kurzen Radiopulse gemessen und die Lateralverteilung des Luftschauers rekonstruiert werden. Basierend auf einer Amplitudenkalibration des Radiosignals für jede Antenne können die Absolutewerte der Feldstärken bestimmt werden. Die Größen Skalenparameter R_0 und Feldstärke ϵ_0 können aus der Lateralverteilung ermittelt werden. Der wahrscheinlichste Wert für den Skalenparameter ergab $R_0 \approx 125$ m und keine signifikanten Abhängikeiten mit Luftschauerparametern, wie Schauerrichtung oder Primaärenergie, konnten gefunden werden. Ein Vergleich der Feldstärke ϵ_0 mit den Werten basierend auf einer Parametrisierung von früheren LOPES Daten, zeigt wesentliche Unterschiede, wobei die Feldstärken der Lateralverteilung systematisch über denen der parametrisierten Werte liegen. Mit Hilfe von Monte Carlo Simulationen der Radiostrahlung von Luftschauern, angepasst auf die gemessenen Ereignisse durch Verwendung der individuellen Schauerparameter, kann ein direkter Vergleich mit den Messungen durchgeführt werden. Das Ergebnis dieses Vergleichs ist, daß die gemessenen Lateralverteilungen systematisch flacher sind. Im Besonderen gilt dies für die Sonderfälle mit einem sehr großen Skalenparameter ($R > 200$ m), die nicht durch die Simulation reproduziert werden können. Im Vergleich der Feldstärken von Messung und Simulation bei verschiedenen Abständen zeigten sich Diskrepanzen in der Vorhersage der Absolutwerte der Feldstärken für den Bereich nahe am Schauerzentrum. Dies ergibt sich als Folge der höheren Werte für den Skalenparameter. Als Ergebnis des Vergleichs ist besonders hervorzuheben, daß die Absolutwerte im Abstandsbereich von $R = 75$ m nur noch in der Größenordnung von $\approx 10\%$ differieren.

Abstract

This work investigates the properties of the radio emission of cosmic ray air showers, in particular by reconstructing the lateral distribution of the emission on an event-by-event basis. The LOPES experiment is measuring the radio emission in the frequency range 40–80 MHz in coincidence with the air shower experiment KASCADE-Grande. For the present analysis a set of data is used which was measured with east-west oriented antennas. By selecting the high energy air showers the occurring short radio pulses can be observed and the lateral distribution of the radio signal for individual showers reconstructed. Based on a performed amplitude calibration of the radio signals for each antenna the absolute value of the field strength is known. Therefore the scale parameter R_0 and the field strength ϵ_0 of the lateral behavior can be determined. The obtained most probable value of the scale parameter results in $R_0 \approx 125$ m, and no significant dependence of this values on general shower parameters, like angle-of-incidence or primary energy could be found. A comparison of the field strength ϵ_0 with the value obtained by a parameterization of earlier LOPES measurements yields significant differences, whereby the field strengths determined from lateral distributions are systematically above the values of the parameterization. Using Monte Carlo simulations of the radio emission of extensive air showers, adjusted to the individual measured events by using the known individual shower parameters, direct comparisons with the measurements are performed. As a result of this, a systematically flatter lateral distribution was obtained for the measurements. In particular, measured events with large scale parameter ($R_0 > 200$ m) could not be reproduced by the simulations. The comparisons of the field strength at different distances with the simulations show a significant discrepancy close to the shower core. This arises from the larger scale parameters at the measurements. However, an important conclusion from the comparison of measurements with simulations results in a deviation of only $\approx 10\%$ of the absolute values of the field strength at a distance of 75 m.

Content

1. Introduction

The cosmic ray particles are a phenomenon that caught the attention of many scientists and in order to understand their origin many measurements were performed. The cosmic ray particles hit the Earth's atmosphere and after the first interaction with nuclei of air molecules many secondaries are propagating through the atmosphere with a velocity close to the speed of light as disc of particles. Such a disc is called an extensive air shower (EAS).

The processes related to the EAS generation and development are manifold and in particular emission processes in the radio frequency range are of interest for the studies in the frame of this thesis. The radio emission in EAS can be measured with an array of antennas, in this case by the LOPES experiment. The results of the measurements are of interest for the establishing of a new complementary detection technique of high energy cosmic rays in astro-particle physics.

First experiments performed in the 1960s and 1970s face a lot of difficulties, e.g. the understanding of theory of the geomagnetic effect for the radio emission or by missing accuracy in detecting very short radio bursts. This was leading to large differences of an order of magnitude in the absolute field strength between measurements performed by different groups. The LOPES experiment is setup at the location of the well calibrated EAS experiment KASCADE-Grande and this gives the possibility to perform coincident investigations of properties of the shower parameters and the radio emission.

The calibrated measurements of the electric field strength in EAS with the LOPES antennas make it possible to investigate lateral distributions of the radio emission on an event-by-event basis. In particular, the obtained results can be compared with dedicated Monte Carlo simulations of the radio emission.

Chapter 2 gives an overview of the current knowledge on origin, acceleration, and propagation of cosmic ray particles. Furthermore, the radio emission processes and their simulation on Monte Carlo based techniques are described. Chapter 3 outlines the experimental setup of the LOPES experiment. The required and applied calibration procedures for the LOPES setup are discussed in chapter 4. Finally, the analysis of the lateral distribution of EAS radio emission will be presented in chapter 5.

2. Cosmic Ray Air Showers and Radio Emission

2.1 Cosmic Ray Particles in the Universe

Cosmic ray particles are an inevitable part of the universe and their existence spans a bow of questions from the particles' nature, their sources in the universe, propagation therein, and observation on Earth. The answers for some of these questions require a closer look and have to be considered in our present overall picture of the universe. The observation of cosmic ray particles is a small, nevertheless interesting contribution.

The universe is such a mysterious place that since centuries we always discover something new. And if we think that we understand our world, there are discoveries that just do not fit with our expectation or model of the overall picture. But having an expectation or model means that we already know something about it and try to make predictions out of the model. Presently we have developed a model of our universe, the Λ Cold Dark Matter model - ΛCDM, that tells us what the nature of the universe is thought to be. Beside the normal baryonic matter in the universe, expressed as a matter density Ω_{b}, there is a contribution of non-baryonic cold dark matter, Ω_{dm}. Together they are described as the total matter density Ω_{M}. Finally a so-called cosmological constant $\Lambda \neq 0$ is introduced, which can be considered as an energy term, or as well as an energy density Ω_{Λ}. From the theory of inflation which is part of the ΛCDM-model one gets that the geometry is a flat one, ($\Omega_{\mathrm{k}} = 0$), where the density parameter Ω_{total} is equal to unity. Summing over the different contributions from the specified densities the total density can be written as:

$$1 = \Omega_{\mathrm{total}} = \Omega_{\mathrm{M}} + \Omega_{\Lambda} + \Omega_{\mathrm{k}} \tag{2.1}$$

where these parameters can be measured by experiments. With $\Omega_{\mathrm{dm}} \approx 0.23$ and $\Omega_{\Lambda} \approx 0.73$ the universe is being filled up to 96 % with something that is unknown in origin and not measured yet. From the Wilkinson Microwave Anisotropy Probe (WMAP) satellite mission the parameter for the ΛCDM model can be constrained (Spergel et al. 2007) and this gives presently a value for the baryonic matter density

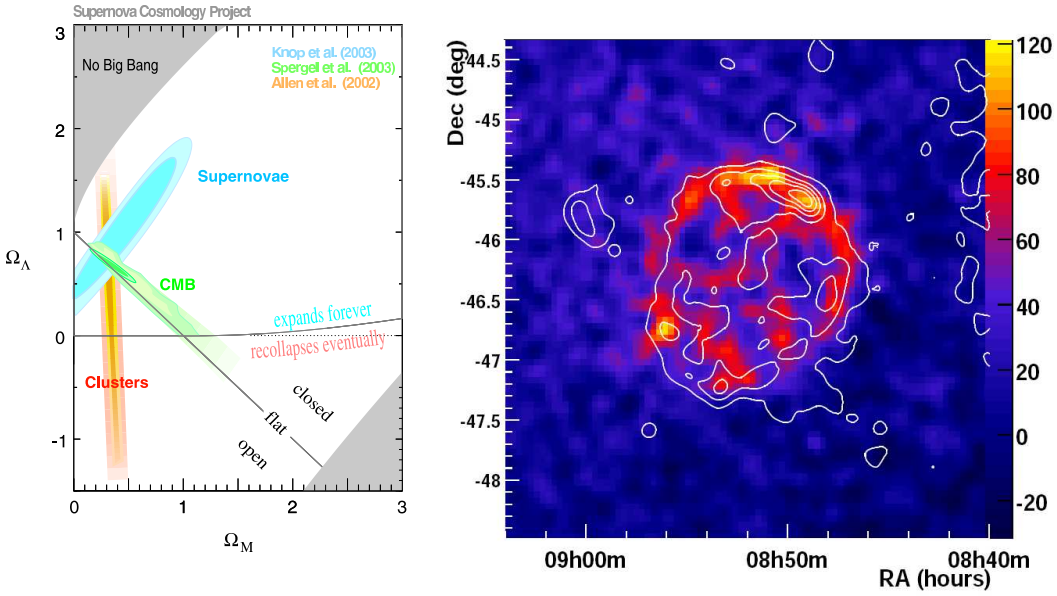

(a) Relation of Ω_Λ and Ω_M from various measurements, figure taken from Knop et al. (2003). With complementary measurements of the CMB and supernova the remaining parameter space is well constrained.

(b) RX J0852.0-4622 is a shell-type supernova remnant. The color image is from HESS observations, the white lines are the contours of the X-ray data from the ROSAT All Sky Survey.

Figure 2.1: Observations of supernovas in the universe are used to constrain the parameter space of the ΛCDM-model (a) and the supernova remnants - SNR (b) play an important roll in cosmology as well as in astroparticle physics.

of $\Omega_b = 0.0444^{+0.0042}_{-0.035}$. Together with other measurements from high redshift supernovae (Knop et al. 2003), X-ray gas mass fraction of cluster of galaxies (Allen et al. 2002), or from weak gravitational lensing observations (Benjamin et al. 2007), the possible parameter range can be constrained even further as they are complementary. This is illustrated in figure 2.2(a) showing the density Ω_Λ over the matter density Ω_M as the sum of baryonic matter and cold dark matter. There are remaining 4% for our well known baryonic matter that can be found all over our universe, in many different energetic states and compositions. In our universe the large scale structures, galaxy clusters and galaxies, the stars and celestial bodies, the planets, the solid state body, and the constituent of atoms, can be observed in many different ways using different techniques. All these structures can show sometimes totally different appearances, however there is always normal baryonic matter involved in it, like photons or charged particles.

On Earth one can observe a large variety of baryonic matter coming from space, a part of it are charged particles with high energy. These particles can be ionized nuclei or leptons, where the ionized nuclei are the dominant part compared to electrons/positrons, neutrons and photons. The fraction is about 10^{-6} and all together are the so-called cosmic rays (CR). These particles are originating from space and must have been created and accelerated somewhere. Afterwards they travel from their point of origin through the universe. Finally they might enter the Earth's atmosphere and collide with a nucleus of air molecules whereby they produce a cascade of lower energy particles. This cascade of particles in the atmosphere can be

observed with different techniques, like particle detectors, optical telescopes, or radio antennas.

2.1.1 The Origin of Cosmic Rays

There are various sources of CR particles under consideration and all of them are astronomical. The closest source is the Sun, and it contributes most to the flux that can be measured on Earth. The word "cosmic" implies that the origin is extra-solar, but there is a continuous transition from particles coming from the sun and particles arriving almost isotropically from the galaxy. Almost all solar cosmic rays, however, have low energy (in the MeV-range) and consist of protons, neutrons, or electrons ejected from the Sun's corona and from solar flares. The transition starts at around 10 GeV and this is the begin of the cosmic ray spectrum.

While the Sun is the closest star, there are many more stars in our galaxy ($\approx 5 \cdot 10^{11} - 10^{12} \mathrm{M}_\odot$, Klypin et al. (2002), expressed in solar mass $\mathrm{M}_\odot$) and many of them can emit ionized nuclei with high energies.

As stars develop, they change their nuclear composition. This can finally lead to the formation of neutron stars, which is one possible endpoint of the star evolution. Of course, a star's evolution depends on parameters like the initial mass, the angular momentum, and the stellar environment. A neutron star is formed from the collapsed remnant of a massive star after a Type-II, Ib, or Ic supernova. Neutron stars have been suggested as possible sources of UHECRs in an early study by Gunn & Ostriker (1969).

Not only stars, but also supernovae remnants (SNR) or black holes (BH) with their accretion discs can be considered as sources for the cosmic rays or the UHECR. A SNR is a shell of matter expanding into the surrounding intergalactic medium (see figure 2.2(b)). As the mean velocity of this expanding shell is significantly higher than the one of interstellar medium, this causes a shock front. The acceleration of particles crossing the shock front can produce CRs, which will be described more thoroughly (see below).

From supernova explosions of massive stars a stellar black hole can be formed. These black holes will have only a few solar masses, $M_\odot$. In the center of our galaxy exists a super-massive black hole with a mass of $M_{\mathrm{BH}} = 3.5 \cdot 10^6 \mathrm{M}_\odot$ (Schödel et al. 2002). Such a super-massive black hole creates a huge gravitational potential that attracts surrounding matter and also remote stars. During the infall towards the event horizon of the black hole angular momentum has to be transported outwards. This leads to the formation of an accretion disc of in-falling matter, which appears to be the limiting factor for the growth of a black hole. The galactic super-massive black hole seems to have presently a low accretion rate and can be called 'inactive'.

For many types of galaxies a super-massive black hole is assumed to be present in the center, and this even holds for late-type galaxies (Satyapal et al. 2008). Some of them have an accretion rate so high that they appear to be very active in a wide wavelength range, they are then called active galactic nuclei (AGN). Considering AGNs as sources of UHECRs, one can search for anisotropies in the CRs' arrival directions and try to correlate this with known AGN locations (The Pierre AUGER Collaboration et al. 2008), as was done with data from the AUGER experiment (Abraham et al. 2004).

2.1.2 Acceleration Mechanism

The energies detected for cosmic rays require an acceleration mechanism that is efficient enough for fully ionized particles with masses from hydrogen up to iron. To accelerate them to very high energies, this can be considered as a bottom-up scenario, whereas a top-down scenario does not directly require an acceleration mechanism to create the observed energy distribution of CRs.

From SNR observations, either optical or γ-ray, the expanding shells into the interstellar medium can be investigated and they are generating strong shock fronts. The currently accepted model of galactic cosmic-ray acceleration in such shock fronts is the first-order Fermi mechanism (Axford et al. 1977; Krymskii 1977; Bell 1978; Blandford & Ostriker 1978). Particles can cross from ahead of the expanding shock front (upstream) through the front into the region behind (downstream). When the particle returns from downstream to upstream it has completed a cycle. For this cycle there is a gain of energy ΔE that is proportional to the particle energy E. There are magnetic fields in involved the vicinity of the shock front, which can confine particles that they can pass more than one cycle. With increasing, energy particles remain longer, nevertheless there is a certain probability that particles do not re-enter from downstream to complete their cycle. The high energy particles have more time to gain energy, but there is is an upper limit in energy that can be achieved in this way, depending on the features of the shock.

For the first-order Fermi acceleration this can be expressed with the relation $E_{\max} \sim Ze\beta_s BtV_s$, where $\beta_s = V_s/c$ is the velocity of the shock front and t the time. As the mechanism involves a magnetic field B one can expect to have a charge number Z dependence for the maximal energy. This can be expressed as $E_{\max} \approx Z \cdot 5$ PeV for some types of SNRs (Kobayakawa et al. 2002; Sveshnikova 2003). Even if there are only a few SNRs in the galaxy, they might be enough to explain the flux and spectrum we observe at these energies of the galactic CRs (Berezhko 2008). For close-by SNRs there should be an observable flux of high energetic particles from this source. From TeV-range γ-ray astronomy observations of the SNR RX J1713.7-3946 (Aharonian et al. 2004) with the HESS telescope (Bernlöhr et al. 2003) the indication of efficient acceleration of charged particles to energies beyond 100 TeV is reported. There will be most probably in the near future more direct evidence that the SNRs are sources of CRs because the γ-ray astronomy is presently a growing field with new, larger, and more sensitive telescopes.

Rotating neutron stars are also considered as candidates for CRs (Gunn & Ostriker 1969) and discussed more recently by Bell (1992) studying cosmic ray acceleration in pulsar-driven supernova remnants. The pulsar is a fast rotating neutron star. During its formation, the magnetic field of the progenitor may not be aligned with the rotation axis. In this case the magnetic field lines are moving fast through the residual ionized gas of the supernova and cause the emission of radiation in the radio, optical and X-ray frequency range. The rotation period of pulsars varies from ‘millisecond pulsars‘ up to a few seconds. In an analysis of Hillas (1984) the maximum energy that can be obtained from a pulsar is calculated to:

$$E_{\max} = \frac{\omega}{c} Z\, e\, B_s R_s^2 \tag{2.2}$$

where ω is the pulsar angular velocity, B_s the surface magnetic field and R_s the neutron star radius. Using a transposition and transformation of the equation 2.2 to

the rotation period T, one can estimate what rotation period is needed to accelerate particles to an maximal energy $E_{\max}$.

$$T = cZeBR^2 2\pi / E_{\max} \tag{2.3}$$

With the assumption of typical neutron star values, a 'millisecond pulsars' can produce ultra high energy cosmic rays with energies above 10^{10} GeV. Astronomical observations of pulsars show what the present galactic pulsar population is. Using a certain acceleration scenario for the CRs from pulsars one can obtain a particle flux in the order of the measured flux of CRs at Earth (Giller & Lipski 2002).

The acceleration up to the highest energies one can observe at Earth requires even more efficient mechanisms. As the galactic CRs can not explain the spectrum alone, there has to be a transition to extra-galactic CRs. Presently we have no definite explanation for the observations and the underlying acceleration processes. That here AGN can play an important role may be imagined, because there is a sub-class of AGNs that eject jets of particles from their central black hole. These relativistic jets can be observed in the radio frequency range as large radio lobes with extensions up to hundreds of kilo-parsecs. The central super-massive black hole attracts surrounding matter and forms an accretion disc that probably generically leads to relativistic jets. In particular Kerr BHs are coupled with magnetic fields and these fields are supported by the currents in the external gas of the BH. About ten percent of these AGNs have relativistic jets with strong, complex magnetic fields. The endpoints of the jets in the intergalactic medium generate shock fronts that can accelerate particles.

Acceleration has been considered so far as a bottom-up scenario, whereas a top-down scenario does not directly need an acceleration mechanism. In this case the CRs particles are originating as decay products from higher energetic X-particles, whatever these particles might be. These models require an increasing photon component at energies above about $10^{19.7}$eV, due to gammas as preferred decay product.Taking into account the present Pierre Auger Observatory limits on the photon fraction these models are essentially excluded (Semikoz et al. 2007).

However, there exist ultra high energy cosmic rays (UHECR) filling our universe and we just do not know yet where they originate from. However, they exist and propagate through the universe and only a negligible fraction approaches our Earth.

2.1.3 Propagation

That we can observe at all galactic cosmic rays at Earth implies that they are not immediately escaping from our galaxy. Our galaxy contains a galactic magnetic field with different components, a large-scale regular and a chaotic irregular component, known from observations in our and other galaxies (Beck et al. 1996). As the accelerated particles are injected into the galaxy they undergo an interaction with this magnetic field. The gyro-radii of high energetic particles above 10^{18} eV are larger than the extension of our galaxy, which is about 30 kpc in diameter. The propagation is a diffusive one and the mean free path length is much larger than the size of our galaxy, which leads to residence times of about 10^7 years. With models, like leaky box models, the propagation of the cosmic rays in our galaxy is described and they try to reproduce the observed cosmic ray flux at Earth.

Several aspects have to be considered when the CRs particles propagate, which finally determine the measured composition and fluxes. There are the interactions with magnetic and also electric fields that can lead to re-acceleration. Furthermore the particles lose energy due to ionization and inelastic scattering. The composition will change after spallation or radioactive decay of the CRs. From observation of the boron to carbon ratio it is derived that higher energetic particles traverse less matter and escape earlier from the galaxy. Therefore, the measurement of the composition of CRs can help to understand the processes during propagation.

The acceleration of the CR results in an energy spectrum that can be described by a power law $E^{-\gamma}$ with spectral index $\gamma \approx 2$. This energy spectrum changes the slope due to the different processes of the propagation and results in a spectral index of $\gamma \approx 2.7$, as one can observe for energies below some PeV.

2.1.4 Energy Spectrum

From the list of possible sources we can see that the energy spectrum spans a wide range from a few tens GeV up to around 10^{11} GeV. The lowest energetic CRs originate from outside the heliosphere and have the highest flux contribution off all measured CRs. This low energy part of the spectrum can be measured directly with high-altitude balloons or satellites. As we have seen, the acceleration for the CRs leads to an energy spectrum with a power law characteristics. Therefore the flux as the number of CRs passing through a surface can be written like:

$$\frac{dN}{dE} \propto E^{-\gamma}, \tag{2.4}$$

with $[\frac{dN}{dE}] = \mathrm{m}^{-2}\mathrm{s}^{-1}\mathrm{sr}^{-1}$. The spectral index γ is a parameter describing the shape that can change over roughly ten orders of magnitude in energy E. Figure 2.2 shows the cosmic ray energy spectrum in the energy range from 10^{13} eV to $> 10^{20}$ eV, where the flux is multiplied with $E^{2.5}$ in order to point out the features of the spectrum. Underlying one can find possible detection ranges in energy for proposed experiments based on radio detection technique, like LOPES and LOFAR.

At low energies the flux is high enough to equip only a small detector area and gain sufficient statistics for different mass numbers of CR particles. The penetration depth for CRs in the atmosphere is increasing with their energy. In the GeV to TeV range balloon measurements are performed to measure directly the CRs and resolve the composition from a spectrometer. With long duration circumpolar flights (Jones 2005) composition studies can be extended up to 10^5 GeV. Beyond this energy only indirect measurements of the primaries can be performed, due too low fluxes. From 10^2 GeV to 10^5 GeV the energy changes by three orders of magnitudes, respectively the flux is decreasing by $10^{-2.7\cdot 2}/10^{-2.7\cdot 5} = 10^{8.1}$, i.e. eight orders of magnitude. That means, to gain the same statistics one has to go from a 1 cm detector area to a 100×100 m^2 area.

In the energy range of $\approx$ 10 GeV up to about $3 \cdot 10^6$ GeV the spectrum exhibits a spectral index of $\gamma \approx 2.7$. This is the well measured part of the spectrum and it is obtained from the acceleration and propagation of the CRs in our galaxy, sometimes referred as galactic component (see sections 2.1.2 and 2.1.3).

At an energy of $3 \cdot 10^6$ GeV the index changes and the slope becomes steeper, now exhibiting $\gamma \approx 3.1$. This feature is called *knee* of the cosmic ray spectrum. The first

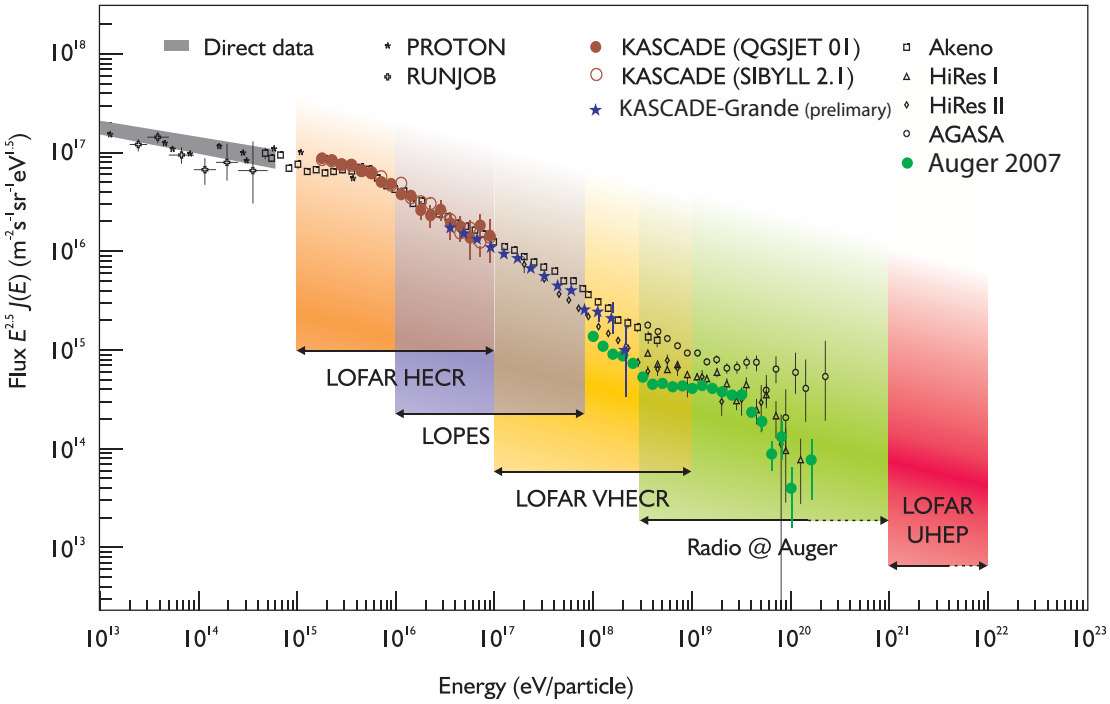

Figure 2.2: The flux spectrum of cosmic rays over energy is multiplied with $E^{2.5}$. Possible detection ranges in energy for proposed experiments based on radio detection technique are highlighted in different colors. The LOPES experiment sets for the energy range 10^{16-18} eV.

observation of this feature was done by Kulikov & Khristiansen (1958) who found an evidence for a change in the slope of the spectrum, measuring the electro-magnetic component of air showers (about components in EAS see section 2.2). An index change at this energy can be due to the acceleration mechanism that was discussed in section 2.1.2. At some point the highest energy $E_{\max}$ is reached in the shock fronts from SNRs. Furthermore the escape probability from our galaxy is increasing with energy. Some propagation models explain the spectral change as a consequence of the diffusion effects during the cosmic ray propagation in our galaxy (Ptuskin et al. 1993). A cutoff starts and perhaps this is a charge number Z depended effect, taking into account that magnetic fields have an effect on charges. If a proton gains a maximal energy $E^p_{\max}$ then this would be for the heavier nuclei at:

$$E^Z_{\max} = E^p_{\max} \cdot Z \tag{2.5}$$

The maximum energy gain of a proton, $E^p_{\max}$, translates for heavier nuclei Z to $E^Z_{\max}$. From this relation one can derive that at a certain energy $E > E^p_{\max}$ the flux of galactic protons decreased, and that the galactic CRs flux ends at some certain energy at all. The spectrum and composition at the knee was measured extensively. The KASCADE experiment (Antoni et al. 2003) showed that the knee is attributed to a significant flux reduction for protons (Antoni et al. 2005).

The spectral index seems to change again at an energy $E = 3 \cdot 10^8$ GeV and various experiments indicate the existence of a so-called *second knee* in the cosmic ray spectrum. This feature could be the signature of the end of the galactic component and the emergence of the extra-galactic one, providing that the latter cuts off at low

energies. In the oversimplified picture of a pure charge number dependent acceleration mechanism this would give a charge number of $Z \approx 100$. This is beyond the charge number of iron ($Z = 26$), which is the upper limit in the CR composition. An alternative is the existence of a second galactic component, maybe from CRs acceleration at pulsars, with rigidity dependent cut-off at higher energies.

After the second knee there is another change of the spectral index in the cosmic ray spectrum, to a flatter spectrum than before. At energies above $4 \cdot 10^9$ GeV there is a rise of the spectral index to $\gamma \approx 2.7$. The experimental evidence is less strong than at lower energies due to the already very low flux and the large detection area needed. This feature is often called the *ankle* of the CR spectrum. A harder extra galactic component dominates now the flux of particles and most probably the galactic component dies out, due to missing acceleration mechanisms. The last feature is a cut-off of the spectrum. This was predicted by Greisen (1966), V. Zatsepin & Kuz'min (1966) independently and it can be considered as an upper limit for CRs. Energies above $5 \cdot 10^{10}$ GeV in the rest frame of the CRs are high enough for an interaction of protons with the cosmic microwave background (CMB).

$$\gamma_{\mathrm{CMB}} + p \rightarrow \Delta^+ \rightarrow p + \pi^0 \tag{2.6}$$

The γ_{CMB} photons with their 2.7° K temperature fill up the universe as a background radiation, first measured by Penzias & Wilson (1965) as an excess in the antenna temperature at 4080 Mc/s. This last feature in the spectrum is presently under strong investigation and the upcoming measurements have to how if there is a cutoff or not.

2.2 Extensive Air Showers - EAS

The sources of CRs - the stars, pulsars, SNRs, or AGNs - are present all over the universe, that is filled with billions of galaxies. The escape probability from these galaxies is non-zero and CRs should be found all over in the universe. Finally some CR particles hit the Earth's atmosphere and we can measure them. Our solar system is moving within the galactic plane, which is also the place where CRs originate and start propagating. More precisely the ecliptic is tilted about 67° against the galactic plane and the sun is located ≈ 5.2 pc above the galactic plane. There will be for sure collisions between the heliosphere and the cosmic ray particles propagating in the galaxy. Even if the solar heliosphere can be considered as a shielding against low energetic particles the cosmic rays can reach the Earth's outer layers. The flux of the particles might be different outside the heliosphere, but this affects only the low energy cosmic ray particles. The penetration of a denser media object, denser than the ambient inter-solar space, will lead to an increasing interaction probability and this will happen, e.g. in the upper atmosphere of the Earth. There, the primary cosmic ray particle interacts with a nucleus of the air molecules. In this first hadronic interaction secondaries with lower energies are produced and in most of the cases the involved nitrogen or oxygen nuclei suffer a spallation.

The secondaries propagate relativistically through the atmosphere and undergo even more interactions or decay to lighter particles. The disc of particles is growing while traveling further in the direction of the incoming cosmic ray particle. This propagating disc of particles is called an extensive air shower - EAS (Auger et al.

1939). The extraterrestrial origin of CRs was discovery first by F. Hess (1912) when he examined the ionizing radiation in the atmosphere, almost century ago. From the fact that the EAS changes with height a development of the shower is expected and as there are hadronic particles involved, the secondaries will arise from different types of interactions and decays.

2.2.1 Components of EAS

The first interaction is a high energy hadronic one and results in mostly unstable particles wherefore an EAS will have different components of particles.

The total number of particles in a shower relates logarithmically to the primary energy, until a certain, particle specific, threshold energy is reached and then no new particles will be created anymore. At a certain height of the EAS development a maximum for the number of particles in the shower disc in reached, $N_{\max}$, and afterwards the number decreases exponentially. In terms of atmospheric depth X (in g cm^{-2}) the EAS at the shower maximum has a depth $X_{\max}$. The longitudinal shower development can be described with the Gaisser-Hillas function (Gaisser & Hillas 1977):

$$N(X) = N_{\max} \cdot \left(\frac{X - X_0}{X_{\max} - X_0} \right)^{\frac{X_{\max} - X_0}{\lambda}} \exp \frac{X_{\max} - X}{\lambda} \tag{2.7}$$

The number of charged particles N at a given atmospheric depth X in this relation depends also on the parameters X_0 and λ that determine the shape of the shower. In figure 2.3 (left) the shower development for simulated proton- and iron-induced showers is shown. The number of particles increases with atmospheric depth up to the value $X_{\max}$ and decreases exponentially afterwards. The simulation distinguishes between electrons/positrons and muons. Most of the charged particles are electrons and positrons, making up 90% of the total number. Together with the photons this is called the electromagnetic component of an EAS. There are also muons in the shower, e.g. from decays of charged pions, that are called the muonic component. With approximately 10% the muonic component is clearly less abundant than the electromagnetic component, but significantly more numerous than the hadronic component.

Hadronic Component
The pions or other mesons, and three quark composed particles, baryons represent the hadronic component of the EAS comprises about 1% of all particles detected at ground level. The first collision typically produces more than fifty secondaries and they carry most of the energy in the early shower stage. Due to their high longitudinal momentum they are emitted closely to the original particle direction and the lateral spread is only a few tens of meters at observation level. Fluctuations in the hadronic component can significantly influence the development of the other two components as they evolve from it.

Muonic Component
This component takes all the muons into account that are produced during the shower development. The hadronic interaction leaves charged mesons, e.g. pions or kaons, which have a short life time. If they do not interact during their propagation

(more likely in the thinner upper atmosphere), they will decay in lighter mesons or directly into muons.

$$\begin{aligned}
\pi^{\pm} &\rightarrow \mu^{\pm} + \nu_{\mu}(\text{BR } 99.99\%) \\
K^{\pm} &\rightarrow \mu^{\pm} + \nu_{\mu} \ (\text{BR } 64\%) \\
&\rightarrow \pi^{0} + \pi^{\pm} \ (\text{BR } 21\%) \\
&\rightarrow 3\pi^{\pm} \ (\text{BR } 5\%) \\
&\rightarrow \pi^{0} + \mu^{\pm} + \nu_{\mu} \, (\text{BR } 3\%) \\
\mu^{\pm} &\rightarrow e^{\pm} + \nu_{e} + \nu_{\mu}(\text{BR } \approx 100\%)
\end{aligned}$$

The life time of relativistic muons[1] is much longer and therefore they can travel much further than the hadronic component. Muons can lose their energy by ionization and by radiative processes, bremsstrahlung, direct production of e^+-e^- pairs, and photonuclear interactions. The total muon energy loss may be expressed as a function of the amount of matter traversed as $-dE/dX = a + bE$ where a is the ionization loss and b is the fractional energy loss by the three kinds of radiation processes. The atmosphere is a thin medium compared to a solid state body and the energy loss due to Bremsstrahlung will be much lower for muons than for electrons, as it is suppressed by $(m_\mu/m_e)^2 \approx 42000$. Low energy muons from late shower stages can decay and add electrons/positrons to the electromagnetic component. The high energy muons from early stages reach the ground and have lost about 2 GeV by ionization, assuming a muon production height (Bürger et al. 1975) of about 15 km.

Electromagnetic Component

The lightest particles in the shower are electrons, positrons, and photons, but their contribution to the total number of charged particles is the highest one, with about 90%. In hadronic interactions, neutral and charged mesons are produced, 99% of which decay in the following two ways:

$$\begin{aligned}
\pi^{0} &\rightarrow \gamma\,\gamma(\text{BR } 98.8\%) \\
\pi^{\pm} &\rightarrow \mu^{\pm} + \nu_{\mu}
\end{aligned}$$

The charged pions live $\approx 10^8$ times longer than the neutral pions which might lead to a smaller contribution to the electromagnetic component. The two resulting energetic photons from the π^0 decay create via pair production electrons (equation 2.8). These electrons can again produce photons (equation 2.9) by bremsstrahlung.

$$\gamma \rightarrow e^{+}e^{-} \tag{2.8}$$

$$e^{\pm} \rightarrow e^{\pm} + \gamma \tag{2.9}$$

A cascade of electromagnetic particles is initiated from this until the energy is fallen below a critical energy E_C (for air is $E_C \approx 80$ MeV). Then the energy loss via ionization becomes dominantly and no new particles are produced for the cascade. At this stage, the cascade will start to die out and the exponential decrease for the number of particles takes effect, see equation 2.7, with $N \sim \exp\left(\frac{X_{\max}-X}{\lambda}\right)$.

Besides the creation and loss of particles in the longitudinal direction, the electromagnetic component suffers Coulomb scattering. The particles are laterally spread

[1]The rest frame life time for the muon is $\tau = 2.19703(4) \cdot 10^{-6}$s

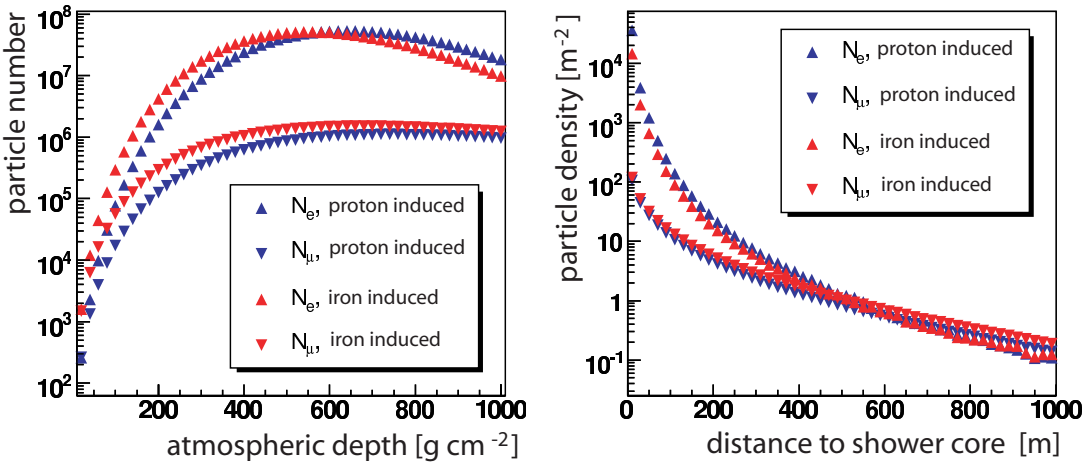

Figure 2.3: From simulation of a 10^{16}eV shower, either proton- or iron-induced, the electromagnetic and muonic components are shown. The change of the particle number with atmospheric depth (left figure) indicates a maximum of particles $N_{\max}$ and the particle density as a function of the lateral distance from the shower center (right figure) can be described with a NKG-function.

out which is described by the Molière theory (Molière 1947, 1948) and has a characteristic quantity, the Molière radius R_m. To describe the lateral distribution of electrons in the shower a NKG-function is used (Greisen 1956; Kamata & Nishimura 1958):

$$\rho(r) = \frac{N_e}{2\pi \cdot R_m^2} \cdot \left(\frac{r}{R_m}\right)^{s-2} \left(1 + \frac{r}{R_m}\right)^{s-4.5} \cdot \frac{\Gamma(4.5-s)}{\Gamma(s)\Gamma(4.5-2s)} \tag{2.10}$$

The density $\rho(r)$ is calculated from the number of electrons N_e at observation level and the distance to the shower core r. The parameter s is a lateral shape parameter. In figure 2.3 (right) the lateral distributions for simulated proton- and iron-induced showers are shown. The NKG-function can be applied to, e.g. lateral particle distributions measured at ground. The shape parameter s is a fit parameter from the observations and the term $\frac{\Gamma(\beta-s)}{\Gamma(s)\Gamma(\beta-\alpha s)}$ is used as a normalization factor, with $\alpha = 2$ and $\beta = 4.5$. At the observation level of KASCADE-Grande a Molière radius of $R_m = 89$ m is used and for the range $0.8 < s < 1.6$ the NKG-function is valid. For Grande the parameters $\alpha = 1.5$, $\beta = 3.6$, and $r_0 = 40$ m were found as optimum for the radial distances (Glasstetter et al. 2005).

From the total particle number determined with the NKG-function an estimation of the primary energy can be done, whereas from the ratio muon number to electron number, N_μ/N_e, the primary mass is estimated (Haungs et al. 2003).

2.3 Radio Emission in EAS

Since there is such an abundant electromagnetic component in EAS further secondary effects can be expected, besides energy loss through secondary particles. The electromagnetic component loses part of its energy in the atmosphere via ionization and this results in excitation of nitrogen molecules in the air. The de-excitation of the molecules is partly emitted as fluorescence light that can be observed with telescopes at ground level (Keilhauer et al. 2006). Another effect arises when a charged

relativistic particle passes through an insulator at a speed greater than the speed of light in that medium, electromagnetic radiation is emitted, called Čerenkov radiation. The refractive index of air, $n_{\text{air}} = 1.000292$ at $\nu = 589$ nm, is only slightly different from vacuum $n_{\text{vac}} = 1$ leading to a small contribution of Čerenkov radiation, compared to the emission in the radio frequency range. On the other hand the Čerenkov radiation is a large background for fluorescence measurements.

Nevertheless, both emissions are used for the detection of CR, Čerenkov radiation by TeV γ-ray telescopes and fluorescence light by optical mirrors in UHECR experiments. The detection is only possible in moonless, cloudless nights which significantly limits the duty cycle.

Askar'yan (1962, 1965) proposed an effect leading to radio emission in air, especially in dense media. The electromagnetic cascade generates electron/positron pairs via pair production (see section 2.2.1 - Electromagnetic Component) which can interact with the medium. The positrons can annihilate with the electrons of the air molecules, furthermore electrons from the air molecules can be regenerated to contribute to the electromagnetic component. This leads to a negative charge excess that travels faster than the speed of light in air towards the Earth and has to emit also Čerenkov radiation. For wavelengths in the order of the shower disc thickness and longer the emission will be coherent. There are presently experiments investigating the Askar'yan effect in dense media, like ice, water, and salt. The RICE experiment placed some radio antennas near the south pole to detect up-going radio signals from in-ice showers and could set limits on ultra-high energy neutrino fluxes above 10^{17} eV (Kravchenko et al. 2006). The experiment ANITA, a dedicated balloon experiment (Barwick et al. 2003), was launched for the first time to circle Antarctica and to detect there distant radio pulses from up-going neutrinos in the ice shelf. There is also the possibility of using a natural rock salt mine as a UHE neutrino detector, a Salt Neutrino Detector (SND, (Chiba et al. 2001)) and rock salt deposits are distributed world wide so there are many candidates for suitable sites.

The matter density in the atmosphere is not constant and reduces about a factor of four from ground to a height of 10 km. At $X_{\max}$ the electromagnetic component has the highest number and the charge excess can be the largest. This of course depends on the density of the air which should be high to let annihilate many of the positrons. The Askar'yan effect relies also on the fact that the medium is radio transparent, which is the case for air. For radiation in the radio frequency range in air the origin is most likely connected with the Earth's magnetic field, already suggested in the late 1960's by Hazen et al. (1969) as geomagnetic production. An analytical model taking into account the charge excess as well as geomagnetic emission mechanisms was developed by Kahn & Lerche (1966).

2.3.1 Geosynchrotron Emission

The Earth has a magnetic field that is approximately a magnetic dipole. Through this field the relativistic shower is moving with its electromagnetic component. For moving charged particles (with velocity $|\mathbf{v}|$) in this external magnetic field $\mathbf{B}$ the Lorentz force $\mathbf{F}$ acts like:

$$\mathbf{F} = q(\mathbf{v} \times \mathbf{B}) \tag{2.11}$$

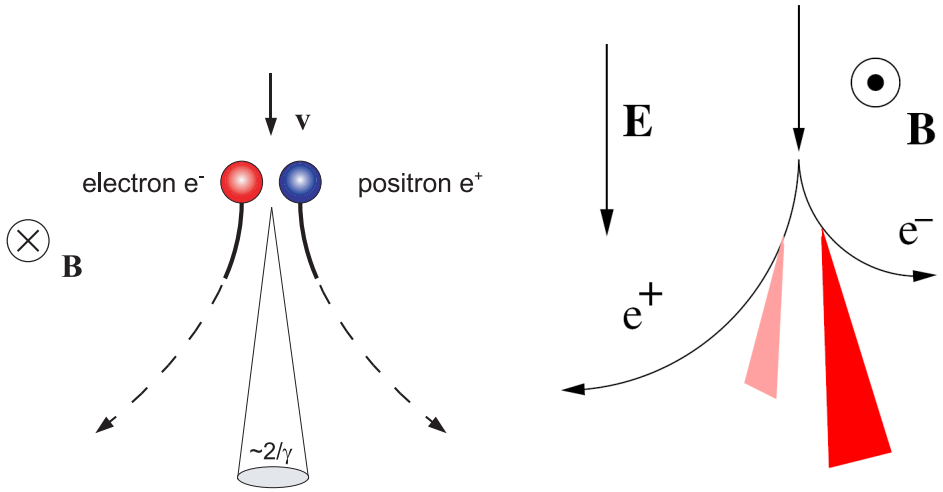

(a) Lorentz force with no external electric field **E**

(b) Additional electric field **E**. Figure taken from Buitink et al. (2007)

Figure 2.4: A moving charge q in a magnetic field **B** will be deflected due to the Lorentz force whereby this accelerated charge will emit electromagnetic radiation in the direction of the motion, see 2.5(a). The electron and the positron are separated on curved trajectories and under the influence of a downward directed electric field **E** an asymmetric radiation is caused, see 2.5(b).

Depending on the sign of the charge q the force acts in opposite directions. This behavior is illustrated in figure 2.5(a) where the magnetic field points into the picture plane.

Any accelerated charge gives rise to electromagnetic radiation (Jackson 1975). Especially any relativistically moving charge is emitting radiation in the forward direction with an emission cone depending on the Lorentz factor with γ^{-1}. This effect is called synchrotron radiation and taking the geomagnetic origin of the field into account this can be called **geosynchrotron radiation**.

Analytical Calculations of the Particle Emission

In an analytical approach (Huege & Falcke 2003), the radiation for a single particle is calculated in the frequency domain to avoid problems from retardation effects. The electric field of a moving charge normalized to the unit solid angle Ω can be expressed with the vector potential $\mathbf{A}(\mathbf{R}, \omega)$:

$$\mathbf{A}(\mathbf{R}, \omega) = \frac{\omega e}{\sqrt{8c\pi}} \exp i \left(\omega \frac{R}{c} - \frac{\pi}{2} \right) \left[-\hat{\mathbf{e}}_{\parallel} A_{\parallel}(\omega) \pm \hat{\mathbf{e}}_{\perp} A_{\perp}(\omega) \right] \tag{2.12}$$

with the plus-sign for the electron and the minus-sign for the positron, the angular frequency $\omega = 2\pi\nu$ of the radiation, and the emission can be conveniently divided into two perpendicular components $\hat{\mathbf{e}}_{\parallel}$ and $\hat{\mathbf{e}}_{\perp}$, that can be used in the far-field limit. For a fixed observer (at distance R) there will be only one flash of radiation from each particle. The single electron or positron does not complete a full gyration cycle (about 20 km) and has lost its energy much earlier. The frequency component of the electric field can be calculated:

$$\mathbf{E}(\mathbf{R}, \omega) = \left(\frac{4\pi}{c} \right)^{1/2} \frac{1}{R} \mathbf{A}(\mathbf{R}, \omega) \tag{2.13}$$

As this is only the emission for a single particle, for the actual situation in a shower pancake one has to superpose the individual emissions with respect to their phase relation. This will give the total radio emission from the EAS.

All Particle Emission
The energy spectrum is $\propto |\mathbf{A}(R), \omega|^2$ which gives a growth $\propto N^2$ with the particle number N, assuming full coherent emission. This full coherence is not in all stages of the shower development fulfilled, as it depends on the frequency ν. To get the total air shower emission one has to integrate over the shower evolution which can be realized by approximating the evolution in slices. For these slices one can take a characteristic scale in the electromagnetic cascade that is the electron radiation length in air $X_0 = 36.7$ g cm^{-2}. Superposition of the individual slice emissions, correctly taking into account the phases arising from arrival times differences, leads to the total emission of the shower.

Monte Carlo Based Parameterized Showers
There are analytical approaches available for the description of the shower evolution that can be used to calculate the emission for different slices. From those one can get the general behavior of the all particle emission (Huege & Falcke 2003). A more sophisticated solution of the calculation of the emission is to use detailed Monte Carlo simulation procedures (Huege & Falcke 2005a,b). The resulting all particle emission can be parameterized in the following way:

$$\begin{aligned} |\mathbf{E}(r, \phi_0, E_p, X_{\max})| &= f E_0 \left(\frac{E_p}{10^{17}\mathrm{eV}} \right)^{0.96} \\ \times \exp &\left(- \frac{200\mathrm{m}(\alpha(\mathrm{X_{max}}) - 1) + \mathrm{l(r, \phi_0)}}{\alpha(X_{\max}) l_\theta} \right) \\ &\times \exp \left(- \frac{\nu/\mathrm{MHz} - 10}{47.96 \exp\left[-l(r, \phi_0)\right]} \right) \end{aligned} \tag{2.14}$$

The relation includes a change of the scale factor l_θ with respect to the shower maximum $X_{\max}$ expressed as the ratio $\alpha(X_{\max}) = l_\theta(X_{\max})/l_\theta(631\mathrm{gcm}^{-2})$. The scale parameter $l(r, \phi) = r\sqrt{1 - \cos^2(\phi_o - \phi)\sin^2\theta}$ is the transformation from the ground-based to the shower-based coordinate system where ϕ and θ specify the shower azimuth and zenith angle and r denotes the observer distance from the shower center and ϕ_o to the observer azimuth. The values for E_θ, l_θ, and b_θ are tabulated quantities and $f = 1$ (Huege & Falcke 2005b). The relation of primary energy E_p of the CR and the electric field strength is approximately linear and can be expressed with a power-law relation, like $|\mathbf{E}(r, 0, 2\pi\nu, E_p)| \propto \left(\frac{E_p}{10^{17}\mathrm{eV}}\right)^\kappa$, using a power-law index $\kappa \approx 0.8 - 1.0$ that depends on the distance of the observer to the shower core.

Monte Carlo Based on CORSIKA Simulated Showers
From the CORSIKA air shower simulation package (Heck et al. 1998) the relevant information of the different shower stages can be obtained more directly. Particle numbers, shower-to-shower fluctuations, energy content, and lateral distributions are available for the Monte Carlo simulations of the radio emission (Huege et al. 2007b). These Monte Carlo simulations enable us to investigate in detail the radio emission from EAS. In figure 2.5 the simulated frequency spectra of the electric field strength $|\mathbf{E}_\omega|$ are shown. Here, a Monte Carlo simulation for a vertical shower with primary

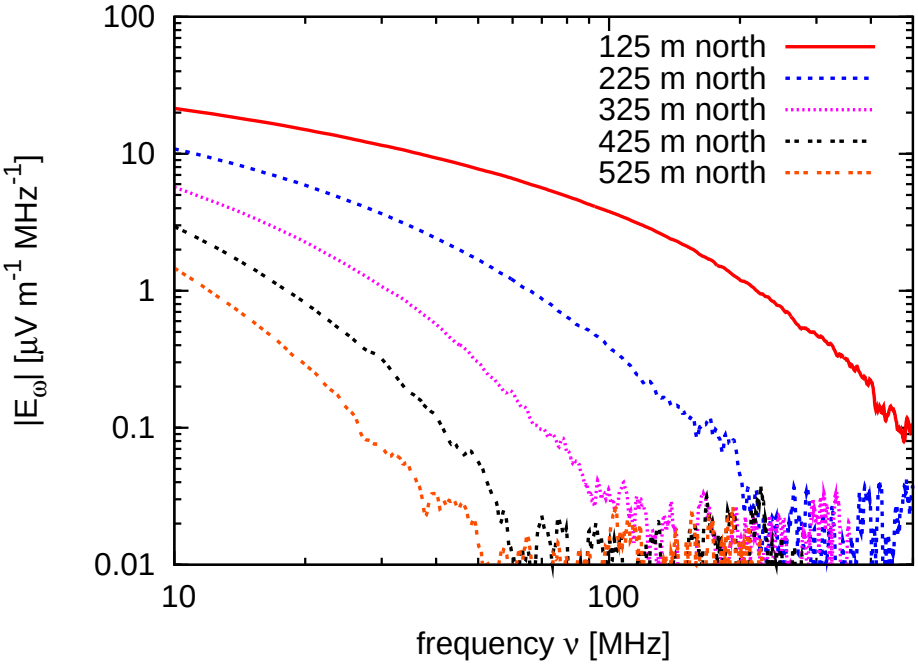

Figure 2.5: Spectrum of the electric field strength $|\mathbf{E}_\omega|$ obtained from Monte Carlo simulations (Huege et al. 2007c) for a vertical shower with primary energy of 10^{17} eV. The spectra are simulated for different observer distances to the shower center. The spectrum falls off very fast (note the double logarithmic scale) and goes into numeric noise at larger frequencies (right bottom).

energy of 10^{17} eV was used. The spectrum was calculated for different observer distances to the shower center (from 125 m up to 525 m north) and exhibits a falling of the spectra towards higher frequencies. The electric field strength $|\mathbf{E}_\omega|$ goes into incoherence, as well into numerical noise, at higher frequencies, in particular sooner for larger distances from the shower center. At

The Monte Carlo simulations calculate the radio pulse in the time domain. A result of these simulations are shown in figure 2.6 where the development of the pulse height for different distance to the shower core is shown. The pulse height is presented for a vertical shower with primary energy of 10^{17} eV. The field strength at different observer distances to the shower center exhibits a decreasing of the amplitude and a broadening. There were different scaling factors used to display the field strength of the pulses.

The use of CORSIKA based Monte Carlo simulations of the radio emission can be regarded as an approach in a microscopic way of modeling the radio emission in EAS. The essential element in the Monte Carlo simulations is the coherent synchrotron radiation from secondary shower electrons and positrons gyrating in the Earth's magnetic field - called geosynchrotron model. The geosynchrotron emission can be also investigated in other Monte Carlo studies, as done by Kalmykov et al. (2006). From a macroscopic point of view the magnetic field of the Earth induces, by pulling with the Lorentz force the electrons and positrons in opposite directions, a net electric current in the electron-positron plasma (Scholten et al. 2008). This method

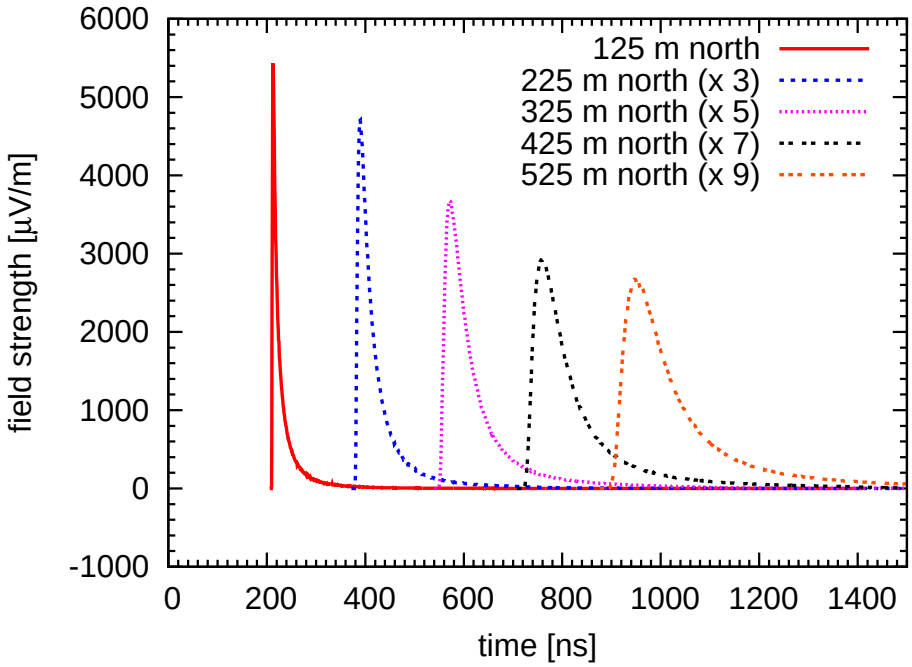

Figure 2.6: The electric field strength and time profile of pulses for different distances from the shower center. Again the observer is north of the center and the Monte Carlo simulation was performed for a vertical 10^{17} eV shower. The pulses are scaled for better presentation.

uses a more realistic air shower model as improvement, but is still very similar to that used in the work of Kahn & Lerche (1966).

Radio Pulses with External Electric Fields

The Lorentz force (equation 2.11) takes into account a magnetic field **B**, but can also be extended with an electric field **E**:

$$\mathbf{F} = q(\mathbf{E} + \mathbf{v} \times \mathbf{B}) \tag{2.15}$$

The atmosphere has an electric field even under fair weather conditions (Le Monnier 1752) with a field strength of about 100-150 Vm^{-1}. The atmospheric electric field **E** can further accelerate the particles in the EAS shower disc and the radio emission can be enhanced (see figure 2.5(b)). Electrons and positrons are separated on curved trajectories due to the Lorentz force and the additional electric field enhances the electron emission and reduces the positron emission for the **E**-field geometry chosen in this diagram. Especially inside thunderclouds large electric fields can be present. Investigations of the radio pulse height under such weather conditions, where field strengths can reach values up to 100 kVm^{-1}, show that the radio emission of EAS is largely amplified (Buitink et al. 2007). There are two mechanisms that can be responsible for amplification: acceleration radiation from the shower electrons and radiation from a current pulse of runaway ionization electrons. The information about the present electric field helps to verify if such signal enhancement is happening and the influence on shower development in general. For the LOPES experiment an electric field mill was installed to monitor the atmospheric electric field, see section 3.3.

2.3.2 Measurements of the EAS Radio Emission

The first discovery of radio pulses from cosmic ray air showers at 44 MHz were done by Jelley et al. (1965). Soon, other measurements could verify this and radio emission from 2 MHz up to 520 MHz was found. In the early 1970s the experiments measured the radio pulses in EAS and could verify the order of magnitude for the absolute field strength. The results of these experiments were summarized in an excellent review of Allan (1971). Nevertheless, there was a lack of understanding of the theory for the geomagnetic effect and a missing accuracy for detecting very short radio bursts, leading to large differences of one order of magnitude in absolute field strength between measurements performed by different groups (Atrashkevich et al. 1978).

In the work of Allan (1971) a parameterization is determined from the radio emission measurements combined with the theoretical expectations at that time. The primary energy E_p, geomagnetic angle α, and the shower axis angle (ϕ, θ) are related to the observable electric field strength ϵ_ν like:

$$\epsilon_\nu = 20 \cdot \left(\frac{E_\mathrm{p}}{10^{17}\mathrm{eV}}\right) \cdot \sin\alpha \cdot \cos\theta \cdot \exp\left(-\frac{R}{R_0(\nu,\theta)}\right) \tag{2.16}$$

R is the distance between the antennas and the shower axis. The scale factor R_0 is about 110 m for 55 MHz and for zenith angles $\theta < 35°$. Towards larger zenith angles the scale factor is increasing, which is also the case towards lower frequencies ν.

To compare this parameterization with results from the all particle emission calculated with Monte Carlo simulations, a conversion of the experimentally motivated ϵ_ν values is needed. The theoretically derived $\mathbf{E}(\mathbf{R}, \omega)$ values (Huege & Falcke 2003) can be converted roughly using the relation:

$$\epsilon_\nu = \sqrt{\frac{128}{\pi}} |\mathbf{E}(\mathbf{R}, \omega)| \approx 6.4 |\mathbf{E}(\mathbf{R}, \omega)| \tag{2.17}$$

From first measurements of the LOPES experiment (Horneffer et al. 2004) the radio pulse height was compared with air shower parameters measured by the KASCADE-Grande experiment (Antoni et al. 2003; Navarra et al. 2004). A parameterization formula, as done by (Allan 1971), that describes the radio pulse height ϵ_est as a function of air shower geometry and primary particle energy E_p was derived (Horneffer et al. 2007):

$$\begin{aligned}\epsilon_\mathrm{est} = (11 \pm 1.0)\,((1.16 \pm 0.025) - \cos\alpha)\cos\theta \exp\left(\frac{-R_\mathrm{SA}}{(236 \pm 81)\mathrm{m}}\right) \\ \times \left(\frac{E_\mathrm{p}}{10^{17}\mathrm{eV}}\right)^{(0.95\pm0.04)} \left[\frac{\mu\mathrm{V}}{\mathrm{m\ MHz}}\right]\end{aligned} \tag{2.18}$$

including the geomagnetic angle α, the zenith angle θ, and the mean distance of the antennas to the shower axis R_SA. The radio pulse height ϵ_est of this parameterization is the measured radio signal using inverted-V shaped antennas of the LOPES experiment (see section 3.1.1). This is only the dominant east-west polarization of the radio emission, different to the predicted east-west emission $\mathbf{E}_\mathrm{EW}(\mathbf{R}, \omega)$ from Monte Carlo simulations. Due to the antenna geometry also contributions from the

vertical component are picked up. Despite this the contributions from north-south and vertical emissions are small. There have been first attempts to compare the values with predictions from theoretical calculations (Huege & Falcke 2003). But so far a reliable comparison of theory and data is missing.

3. LOPES Experiment

The LOPES experiment consists of 41 antennas of different types distributed over the field of the KASCADE-Grande experiment in the Forschungszentrum Karlsruhe, Germany. The first installed antennas were designed as prototypes for the LOFAR experiment (Rottgering et al. 2006), a large antenna array for astronomical purposes. LOFAR is presently being built in the Netherlands. The initial idea for LOPES (LOfar PrototypE Station) was to test the potential of the LOFAR setup for the measurement of cosmic rays and to investigate the properties of the radio component of an extensive air shower. The applicability of the detection method to large scales, like in the Pierre Auger Observatory (Abraham et al. 2004), is being tested especially with self-triggered antennas, LOPES^{STAR}. Another experiment, CODALEMA (Ardouin et al. 2005), at the Nançay radio observatory is also investigating this radio component.

From a scientific point of view the aim of the LOPES experiment is to correlate the observables of the radio measurements with the shower properties provided by the particle air-shower experiment KASCADE-Grande. For this reason, LOPES is triggered by KASCADE-Grande and uses the reconstructed shower data as input for the pulse analysis. In other words, the shower core position at ground and the direction of the shower axis are used as starting values for the reconstruction of the radio signals. The unique combination of an established and well understood air shower array together with a new detection technique gives the best opportunity to study the radio emission in EAS. From the initial setup of ten LOPES antennas first analysis results of the measurements have already been published (Falcke et al. 2005; Apel et al. 2006; Buitink et al. 2007; Petrovic et al. 2007). All the results published so far, however, rely on relative field strength values, which were only roughly normalized by a fudge factor. To quantify the measurements and to compare with theoretical expectations the antennas need an absolute amplitude calibration. This calibration of the system is described in detail in chapter 4.

In order to understand and interpret the recorded data a dedicated knowledge of the LOPES antennas is required. In this section, the hardware components (section 3.1) and the operation (section 3.2) of the system will be described. A special aspect of the operation are the measurements during thunderstorm conditions (section 3.3.2).

During thunderstorms, the operation of LOPES changes into an extended data taking, with the aim to investigate correlations between lightnings and the occurrence of EAS.

3.1 Hardware System

3.1.1 Characteristics of the Dipole Antennas

LOPES now consists of 30 LOFAR-type low band antennas as well as newly designed antennas forming the LOPES$^{\mathrm{STAR}}$ array (Gemmeke et al. 2006). All antennas and the electronics are optimized to measure in the relatively noise-free frequency range of 40 MHz to 80 MHz in Karlsruhe.

The initial LOPES antennas are inverted-V dipole antennas and are installed inside the KASCADE-experiment (Antoni et al. 2003). In figure 3.1 one of the LOPES antennas at the KASCADE-array [2] is shown. The geometry of the frame keeping the inverted-V dipole antenna is a four-sided pyramid made out of PVC tubes. The height of the pyramid is 1.4 m and the base length is 2.0 m. The top of the antenna is a round socket providing space for the dipole antenna and the active balun. The balun performs the balanced to unbalanced conversion, transformation of the antenna impedance to the 50 Ω impedance of the transmitting cable, and the amplification of the received signal.

The base of the pyramid is positioned on an aluminum pedestal. With a height of about 30 cm the pedestal protects the fragile PVC pyramid from maintenance work at the KASCADE-array. In addition, this pedestal acts as a ground screen, and its size is of relevance for the antenna gain. More about the effects of the pedestal for the evaluation of the antenna gain will be discussed in section 3.1.2.

The antenna itself is a radiator consisting of two copper cables with a length of 1 m each placed in opposite tubes of the pyramid. The antenna is therefore a linearly polarized antenna. With an angle of $\approx 85°$ between the copper cables the length of the two arms correspond to $\lambda/2$ at 75 MHz.

The second set of LOPES consists of 20 antennas similar to the initial 10 antennas. The geometry and the pedestals are nearly the same, only the base frame of the PVC pyramid was omitted and the color changed from green to black. The actual height of these antennas is 1.7 m and with a base length of 2.0 m the opening angle is $\approx 90°$. The extension by additional 20 antennas increases the ability to measure lateral distributions of the radio emission.

The third type of antenna is a log-periodic antenna consisting of dipoles (LPDA). The antenna has an impedance and radiation characteristics that are regularly repetitive as a logarithmic function of the excitation frequency. This setup is called LOPES^{STAR} (Gemmeke et al. 2006; Krömer 2008) with STAR as an abbreviation of "Self-triggered Array of Radio Detectors". The approach is to develop on the basis of the EAS trigger information from KASCADE-Grande an antenna system that can operate independently and self-triggered. For applications in large scale experiments the test of such antenna systems is of importance, because in such an environment no dense EAS detector array will be available. The antennas can work as complementary detector, e.g. at the Pierre Auger Observatory.

[2] The word "array" is indicating the field of detector huts of the original KASCADE experiment.

Figure 3.1: Left: LOFAR prototype antenna. Right: LOPES^{STAR} type, LPDA. Inside the KASCADE-array the LOPES antennas are installed between the detector station. The pyramid geometry determines the receiving characteristics of the antenna. At two opposite sides of the pyramid the dipole antenna is placed, causing the inverted-V shape.

3.1.2 Antenna Gain

The inverted V-shape antenna used is not a simple dipole, therefore the receiving and emitting characteristics have to be modeled in detail. The reciprocity theorem in Electrodynamics implies that an antenna behaves the same for emitting and for receiving electromagnetic waves (Rohlfs 1986). The radio pulses in an EAS occur as electromagnetic radiation, which propagates in the medium air. The energy flux of an electromagnetic wave propagating in the free space is described with the Poynting vector:

$$\mathbf{S}(t) = \mathbf{E}(t) \times \mathbf{H}(t) \tag{3.1}$$

The electric field $\mathbf{E}(t)$ and the auxiliary magnetic field $\mathbf{H}(t)$ are used to describe the energy flux ($\mathrm{W/m^2}$) of the electromagnetic field. For the free space case the two quantities have a fixed phase relation, the vectors are perpendicular to each other ($\mathbf{E} \perp \mathbf{B}$) and the propagation direction, and their amplitudes are related with the impedance of the free space Z_{0_f} ($\left[Z_{0_f}\right] = \Omega$, Ohm):

$$Z_{0_f} = \frac{|\mathbf{E}(t)|}{|\mathbf{H}(t)|} = \sqrt{\frac{\mu_0}{\epsilon_0}} = \mu_0 c_0 \approx 120\pi\Omega \tag{3.2}$$

$$|\mathbf{S}(t)| = |\mathbf{E}(t)|\,|\mathbf{H}(t)| = \frac{1}{Z_{0_f}}\,|\mathbf{E}(t)|^2 = \frac{1}{\mu_0 c_0}\,|\mathbf{E}(t)|^2 \tag{3.3}$$

For other media than vacuum the permittivity ϵ_0 and permeability μ_0 are replaced by $\epsilon_0\epsilon_\mathrm{r}$ and $\mu_0\mu_\mathrm{r}$. The resulting impedance for the media is then given by $Z_{0_\mathrm{M}} = Z_{0_\mathrm{f}}\sqrt{\mu_\mathrm{r}/\epsilon_\mathrm{r}}$, which is for air only slightly different from the value for the free space. The permittivity ϵ_r in the atmosphere for standard conditions of temperature and

pressure is 1.00059, leading to an impedance reduced by 0.1Ω to a value of $Z_{0_{\mathrm{M}}} \approx 376.62$. For harmonic oscillations the absolute value of the Poynting vector $|\mathbf{S}|$ represents the instantaneous value of the power density and the time-averaged value is called irradiance.

At large enough distances r from an antenna one can assume a plan wave front and the total emitted power P_t which passes through the surface of the sphere F is:

$$P_t = \int_F |\mathbf{S}(t)|\,\mathrm{d}\mathbf{f} \tag{3.4}$$

$$= r^2 \int_{\phi=0}^{2\pi} \int_{\theta=0}^{\pi} S(\mathrm{r}) \sin\theta \mathrm{d}\theta \mathrm{d}\phi \;\; \mathrm{with\,r} \gg 1 \tag{3.5}$$

In case of an ideal isotropic emitter the power $P_{\mathrm{i}so}$ per surface element d$\mathbf{f}$ is the same over the whole surface of the sphere. This ideal case is not realized in practice. If electromagnetic radiation impinges upon a conductor, then it couples to the conductor, travels along it, and induces an electric current on the surface of that conductor by exciting the electrons of the conducting material. This effect is the skin effect (Lord Kelvin 1889). For a real antenna the power $P_{(\theta,\phi)}$ transmitted or received in a certain direction is only a fraction $G(\theta,\phi)$ of the power transmitted by an isotropic antenna $P_{\mathrm{i}so}$

$$P_{(\theta,\phi)} = G(\theta,\phi) P_{\mathrm{i}so} = \frac{1}{4\pi} G(\theta,\phi) P_t\,. \tag{3.6}$$

The gain $G(\theta,\phi)$ of an antenna can only being measured in the far-field where the wave front is approximately planar. The definition of the gain given above is sometimes referred to as the directivity of the antenna only. Losses due to the active balun and the coupling mismatch to the antenna are not included. For the LOPES setup we can not distinguish between theses losses and the directivity, whereas we can include these effects in an amplitude calibration (see chapter 4). Commonly the gain is given in logarithmic scale:

$$G(\theta,\phi) = 10 \log\left(G(\theta,\phi)\right) \;\; [\mathrm{dB}] \tag{3.7}$$

A proper description of the gain or directivity is needed in order to know the emitted or received power of the antenna. The antenna gain calculations were performed with the program package IE3D from Zeland company (see also www.zeland.com), a program using the multi pole expansion to calculate the electromagnetic properties of three-dimensional antennas. As input to the antenna gain calculations the real geometry of the LOPES antenna including the metal pedestal is used. The inverted-V dipole of the LOPES antenna has an opening angle of $\alpha \approx 85°$ or $\approx 90°$ which modifies the directivity pattern compared to a linear dipole.

For the definition of the ground an infinite plane is assumed and the electrical properties of this ground plane are similar to the real ground. Therefore resistance, ground humidity, and conductivity are chosen to be close to the actual condition at the antenna field. For the dielectric constant the value was set to $\epsilon_r = 3$ and a value of $\sigma = 0.01$ S m^{-1} was used for the conductivity. The simulation describes only the antenna itself, and therefore no antenna coupling to the electronic system was considered. A possible effect of mismatch between the antenna, the active balun,

Table 3.1: Excerpt from the first and last lines of the data table for the calculation of the LOPES antenna gain. The gain is divided into two components, G_θ and G_ϕ and according phases α_θ and α_ϕ are calculated.

Frequency [MHz]	Zenith θ [deg.]	Azimuth ϕ [deg.]	G_θ [dB]	α_θ	G_ϕ [dB]	α_ϕ
10	0	0	3.68	-90.88	-157.35	-90.85
10	0	10	3.55	-90.88	-11.53	89.12
...						
10	0	360	3.68	-90.88	-157.35	-90.85
10	5	0	3.63	-90.88	-113.14	-1.21
...						
100	180	350	-1931.24	0.00	-1946.31	0.00
100	180	360	-1931.10	0.00	-2044.18	0.00

and a subsequent low-noise amplifier cannot be seen directly from the calculations, but will be included in the calibration procedure.

The calculations range from 10 MHz to 100 MHz and result in a gain value for each frequency (1 MHz step size) and direction (zenith angle θ with 5° and azimuth angle ϕ with 10° step size) of the incoming signal, which can be displayed as a directional diagram.

Table 3.1 gives the output format of the calculations, with columns as for the frequency ν in MHz, azimuth angle ϕ in degree, zenith angle θ in degree, zenithal component of the gain G_θ, phase for the zenithal gain α_θ, azimuthal component of the gain G_ϕ, and phase for the azimuthal gain α_ϕ, respectively.

The definition of a complex antenna gain $\mathbf{G}_{(\theta,\phi)}$ with phase α needs the information of the components in spherical coordinates (table 3.1). With these values the complex gain can be calculated like:

$$\mathbf{G}_{(\theta,\phi)} = 10^{(G_\theta/10)} \cdot \exp(i\alpha_\theta) + 10^{(G_\phi/10)} \cdot \exp(i\alpha_\phi) \tag{3.8}$$

From the complex gain $\mathbf{G}_{(\theta,\phi)}$ one can directly get the real gain $G(\theta,\phi) = \left|\mathbf{G}_{(\theta,\phi)}\right|$

In figure 3.2, left panel, a vertical cut through the calculated directivity pattern is shown and the antenna gain value $G_\mathrm{r}(\theta, 180°, \nu)$ are displayed for different frequencies. The main lobe of the antenna has a -3 dB angle of $\approx 70°$. Side lobes are strongly suppressed due to the pedestal of the LOPES antenna and the ground plane conditions. This -3 dB angle is the full width half maximum (FWHM) angular beam width. For zenith angles θ above 60° the gain drops significantly compared to the line of symmetry (in the zenith, $\theta = 0°$).

In figure 3.2, right panel, a horizontal cut through the calculated diagram at a fixed zenith angle of $\theta = 45°$ is shown. The visible main lobes for such a zenith angle display an oval shape and the dipole origin is only indicated by the constriction along the y-axis at gain zero on the x-axis. It is obvious that the antennas prefer radio pulses from north or south as a result of their orientation (i.e. here the east-west direction).

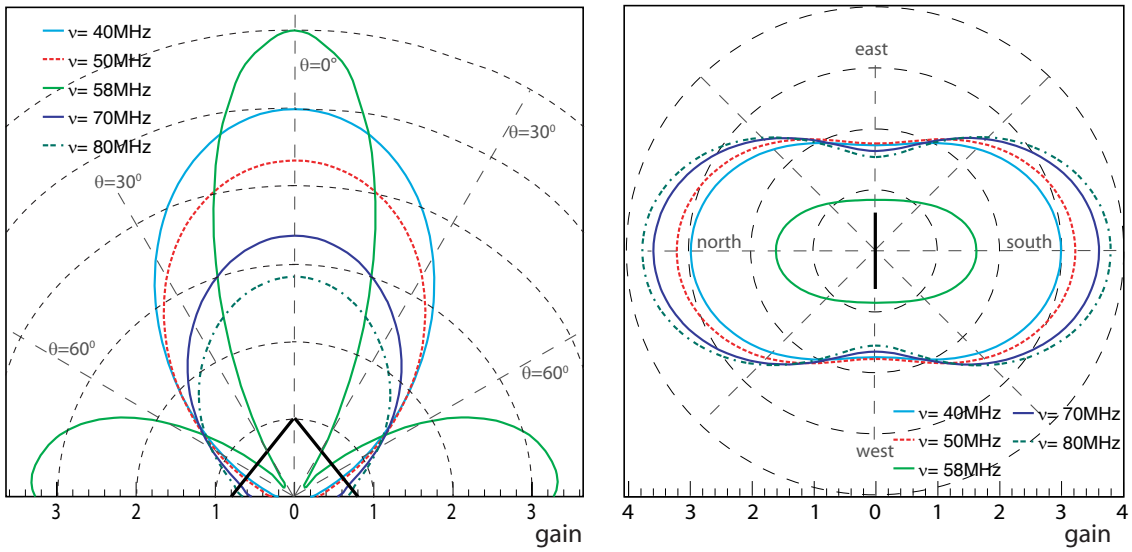

Figure 3.2: Left: Antenna gain $G_{\mathrm{r}}(\theta, 180°, \nu)$ of the LOPES antenna in the $\vec{E}$-plane (zenithal sensitivity). The antenna is illustrated by a triangle in the center of the x-axis and lies in the image plane. Right: Antenna gain $G_{\mathrm{r}}(45°, \phi, \nu)$ of the LOPES antenna for a fixed zenith angle (azimuthal sensitivity). This can be considered as a horizontal plane cut at $\theta = 45°$. The dipole antenna lies on the y-axis.

Another way of visualizing the directivity pattern is displayed in the left panel of figure 3.3, where the dipole is oriented horizontally and the color-coding for brighter colors indicates higher gain values. This reveals once more that the linearly polarized antenna has an elliptical azimuthal sensitivity and for high inclinations the antenna gets almost insensitive, which was intended by choosing this geometry.

A striking feature is the behavior at 58 MHz, visible as horizontal side lobes in figure 3.2, left panel, or clearly pronounced in the right panel of figure 3.3. The calculations indicate that there is a resonance induced from the 2 m by 2 m metal pedestal below the antenna. The resonance seems to be sharp and should be visible in a calibration procedure and will be checked by specific measurements (section 4.2.5).

3.1.3 Electronics of the LOPES System

The antennas are connected to low noise amplifiers (LNA). The signal is then transmitted via a coaxial cable to one of three stations where it is again amplified, filtered and digitized. The three stations with 10 antennas each are operated by independent electronic chains and data acquisition systems. One of these three stations was forming the initial LOPES10 experiment. That means that for the initial LOPES10 setup and the extension LOPES30 not the same batch of production of the analogue electronic components were used.

Figure 3.4 displays the scheme of the LOPES electronics in more detail. For the overall performance of the LOPES antenna system, the analog part is most crucial. In the transmission chain from reception of the radio pulse to its digitalization, there are some active and passive components that influence the amplitude and phase of the radio signal:

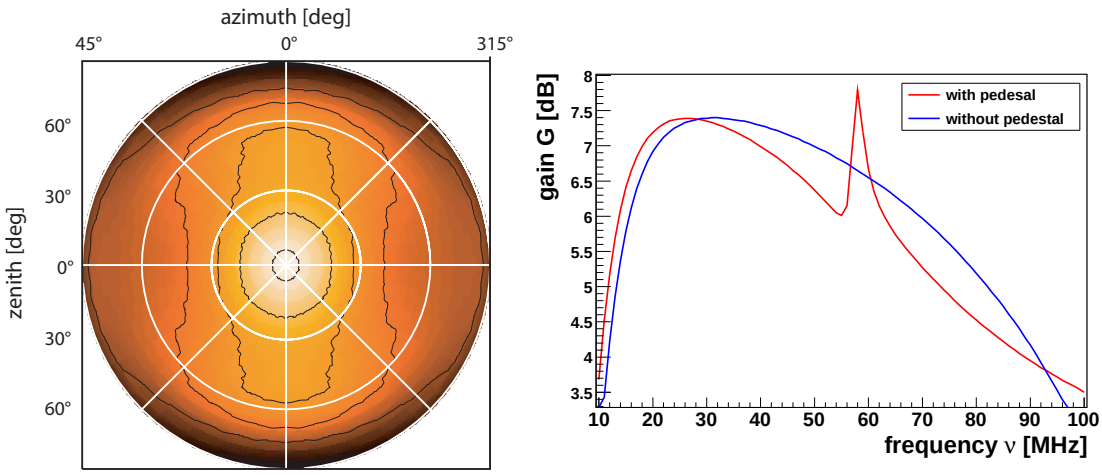

Figure 3.3: Left: Modeled antenna gain patterns for the LOPES antenna at 60 MHz. The polar plot shows the zenith in the center and the horizon at the plot edges, with a horizontally oriented antenna. The gain is color-coded and ranges from black (minimum) to the white (maximum). Dark contours are plotted in steps of 20% of the gain. Right: Comparison of the gain in the zenith for a LOPES antenna with (red line) and without (blue line) a pedestal. For the antenna calculation with pedestal a sharp resonance is obtained at 58 MHz.

Active balun A negative feedback amplifier with good linearity and noise performance is used to operate as the impedance match between the antenna and the coaxial cable. A bias-tee in between acts as power supply for the amplifier.

Coaxial cable All signals received by the antenna at the field have to be transfered into the three stations. The RG-213/U coaxial cables used have two different lengths, either 100 m or 180 m depending on the antenna position on the field, with an attenuation at 60 MHz per 100 m of ≈5 dB.

Amplifier and filter After the signal transmission over the coaxial cable to the Receiver Module LOPES [RML], the analog HF-signal has to be amplified again (+16 dB), and afterwards the anti-aliasing filter suppresses the strong FM-band transmitters above the frequency range of 40-80 MHz. The necessity of steep edges for the filter results in an effective usable frequency range of 43-76 MHz.

A/D-converter The amplified and filtered signal is digitized with a 80 MHz sample clock that is provided from a clock distribution board. The sampling rate used represents a sampling in the second Nyquist domain of the ADC. With 12-bit resolution and a maximum input voltage of ±1 V the ADC can detect weak radio signals while it is not saturated by the RFI. The digitized signal is converted into an optical signal and transfered via fiber optics.

Clock distribution boards To provide all LOPES antennas with a common clock, a clock distribution board generates the needed 40 MHz and 80 MHz signals as a rectangular wave. These are distributed via coaxial cables (RG-58C/U) to the three stations, and, after refresh, multiplied ten times in so-called slave clock distribution boards.

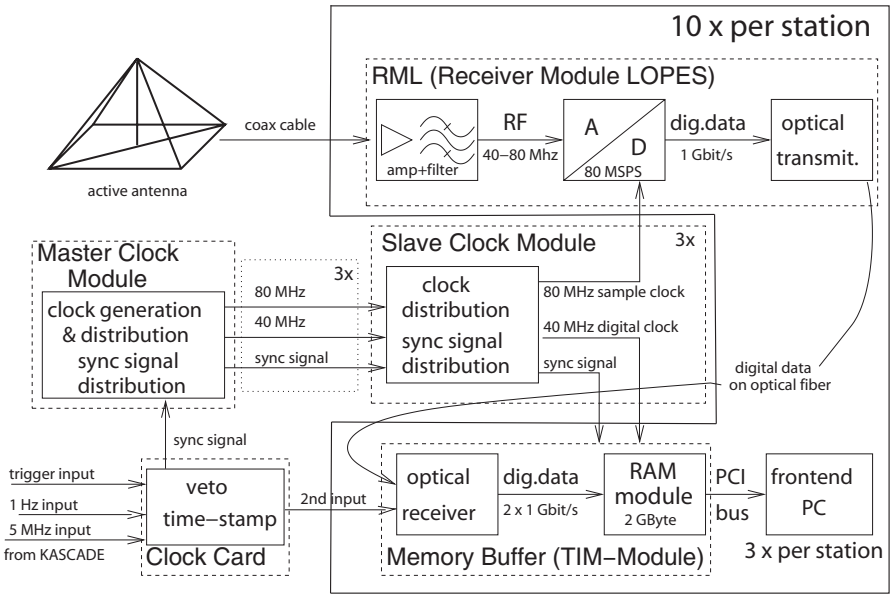

Figure 3.4: Scheme of the LOPES electronics: Incoming radio pulses from EAS are received with the active antenna and transmitted via a long coaxial cable (RG-213) to the Receiver Module LOPES (RML). The amplified and bandpass filtered analog signals are digitized with a 12-bit A/D converter. After the optical fiber transmission the signals are stored in a memory buffer. Trigger from KASCADE-Grande are distributed by a master clock module to each station and finally transmitted to the front-end PC for data read-out.

Memory module Each memory module has two optical inputs and a standard PCI-connector. The optical receiver is connected to a 2×1 GB memory (PC133 style). The storage of the digitized data in the memory ring-buffer allow us to write data continuously. For a 12.5 nsec sampling rate and a used 16-bit short integer for the data samples the 10^9 bytes of memory can store up to 6.25 seconds of data. For 10 antennas per station, 5 memory boards are needed, hosted in 3 front-end PC.

Clock card The PCI clock card is hosted in one front-end PC and has a 1 Hz, 5 MHz, and TTL-input, as well as one TTL-output. The clock card processes the KASCADE-Grande trigger (as TTL input) and relays the trigger pulse to the master clock distribution board. If required, a software trigger can be created at the TTL-output. The DAQ software is connected with the clock card to receive timestamp information.

The power support is arranged per station by low emission power supplies, providing 3, 5, and 15 volt DC for the analogue and digital components. The stations are air conditioned and kept at an almost stable temperature. The front-end PCs are connected within a local area network and the DAQ is controlled by a central PC.

3.2 Operation

The inverted-V antennas are dipoles with two arms. A single dipole is only sensitive to one polarization direction. For a geomagnetic emission mechanism and showers coming from the north or south, the expected signal is dominantly east-west

polarized. This was already the result of analytical calculations (Huege & Falcke 2003) and this determined the LOPES configuration. The dipole antennas have been oriented at first in east-west direction.

The LOPES setup is operated by a central DAQ-PC that sets up software clients on the front-end PCs. In order to perform a coincidence measurement with the KASCADE-Grande experiment, the clock card receives a 1 Hz and 5 MHz clock from KASCADE-Grande and the DAQ is generating a time stamp from this information applied to all data files. The data is ring-buffered for up to 6.25 seconds and read-out only if an external trigger arrives (from KASCADE-Grande, see also section 3.2.2). Then the central DAQ-PC collects $2^{16} \times 12.5$ ns $= 819.2\,\mu$s samples of data around the trigger from all 30 antennas, adding a KASCADE-Grande time-stamp and storing them as one LOPES-event file.

During thunderstorm conditions, the record length of the time series of 2^{16} will be extended, see section 3.3.2. In this mode the resulting dead-time of the LOPES-system will be increased, as the data transfer and LOPES-event file writing process takes more time.

3.2.1 Antenna Configurations

A layout of the experimental setup is sketched in figure 3.5. The figure indicates the KASCADE-Grande stations as blue squares, the KASCADE-array in the upper right corner is illustrated as 4×4 squares (with the upper cluster).

During the operation of the LOPES experiment since 2003, the number of antennas as well as the positions on the field have changed. For the LOPES10 configuration always two antennas per KASCADE cluster have been setup, (for the definition of cluster see section 3.2.2) whereas four inner and one outer cluster were equipped. All antennas were oriented in east-west direction, only able to measure one polarization component of the radio pulse. The maximum baseline was about 156 m for this antenna field. In this configuration LOPES has taken data from August 2003 until September 2004.

From end of 2004 until mid of 2005 LOPES was extended by 20 more antennas - LOPES30. A major change in hardware was necessary due to the fact that two new stations had to be set-up and be provided with the trigger and the central clocks. The enlarged maximum baseline about 265 m is across the KASCADE-array from the upper left to the lower right corner.

From first analyses of the LOPES data it was recognized that there is strong RFI occurring right after the radio pulse. To investigate and avoid the RFI next to the shower core of the EAS (where the largest energy deposit in the detector stations occurs), four antennas have been placed outside the KASCADE-array on a free meadow on the west-side. From November 2005 to December 2006, LOPES has taken data in this configuration. This is the data set of the analysis described in chapter 5.

A first change of the LOPES setup regarding full polarization measurements was done in August 2006, when 3 antennas were chosen to be also equipped with a north-south oriented dipole. Therefore 3 existing antennas were moved and their cables underground redirected. Since this time antenna #27 is measuring the second

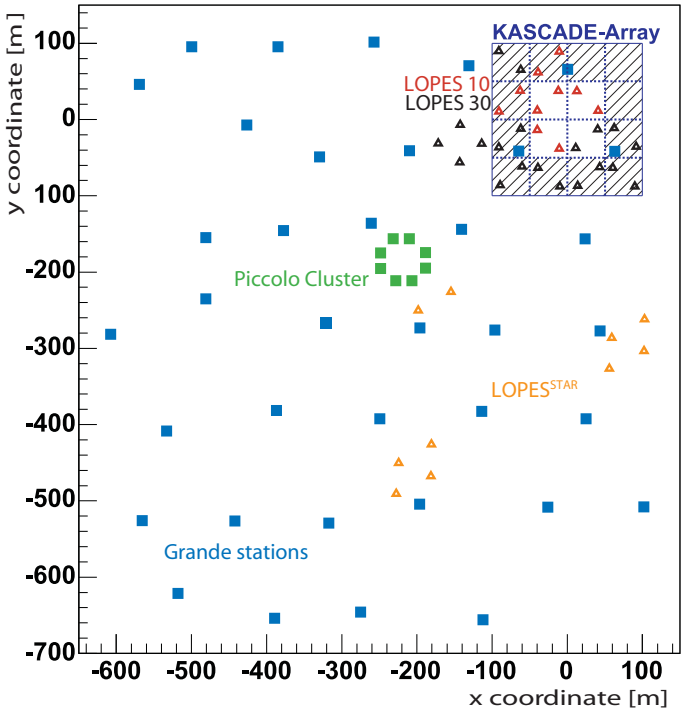

Figure 3.5: Sketch of the KASCADE-Grande and LOPES experiments: The KASCADE-array particle detectors and the distribution of the 37 stations of the Grande array are shown. The locations of the 30 LOPES radio antennas as well as the 10 LOPES$^{\mathrm{STAR}}$ antennas are displayed.

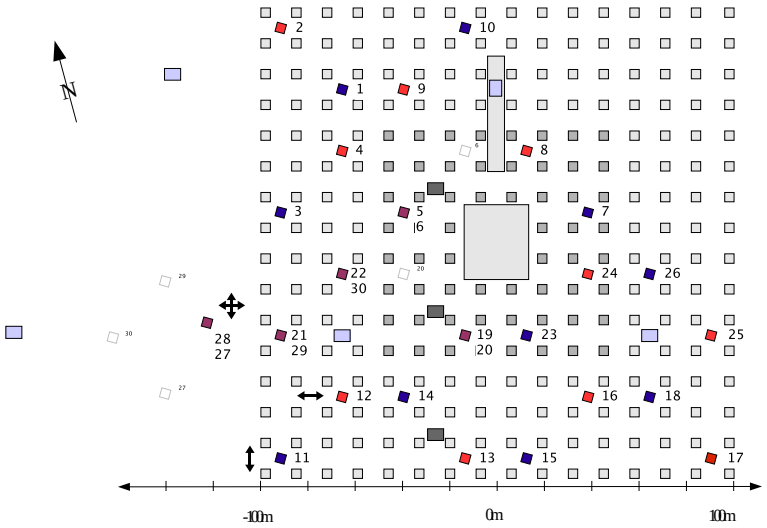

Figure 3.6: The LOPES antenna field is shown at the KASCADE-array after a reconfiguration end of 2006 to measure with 10 antennas in north-south (blue squares) and 10 antennas in east-west (red squares) orientation. The five purple squares are indicating the five dual polarized antennas. The regular grid of grey squares mark the KASCADE-array huts. The five Grande stations are indicated as light-blue rectangulars.

polarization at antenna #28, antenna #29 was redirected to antenna #21, and antenna #30 to antenna #22.

After successful tests and verification of the reliability of this configuration, the LOPES experiment was reconfigured once again (December 2006) to its present configuration, see section 3.6. The verification of the reliability is subject of section 4.2.4.2. Since this time, there are two antennas more operating in a dual-polarization mode. Antenna #6 joins now antenna #5 and antenna #19 moved to antenna #20. In all cases the antennas equipped with both polarizations belong to the same electronics station. Furthermore, we have rotated half of the antenna to single north-south configuration (antenna #1, #3, #7, #10, #11, #14, #15, #18, #26). Excluding the dual-polarized antennas, 10 antennas stayed in east-west polarization (antenna #2, #4, #8, #9, #12, #13, #16, #17, #24, #25). In this configuration the optimum between maximum baseline and homogenous ground coverage for the east-west and north-south oriented antennas was searched for. In total 15 antennas are oriented in north-south, 15 antennas in east-west, 10 single north-south, 10 single east-west, and 5 with both polarizations.

The 10 LOPES^{STAR} LPDA are operating since 2006 and taking data with both polarizations. The trigger condition from KASCADE-Grande is a single seven-out-of-seven (7/7) coincidence of Grande stations.

3.2.2 KASCADE-Grande Trigger

The aim of the LOPES experiment is to correlate the observables of the radio measurements with the shower properties provided by the particle air-shower experiment KASCADE-Grande. For this reason LOPES is triggered by KASCADE-Grande and uses the reconstructed shower data as input for the pulse analysis. In other words, the shower core position at ground and the direction of the shower axis are used as starting values for the reconstruction of the radio signals.

KASCADE-Grande consists mainly of stations equipped with scintillation detectors, where 252 stations compose the KASCADE-array, and further 37 large stations the Grande array. The KASCADE-array is a regular grid of detector stations with a spacing of 13 m. On the 200×200 m^2 area of the KASCADE-array the detector huts have an effective detection area of about 3.2 m^2 each for both detector types. In each station there are up to four electron/gamma-detectors and an muon-detector under an iron-lead-absorber. The absorber has about 20 attenuation lengths and serves as shielding against the electromagnetic component of the EAS. Only muons with energies greater than 230 MeV are able to penetrate the absorber. Table 3.2 gives an overview of the detector components in the KASCADE-array and the Grande extension. For the KASCADE-array 16 detector stations (huts) form a so-called cluster with an electronics container in the center. The 16 clusters act as independent shower experiment and generate a trigger. The mean energy deposit of the minimum ionizing particle (m.i.p.) is found to be 12 MeV (Antoni et al. 2003), and with 8 detector stations above 1/3 m.i.p. a cluster trigger is generated. When a trigger is generated within one cluster all data with less than 8 μs time difference to the trigger time are collected. The resulting trigger rate for KASCADE-Grande is about 4-5 Hz.

The trigger condition for LOPES is generated from the cluster triggers and has to have at least 10 out of 16 clusters. This trigger threshold is set in order to have

Table 3.2: The table lists the KASCADE-array and the Grande detector components with their characteristics.

Detector component	Particle type	Energy Threshold	Area
KASCADE-array			
liquid scintillator	e/γ	5 MeV	490 m^2
plastic scintillator	μ	230 MeV	622 m^2
Grande extension			
plastic scintillator	$e/\gamma/\mu$	5 MeV	370 m^2

only high energy showers and the rate is only about 0.03 Hz. An expected positive detection of the radio signal should be even significantly above this threshold.

The investigation of high energy showers at larger distances needs a trigger condition from Grande. The irregular grid of Grande is organized in so-called trigger hexagons. Each trigger hexagon consists of 6 Grande stations surrounding an inner station. The seven-out-of-seven (7/7) coincidence is generating a trigger if an energy deposit above threshold is registered in all stations. Since 18 December 2006 a coincidence of the trigger hexagons 9, 10, and 13 leads to a further trigger signal for LOPES. This trigger condition includes 12 stations in the center of the Grande detector field. The rate for the trigger condition is very low, below 10 events per hour.

The larger distance of the LOPES antenna field also helps to avoid RFI from the particle detectors that happens very close to the shower core and mostly for the closest antennas only. The logic combination of the two trigger conditions is set to OR and an online discrimination is not possible as the same TTL-pulse is used.

3.2.3 Monitoring of the DAQ

During the operation of the LOPES experiment the performance of the antennas is checked regularly. For this purpose two possibilities exists: daily dynamic spectra and a monitoring of the voltages at the ADC.

The daily dynamic spectra[3] are representing a whole day with the power received by the LOPES antennas per event and averaged over all antennas. This gives a vertical segmentation that is not equidistant in time. A vertical column represents 819 μs of data, but the average trigger rate per hour is relatively constant. The ordinate shows the frequency range of LOPES, 40–80 MHz, with 4096 frequency channels and $\approx$ 10 kHz bandwidth. Fourier transforming the 2^{16} samples in one event yields 2^{15} frequency channels with 1.2 kHz bandwidth, after which blocks of eight channels are averaged to obtain the $\approx$ 10 kHz bandwidth. The intensity in the plots represents the averaged logarithmic power from all antennas. Averaging means that all signals from the entire sky received by each antenna are averaged in the plots. The color map is logarithmic, has fixed limits for all plots and the values are in arbitrary units.

In figure 3.7 a daily dynamic spectrum is shown. Some brighter horizontal lines can be identified at fixed frequencies, which indicate man-made Radio Frequency

[3]Daily dynamic spectra are available at www.astron.nl/lopes/brosedata

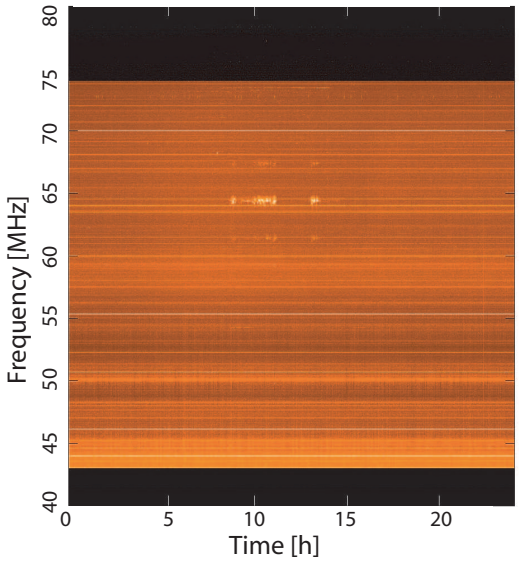

Figure 3.7: An example of a daily dynamic spectrum. The brightness of the spectrum is a measure of the averaged power received by all antennas at a certain event, shown in an arbitrary normalized logarithmic scale. Note that the x-axis is not equidistant in time, but each vertical line represents a recorded event of the day.

Interference (RFI). With the LOPES antennas it is possible to observe phenomena like solar bursts which appear as bright, vertical strokes dying out towards lower frequencies. Also strong lightning events will appear in our data.

Another monitoring is performed on the basis of single events. A mean noise level is calculated from the counts $C_{ADC}(n)$, that result from the conversion of the voltages in the ADC. There are two time ranges $L_1 = -399.6$ μs to -143.6 μs and $L_2 =$ 207.6 μs to 399.6 μs in the data set that are used to calculate the mean noise level S_{mean}. The absolute value is taken and summed up like:

$$S_{\mathrm{mean}} = \frac{1}{L} \sum_{n}^{L} |C_{\mathrm{ADC}}(n)| \tag{3.9}$$

The sum of all $C_{ADC}(n)$ goes over $L_1 + L_2 = L = 35840$, which is 54% of the data length. The graphical overview shown in figure 3.8 gives the mean noise level S_{mean} in all antennas (one column for each antenna) as color code. The monitoring is scheduled to run every 20 minutes and the last saved event is evaluated. The last results are graphically prepared and attached at the top of the figure, therefore, the last 8 hours can be checked immediately online [4].

3.3 Electric Field Conditions

The almost static atmospheric electric field is even present under fair weather conditions (Le Monnier 1752). The typical field strengths at ground are of about 100–150 Vm^{-1}. But, especially inside thunderclouds large electric fields can be present,

[4]The LOPES internal web page is available at http://www-ik.fzk.de/~nehls/lopes/log.html

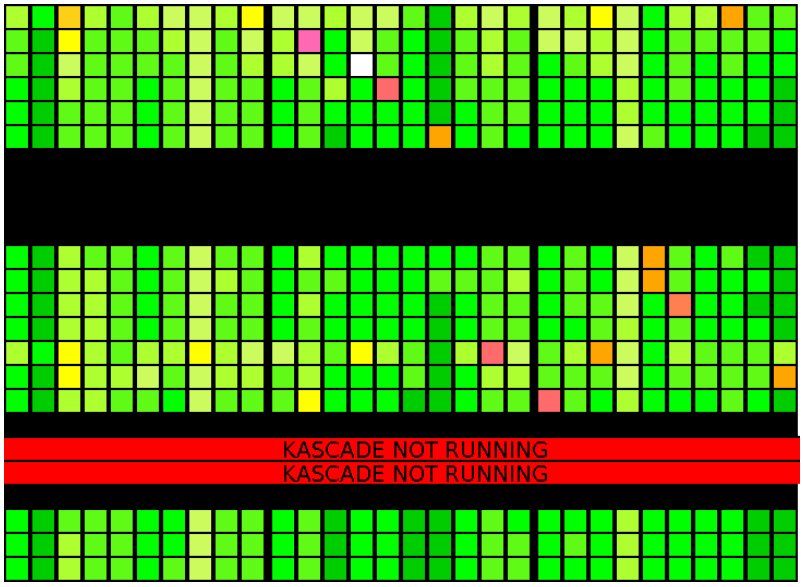

Figure 3.8: Example of the DAQ online monitoring for LOPES. The 30 columns represent one antenna channel each and a raw is attached at the top every 20 minutes. The color code indicates the mean noise level per antenna. A detailed description can be found in the text. Black lines indicate that there was no new event saved since the last evaluation. The graphical overview was obtained during a calibration campaign, were the calibrated antenna shows an increased signal level. The break over lunch time is in the part of the graph, where "KASCADE NOT RUNNING" is indicated.

where field strengths can reach values of up to 100 kVm^{-1}. Due to this fact a monitoring of the electric field can help to evaluate the measured radio signals.

3.3.1 Electric Field Mill

An Electric Field Mill is an electro-mechanical device which measures the strength of a static electric field. One or more electrodes are alternately exposed to and shielded from the field to be measured. The electric current which flows to and from the electrodes is proportional to the strength of the electric field.

For the LOPES setup the electric field meter CS110 from Campbell Scientific[5] is mounted on top of the roof of cluster 6 (see figure 3.9, left). The CS110 electric field meter measures the vertical component of the atmospheric electric field. It can be used for lightning warning applications. The CS110 uses a reciprocating shutter instead of the traditional rotating vane field mill, a feature that improves DC measurement performance, reliability, and reduces power consumption.

There is also mounted a defined ground plate on top of the cluster station, which is connected to the Earth ground potential. This ensures a suppression of static field changes from surrounding disturbance sources. The field meter runs continously and is connected to the DAQ system of LOPES.

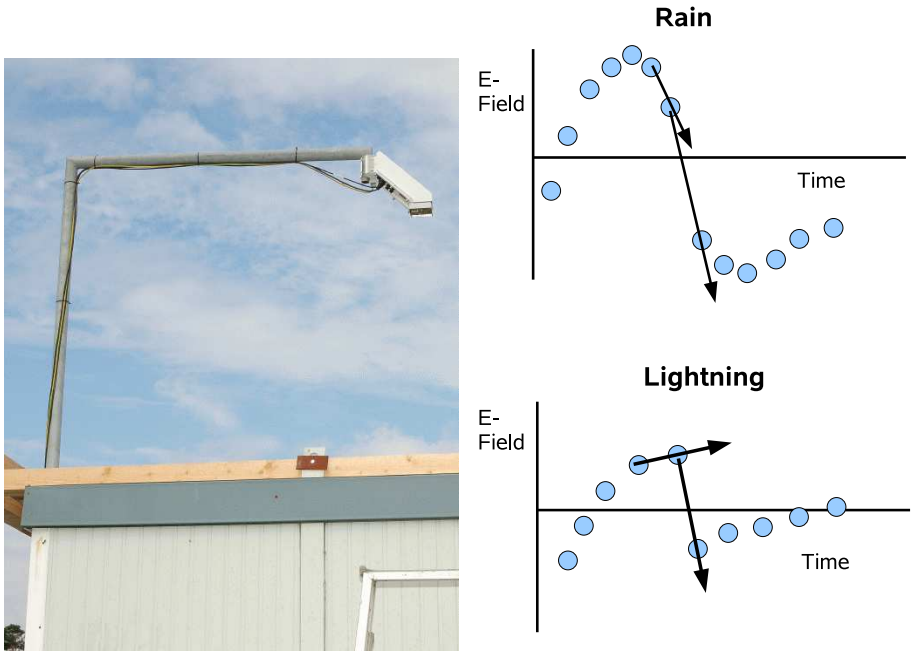

Figure 3.9: Left: Mounted CS110 electric field meter on top of a KASCADE cluster station. The field meter is mounted above a grounded aluminum plate. Right: Two electric field scenarios, for rain a smooth change can be seen (indicated by the arrows) and for lightning there are jumps in the slope.

3.3.2 Thunderstorm Mode

The electric field mill is used as lightning detector and operates for the LOPES DAQ as a discriminator between fair weather conditions and thunderstorm conditions. The aim is to change the way of data taking during thunderstorms and investigate possible correlations between lightning activity, EAS, and radio emission from lightning initiation processes.

For this purpose a software solution is implemented in the LOPES DAQ that distinguishes between thunderstorm condition and all other weather situations. Each three minutes the last 15 minutes of the electric field measurement are evaluated in the following way:

1. For each minute of the $15 \times 60 = 900$ second of data V_i an average value V_{avg} and the standard deviation $\sigma_{1\text{min}}$ are calculated.

2. A loop is performed over the whole data set until there is a field strength exceeding fair weather conditions, $|V_{i-1}| > E_{\text{thres}}$. This threshold suppresses distant thunderstorms, as well as local disturbances.

3. A significant jump size, $|V_i - V_{i-1}| = |\Delta V_J| > E_{\text{jump}}$, is required to only consider close discharge discontinuities.

4. The jump size has to be significant compared with the average field for this one minute, $|\Delta V_J| > B \cdot \sigma_{1\text{min}}$. AND also the jump size for $V_i - V_{i-2}$ has to be larger than this threshold.

[5] http://www.campbellsci.com/electric-field-meter

5. A slope change between two neighboring points, $|DS| > \alpha$, has to found, with:
   $DS = (\Theta_1 - \Theta_2) \cdot 180/\pi$ and width w=3
   using the following quantities:
   $\Theta_1 = \arctan((V_{i-1} - V_{i-1-w})/w)$,
   $\Theta_2 = \arctan((V_{i+w} - V_i)/w)$, and
   OR
   there is a sudden lightning discharge $|\Delta V_J| > S \cdot \sigma_{1\mathrm{min}}$.

6. ONLY if the software was passing all conditions the unique record number is written out and the LOPES DAQ changes with the next event into the thunderstorm mode (TS-mode)!

The upper panel of figure 3.10 shows 15 minutes of electric field data and larger 9 jumps due to lightning. The TS-mode was active for this time.

The following parameters are used to optimized the TS-mode trigger and suppress false trigger from other features of the electric field.

$E_{\mathrm{thres}} = 500$ V/m

$E_{\mathrm{jump}} = 300$ V/m

significant factor B=2

angle difference $\alpha = 1^\circ$

sudden jump S=15

In TS-mode, the DAQ will change the read-out block length for an antenna data block from 2^{16} samples $\times 12.5$ ns $= 819.2\,\mu$s to 2^{19} samples $\times 12.5$ ns $= 6553.6\,\mu$s. The block length is no longer symmetric around the expected position of the KASCADE-Grande trigger, rather the data block is extended at the end by 5734.4 μs.

Since the implementation of the TS-mode three thunderstorms occurred. An analysis of the data after the summer season will be possible with much better statistics, e.g. at June 2^{nd}, 2008 the TS-mode was active (lower panel figure 3.10).

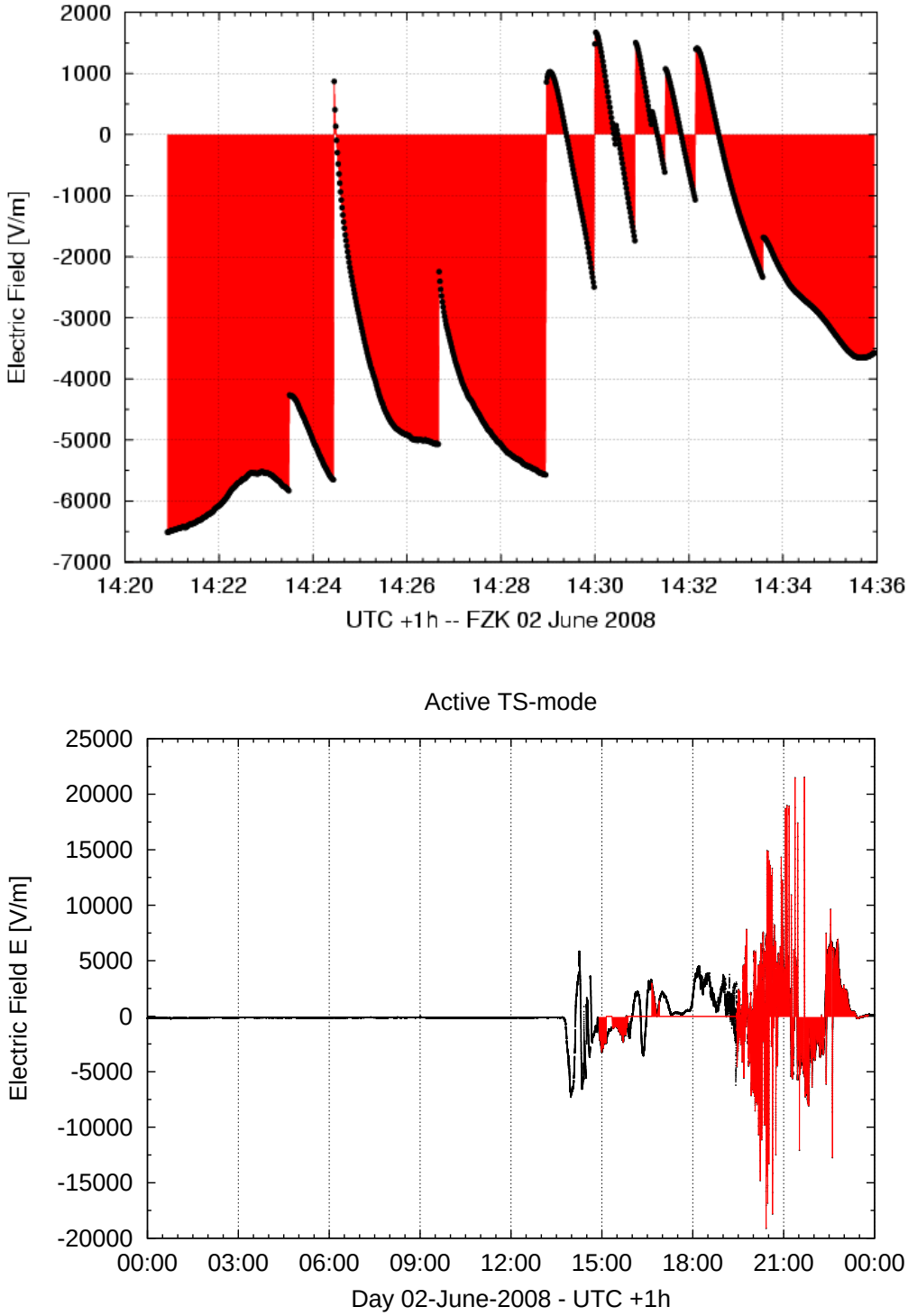

Figure 3.10: Example of an occurred TS-mode trigger (upper panel). The LOPES DAQ has switched from normal data taking into the TS-mode at June 2^{nd}, 2008 between 7 pm and 11 pm for a strong thunderstorm (lower panel). The fair weather condition with ≈ -150 V/m appears as flat line for most of the day.

4. Data Calibration

Measurements with the LOPES antennas aim to investigate the transient radio emission from EAS. At the antenna field the received radio signals are transfered and converted into voltage values. To analyze the data the temporal relation and absolute measure in terms of electric field strength has to be known, i.e. one has to correct all instrumental effects before dealing with physical quantities. This requires a correction of system delays as well as one needs an absolute amplitude calibration. For such a calibration one needs reference signals that can be used to correct instrumental delays and amplitude values. In this section the calibration methods applied for the LOPES system are described.

4.1 Delay Calibration

LOPES is an interferometric instrument being able to perform beam forming by time shifting in a certain direction. Therefore, instrumental signal delays have to be known for all antennas with high precision. The order for this timing precision has to be below the sampling rate of 80 MHz, respectively 12.5 nanoseconds. The aim of the delay calibration is to correct for system introduced delays per individual channel continuously over the running time of the experiment. Important in this context are effects from unequal aging of the parts of the electronics, tolerances in manufacturing, and different operation temperatures. Due to the three DAQ sub-systems the trigger has to be provided at three different places resulting in a clustering of the delays according to the antenna assignment. All this causes a variation of the delay for the 30 individual channels. In addition, the trigger distribution to the TIM module and the ADC board can cause two sample jumps, due to a 40 MHz sub-clock used to synchronize the ADC and the data transfer via fiber to the TIM module. The global delay has to be corrected for this effect. This requires a known reference signal that is present in the data at each individual event, which delivers reliable timing information.

4.1.1 Delay Calibration Using the Sun

The sun is a strong radio source, especially during solar bursts. Then the sun becomes by far the brightest source in the sky at MHz frequencies. In figure 4.1

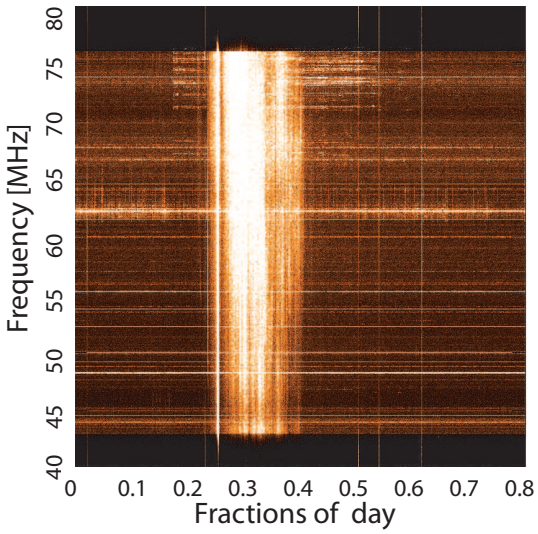

Figure 4.1: Dynamic spectrum from October 28, 2003 averaged over all antennas. At that day a solar burst was occurring and recorded in the LOPES data (frequencies range 43-76 MHz) for a couple of events. The x-axis are data files, which are not equidistant in time. The color code represents the recorded power in an arbitrary normalized logarithmic scale.

the dynamic spectrum of October, 28^{th} 2003 is shown, revealing the strong solar burst as a bright vertical strip. LOPES does not image the sun as an extended source and this allows us to use the radio signals from the sun as a delay calibration source. The absolute scale of the timing is of minor importance, as we do not perform comparisons between other radio antenna arrays. Hence only the relative delay between the individual LOPES antennas has to be known.

These relative delays are obtained by choosing one antenna as a reference, and then perform the following steps for all remaining antennas:

a) From the positions of the antennas and the sun position at the sky theoretical delays are calculated. Then the expected relative time delays to the reference antenna are given by the difference.

b) Calculation of the cross-correlation function for the time series of the antenna and the reference.

c) Estimate the time delay, at which the cross-correlation function has its maximum.

d) The difference between this time delay and the calculated expected delay is the instrumental delay.

For example after, October 28, 2003, time delays estimated over 6 solar burst events could be averaged and a complete delay calibration of the LOPES experiment performed.

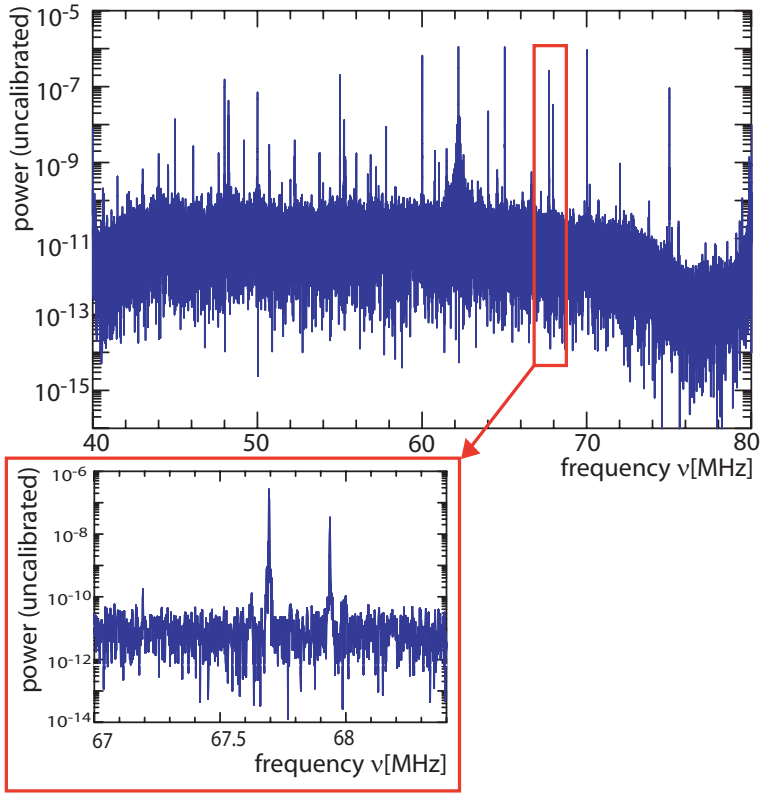

Figure 4.2: Typical uncalibrated LOPES raw signal of one antenna in the frequency domain. The zoom-in shows two audio signal carriers from a TV transmitter at 67.70 MHz and 67.92 MHz in more detail.

However, the method depends on the presences of solar bursts in the LOPES data. If there are non available, the delay calibration has to be performed by different methods. After 2003 the sun runs into its period of minimum activity and only a few bursts happened since then. Therefore, this delay calibration method can presently not be used.

4.1.2 Phase Correction with a TV-Transmitter

The information about the relative delays obtained during a solar burst is used as first order correction of the delays in the system. For each recorded data-set, i.e. individual events, the validity of the delay calibration has to be checked again. For example, the possible two sample jumps for individual antennas have to be detected and the data corrected for. This is done by monitoring the relative phases of a TV transmitter visible in the LOPES frequency range.

In figure 4.2 an uncalibrated power spectrum from a LOPES-event file for a single antenna is shown. Many narrow band radio emitters exceed the noise floor by orders of magnitude, but only a few of them are stable in time. The two audio carriers of a TV-transmitter in the LOPES band are shown in the zoom-in of figure 4.2. The video carrier and the two audio sub-carriers are strong enough that they are visible in every antenna every time. This TV-broadcasting station is called Raichberg:

Location: Albstadt (Onstmettingen)

Frequencies: Video carrier: 62.25 MHz
Audio carriers: 67.70 MHz, 67.92 MHz

Channel: E04

Distance: $\approx$ 120 km, no direct line of sight

From the known location of the TV transmitter relative delays can be calculated, or going to the frequency domain, i.e. Fourier transform of the time domain data, relative phases can be calculated.

The TV-transmitter is not seen directly be the LOPES antennas, but the signals reflected at the ionosphere receive them. However, the relative phases should be reasonable stable over time, at least within one data-set. A comparison of just one single frequency leaves over ambiguity of the phase. Shifts higher than the period at this frequency can not be corrected. But using three frequencies this ambiguity can be reduced. Not only delays by a small fraction of a sample time, but also shifts of an integer number of samples can be detected and therefore corrected for.

To calculate the phase corrections for the antennas some intermediate steps are needed. The resolution in the frequency domain is 1.22 kHz and the exact frequencies of the three carriers are not falling exactly within one frequency bin. The bins with the most power are searched and the according phases are used for the calculation of the relative values. Then the difference between determined phase from the data-set and the expected phase is calculated, showing the residual phases $\Delta\phi_{\nu_1,\nu_2,\nu_3}$. The absolute sum of these residual phases $\Delta\phi$ has to be below 150°, otherwise shifts by integer number of samples between -32 and +32 are tried. $\Delta\phi = 150°$ corresponds at $\nu = 80$ MHz to $\Delta T = 1/\nu\Delta\phi/2\pi = 1.7$ ns, or to a shift of 0.14 subsamples that is accepted as timing uncertainty for an antenna. If this value is exceeded and none of these shifts produces small residual phases the corresponding antenna is flagged as bad. Finally a delay correction is applied to the single antenna data, arising from the residual phase and possible multi sample jumps.

Unfortunately, terrestial analog TV is no longer supported and in a first step the emitting power of Raichberg was reduced at September 11^{th}, 2007. Finally at November 27^{th}, 2007 the TV-transmitter was shutdown. Therefore, this used TV-transmitter is no longer available for performing a delay calibration and another solution is needed in order to correct the instrumental delays for each data-set. There are two possibilities: One can improve the timing of the hardware in such a way that no delay correction is needed for each data set and a measure from time to time in the laboratory can be used to check changes in the system. But more sophisticated is to replace the solar burst and the TV-transmitter phase check by a controlled self-made reference source.

4.1.3 Self-made Reference Source

During operation time by a crash due to thunderstorm lightnings, there have been changes at the hardware of LOPES that required a new delay calibration, like done with solar bursts. Especially the trigger signal distribution to the three DAQ sub-systems was improved and this modified the time delays in the distribution system. As solar bursts are not very frequent during the solar minimum of the solar cycle,

another method has to be used for verifying the modified delays. The most promising method is the installation of a self-made reference emitter within the LOPES band. This reference source consists of a signal generator giving the superposition of sinus waves from two very stable quartzes. The emitting power for the two frequencies has to be significantly larger then the RFI background at the FZK. Choosing these two frequencies at 63.5 MHz and 68.1 MHZ one can avoid disturbances with the RFI, occurring mostly at even frequencies. As this will be a local reference source the received power will be significantly different for the closest antenna compared to the most distant antenna, which has to be taken into account for the calibration of the expected delays. There is mostly a direct line of sight from the field antenna to the reference source.

Presently the system works in a continuous mode, providing the two stable frequencies all the time, even if there are no data taken. The optimized solution will be a feedback solution, only emitting the reference signal within a certain time window after the KASCADE-Trigger has reached the LOPES DAQ. By that, the signal will have a discrete beginning and end in time which makes it usable like a solar burst. This possibility gives a combined method of solar burst and TV-transmitter delay correction and such a setup is presently under construction.

4.2 Amplitude Calibration

In general, to perform an amplitude calibration of the antennas there are two possibilities: Either the antenna characteristics are calculated theoretically and the electronic chain is calibrated in the laboratory, or the full chain is calibrated by an external source of known field strength. The former method was performed for the LOPES10 configuration and has only applicability for relative comparisons of radio emission and air shower properties. The latter procedure has the advantage of calibrating the full chain of the experiment, the antenna and the electronics simultaneously (end-to-end calibration). In addition, this approach provides the opportunity to investigate influences of environmental variables such as weather or ground humidity during shower measurements and to test the simulated antenna gain pattern.

Compared to the smaller initial LOPES10 setup with only one DAQ-station, for the LOPES30 setup larger variations in the behavior of the individual electronic channels can be expected. Therefore, a relative measurement of the electric field strengths, as it was performed for the initial LOPES10 setup, is not sufficient. Instead, an amplitude calibration is performed for the whole setup, including the full electronic chain of the antenna, i.e. LNA, cable, filter, and analog-to-digital converter.

For LOPES30 we have chosen a combination of end-to-end calibration with the determination of the behavior of individual components (Nehls et al. 2008). This hybrid method requires an antenna gain calculation. The LOPES antenna gain calculation have been described in section 3.1.2. However, experience within the LOFAR initial test station (ITS, Nigl et al. 2007) has shown that calibration measurements contain large uncertainties and can never fully cover the directivity pattern. Therefore, the amplitude calibration is mainly realized for the zenith direction. For other directions we will rely basically on antenna gain calculations. But the main characteristic of the antenna is described by its directivity and a full experimental test of these calculation results are important for the amplitude calibration.

Nevertheless, some test measurements are performed to verify the directivity as the method in principle allows to measure the full direction characteristics and to evaluate the antenna gain calculations (section 3.1.2).

As external source for the amplitude calibration one can use either an astronomical one, like the galactic background radiation (Dulk et al. 2001), or a man-made radio source. For the location of the LOPES-experiment the galactic background radiation is fully oblique due to man-made noise sources at Forschungszentrum Karlsruhe and can therefore not be used as reference source. What follows is the description how the LOPES30 amplitude is calibrated with the help of an external reference source.

4.2.1 Method

The amplitude calibration is based on two ingredients: First, in each individual antenna the signal received from a calibrated radio source is measured. Second, the expected signal to be received is calculated using antenna characteristics obtained from calculations. Then, we compare the expected signal strength with the measured signal and derive an amplification factor as the ratio of measured to expected signal, describing how the system alters the incoming signals.

The antenna in an external electromagnetic field extracts a certain amount of power P_r from it, what one can describe with the effective aperture or antenna effective area:

$$P_\mathrm{r} = |\mathbf{S}|\, A_\mathrm{eff} \tag{4.1}$$

The dimension of the effective aperture A_eff is m^2 and the power density is given in $\mathrm{W/m}^2$ giving $[P]$ =W. As a consequence of electromagnetic reciprocity the antenna effective area in receiving direction is related to the antenna gain G in emitting direction like:

$$A_\mathrm{eff} = \frac{G\lambda^2}{4\pi} \tag{4.2}$$

Combining equation 4.1 and equation 4.2 the power that an antenna receives from the power density of an electromagnetic wave $|\mathbf{S}|$ is given by:

$$P_\mathrm{r} = \frac{G\lambda^2}{4\pi}\,|\mathbf{S}| \tag{4.3}$$

Using the relation of the electric field $\mathbf{E}$ and the power density $\mathbf{S}$ from equation 3.3 the received power P_r of an antenna is:

$$P_\mathrm{r} = \frac{G_\mathrm{r}\lambda^2}{4\pi}\frac{|\mathbf{E}|^2}{Z_0} \tag{4.4}$$

The gain G_r of the receiving antenna is the gain that was discussed in section 3.1.2 and for the LOPES antennas it is an input value for the calculation of the power which is received by the LOPES electronics. The power density was expressed with the electric field strength $|\mathbf{E}|$ and this can be a radiation source at a certain distance r. For a transmitter with the power P_t and a gain G_t the resulting electric field strength is given by:

$$P_t G_t = \frac{4\pi}{Z_0} r^2\,|\mathbf{E}| \tag{4.5}$$

Instead of an ambient electric field one can have one transmitting and one receiving antenna, where the power ratio of the receiving to the transmitting antenna is given by the transmission equation from Friis (1946).

$$\frac{P_r}{P_t} = G_r G_t \left(\frac{\lambda}{4\pi r}\right)^2 \tag{4.6}$$

The transmission equation is valid under idealized conditions that are virtually fulfilled in the far-field, for radio frequencies, and not taking into account possible attenuation effects in the atmosphere.

For the calibration we make use of the transmission equation, as we will have on one hand a known radiation source and on the other hand the LOPES antenna, that can be calibrated in this way. All quantities of this equation are known. In addition we will take into account that for linear polarized antennas with a polarization angle β between their axes a loss of power goes with $\cos^2\beta$.

The power P_R that enters in the antenna is not the power that is recorded finally in the system. Instead the power P_M is recorded and this power is related with the calculated input power via a factor V. All components have a frequency dependent characteristics, therefore all calculations are expanded in the frequency ν

Rewriting equation 4.6 with the measured power $P_\mathrm{M}(\nu)$ and the power $P_\mathrm{t}(\nu)$ results in:

$$\frac{P_\mathrm{M}(\nu)}{P_t(\nu)}\cdot = G(\nu)G_t(\nu)\left(\frac{c}{4\pi r\nu}\right)^2 \cos^2\beta \tag{4.7}$$

With $P_\mathrm{R}(\nu)$, that represents the transmitted power of a reference source, the factor $V(\nu)$ is given by:

$$V(\nu) = \frac{P_\mathrm{M}(\nu)}{P_\mathrm{R}(\nu)} = \left(\frac{4\pi r\nu}{c}\right)^2 \frac{P_\mathrm{M}(\nu)}{G_\mathrm{r}(\theta,\phi,\nu)G_\mathrm{t}P_\mathrm{t}(\nu)\cos^2\beta} \tag{4.8}$$

For the amplitude calibration method one has to determine the factor $V(\nu)$. The result of this frequency dependent amplification factor $V(\nu)$ will be used during the analysis of the LOPES air shower data to calculate the absolute electric field strength. The equation 4.8 is expressed with:

P_M The power measured with the LOPES antenna and calculated in the frequency domain.

P_R The (calculated) incoming power to the LOPES electronics chain.

ν Frequency of the emitted signal.

r Distance between the external reference source and the LOPES antenna.

$G(\theta,\phi,\nu)$ Gain of the LOPES antenna taken from model calculations.

$G_\mathrm{t}P_\mathrm{t}(\nu)$ Product of the reference source antenna gain G_t and its power P_t which are not exactly known by themselves, but known as the electric field strength $E_\mathrm{t}(\nu)$ in $r = 10$ m distance. This value is obtained from the manufacture calibration report of our reference source.

β Angle between the polarization axis of the reference source and the field antenna. This axis has to be aligned during the measurements.

4.2.2 Radio Reference Source

The discussed calibration method relies on an external radio source which is calibrated independently. For the actual amplitude calibration method a commercial product from the company Schaffner, Augsburg (Type: VSQ 1000 with DPA 4000 and RSG 1000) was used. More detailed information are available on data sheets at www.teseq.com or reference Hakenjos (2006).

The radio reference source (further referred to as VSQ) consists of a biconical antenna, Schaffner DPA 4000, attached to a signal comb-generator RSG 1000, see fig. 4.3. The signal comb-generator gives a signal peak from 1 MHz to 1 GHz, which can be multiple a of 1 MHz, 5 MHz, or 10 MHz. To achieve a good coverage of the LOPES frequency range the calibration was performed with the smallest frequency spacing of 1 MHz. The signal generator has a mean power of 1 μW over the whole LOPES frequency range (40–80 MHz). Since it is battery-operated, it is usable for measurements on the antenna field. Due to the selected 1 MHz spacing the absolute electric field strength is in general lower. Beside the discrete spectrum the source emits only each 1 μs a defined pulse. The biconical antenna DPA 4000 is linearly polarized and has a nearly constant directivity close to its main lobe. This is important since it results in only a small loss, if the radio source is slightly off target. The DPA 4000 is originally designed for the frequency range 300–1000 MHz, but the VSQ 1000 is specified and certificated for the broader frequency range from 30–1000 MHz despite the fact that the antenna factor changes in the lower frequency range. Nevertheless, it fits within the LOPES frequency range.

The reference radio source itself is calibrated, hence the resulting field strength at any given distance can be calculated. For the fiducial distance of 10 m from the VSQ the electric field strength ranges from 210 $\mu\mathrm{V\,m^{-1}\,MHz^{-1}}$ at 40 MHz up to 2100 $\mu\mathrm{V\,m^{-1}\,MHz^{-1}}$ at 80 MHz. The systematic uncertainty of the calibration measurements for the electric field strength is 2.5 dB (or $\approx$ 33 %). This value is reported in the certificate of calibration provided by the manufacturer for our individual VSQ. Beside this uncertainty of the calibration method the signal stability of the RSG 1000 for the temperature range 10°C –30°C is $<$ 0.5 dB (or $<$ 6 %). The data sheet provides the electric field strength in the logarithmic unit dBμV/m that are converted like:

$$\log_{10} E[\mu\mathrm{V\,m^{-1}}] = \mathrm{E}[\mathrm{dB}\mu\mathrm{V\,m^{-1}}]/20 \tag{4.9}$$

This includes the free space impedance $Z_0 \approx 377\Omega$ and for the analysis the electric field strength is converted into a power:

$$P = \frac{4\pi}{Z_0} r^2 \cdot (E[\mu\mathrm{V\,m^{-1}}])^2 \tag{4.10}$$

4.2.3 Measurements at the Antenna Field

For a calibration campaign, the whole setup of the VSQ is placed at about 10.5 m above each LOPES field antenna, using a movable crane with a wooden extension (see figure 4.4). Fixed in a frame, the whole setup consists of the reference source VSQ, an external GPS antenna, and the GPS hand-held unit. The wooden extension is necessary to avoid reflections of the radio signal of metal parts of the crane, which would otherwise lead to differences between calculated and real received power. For

Figure 4.3: The VSQ 1000 from Schaffner consists of the signal generator RSG 1000 and the biconical antenna DPA 4000. The total length of the biconical antenna is 40.5 cm (image courtesy of Schaffner).

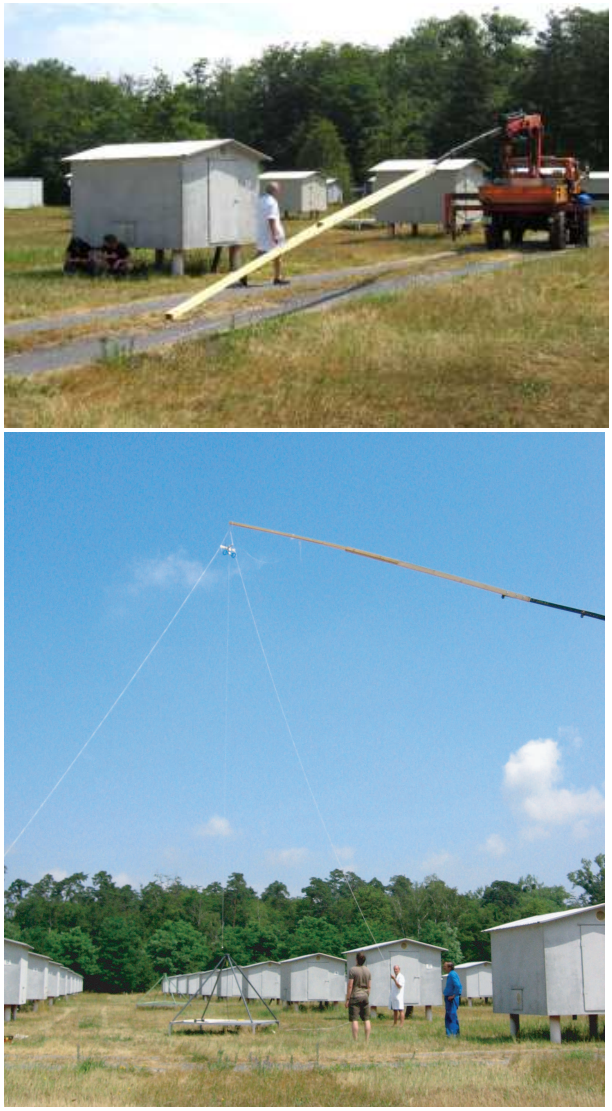

Figure 4.4: Calibration campaign at the LOPES field. Top: Preparation of the setup, like mounting the wooden beam. Bottom: Configuration during the actual measurement.

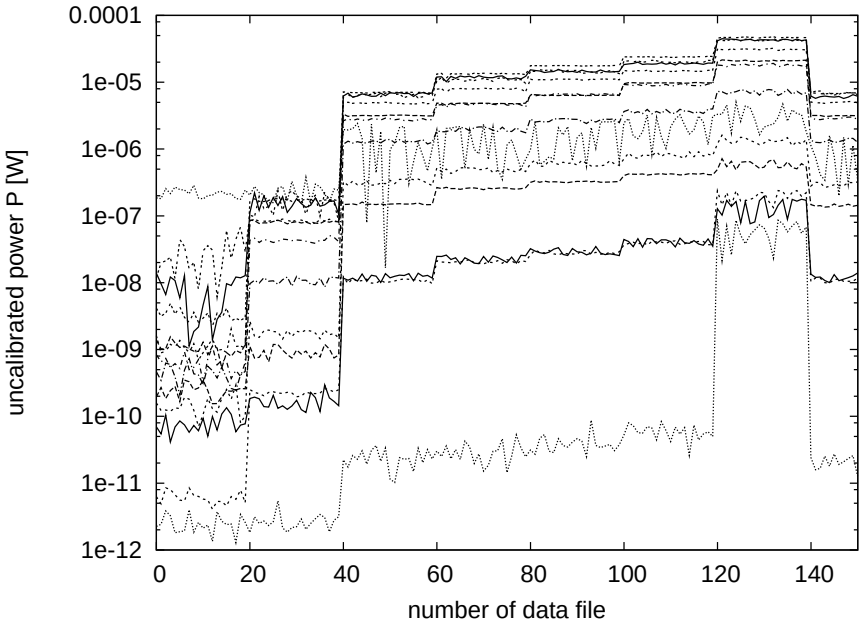

Figure 4.5: During a calibration campaign the data files are stored each 6 seconds and afterwards the received power is read-out. For antenna #20 the uncalibrated power is shown for the first 7 measurements with 20 data files each. Different line types indicate different frequencies.

the VSQ setup we use a plummet with a fixed length and a differential GPS to determine the exact position of the radio source. The used differential GPS is a ProMark2 system from Ashtech Solutions that achieves a precision in the position of about 10 cm. The accuracy of the measurement is varying with the number of satellites that are used for the determination.

The calibrated external radio source is emitting at a distance of about 10.5 m and the received signal in the field antenna is transmitted to the electronics chain via a long coaxial cable. During each calibration run, artificially triggered data files are stored. Each file contains N=65536 samples per antenna, at a sampling rate of 12.5 ns this results in 819.2 μs of data. The calibration setup lasts for at least two minutes at a field antenna and uses a trigger period of 6 seconds (rate 0.17 Hz), which leads to 20 or more stored data files. As the signal comb-generator gives a discretized time signal with 1 μs spacing either 818 or 819 pulses per data file are recorded. Summing up over the 2 minutes, a difference for the received power can be about $(818 - 819)/819 \approx 0.1$ %. A possible systematic uncertainty from this is very low and is not further considered. The way of data taking is used to average over small geometric variations in the setup during the calibration procedure. On the other hand, influences from wind gusts and fast changes in environmental conditions can be monitored and affected data files are not considered for the next analysis steps.

Each data file is analyzed individually in our software package and after a Fourier transformation the complex values are used to calculate the amplitude for a certain frequency. The resolution in the frequency domain from 40–80 MHz is determined by the Fourier transformation to $N/2 = 65536/2 = 32768$ bins to 40 MHz/32768 = 1.22 kHz.

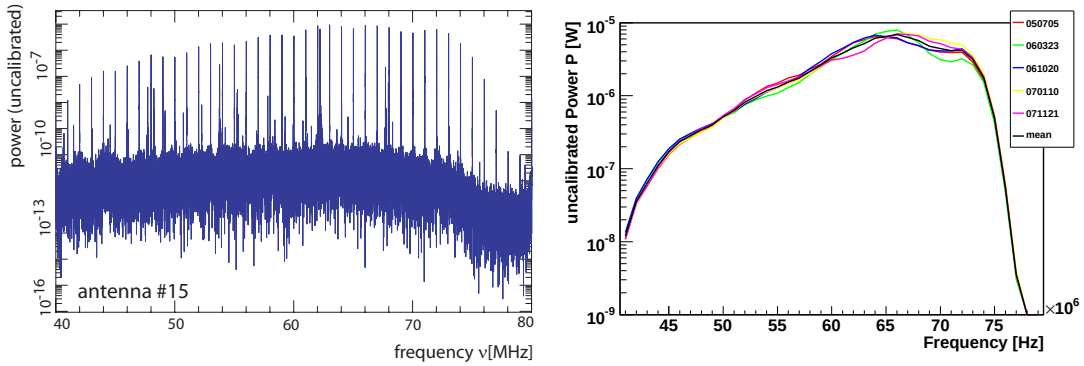

(a) Measured power of one calibration raw data file. Clearly visible are the 1 MHz steps of the emission of the reference antenna with is comb generator.

(b) Measured power of antenna #15 for different campaigns over more than two years, showing sufficient stability

Figure 4.6: The uncalibrated power for antenna #15 is shown for a single data file (left) and all measurements taken during calibration campaigns (right).

The characteristic of our radio reference source with the comb-shaped spectrum with 1 MHz spacing is shown in figure 4.7(a). The amplitude in the frequency domain is equivalent to the received power, binned with N/2=32768 bins. The measured power $P_{\mathrm{M}}(\nu)$ for each integer frequency is determined by summing over 20 bins or 24.4 kHz around the center of the peak. The peak value is on average three orders of magnitude higher than the surrounding noise level and has spreads over roughly 5–10 bins, i.e. 6–12 kHz. The noise floor around the frequency peak contributes with less than 1 % to the integrated power.

In figure 4.5 the uncalibrated measured power for a fixed antenna during a calibration campaign is shown. Easy to recognize is the change after 20 data files and the increase of the power, as for this measurement the distance between reference source and antenna was varied. The first measurements for this day give a stepped structure each 2 data files wide. The radio source was not in the vicinity of the antenna #20 during the first 20 data files, thereby showing the noise background only for each frequency.

The different lines are for different frequencies and some of them are very noisy or with low power (e.g. 41 MHz at the band-pass filter edge). At some fixed frequencies, not every time, and not in all antennas, man-made RFI in the same order of magnitude as the received signals strongly affects the measurement. Therefore a linear interpolation of the received power replaces these contaminated frequencies. In figure 4.5 the upper noisy line is for 50 MHz, which signal will be replaced by a linearly interpolated using the values from 49 and 51 MHz.

The integrated power P_{M} for each integer frequency averaged over all data files in a calibration step (at least 20 in 2 minutes) reflects the overall behavior of the LOPES antenna system during such a measurement. For each antenna a set of measurements $P_{\mathrm{M}}(\nu)$ exists, which is used to calculate the ratio $V(\nu)$ of measured to expected power.

For that purpose one has to be sure that one operates in the far field region, not to be disturbed by near field effects of the emitter. The far field approximation ($r_{\mathrm{far}} > 2\,D^2\,\nu/c$) should be valid for $r_{\mathrm{far}} > 2$ m at $\nu = 80$ MHz and with an antenna

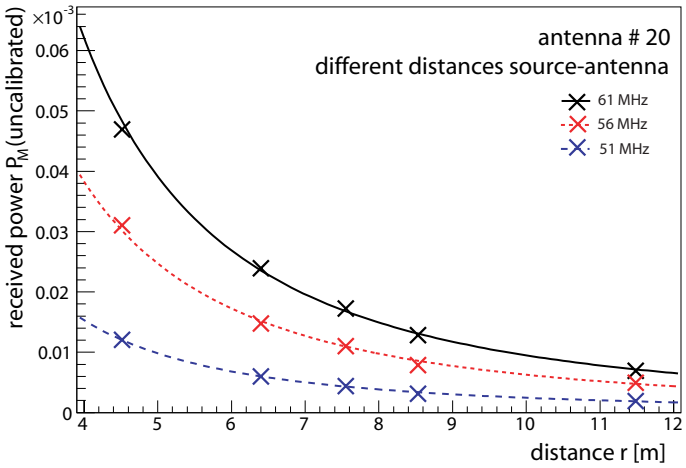

Figure 4.7: The data points show the received power P_{M} integrated over 61 kHz for various frequencies as a function of r, which is the distance source - LOPES antenna. The lines are fits of a r^{-2} dependence.

aperture $D = 1.8$. In the far field approximation the energy density of the electromagnetic field varies as r^{-2} with the distance r. Figure 4.7 shows measurements of the received power P_{M} with respect to the distance r between the reference source and the LOPES antenna. The power P_{M} is the integrated power over 61 kHz around the mean frequency. For distances of $r = 4.5$ m to $r = 11.5$ m the far field approximation was tested. As the fits for the different frequencies (51, 56, and 61 MHz) are performed with a fixed power index of -2, $P_{\mathrm{M}} = a \cdot r^{-2}$, the measurement clearly shows the validation of the far field approximation. This measurement has also shown that a possible saturation effect for the low-noise amplifier is unlikely, and that the calibration acts in the linear working regime. The 12-bit ADC also does not suffer from a saturation effect, but the closest measurement at 4 m distance was at the limit of analogue input voltages (± 1 V) for the ADC. For the calibration campaigns a distance r between field antenna and reference source of around 10 m was chosen, therefore, we can exclude saturation effects for the determination of the amplification factors.

4.2.4 Amplification Factors

From the measurements taken over more than two years all antennas could be checked multiple times, particularly important after changes in the hardware or after maintenance work. The amplification factors V calculated with equation 4.8 describe the system influence, exemplarily shown for one antenna in figure 4.8, based on the result shown in figure 4.7(b).

The amplification factors $V(\nu)$ for all 30 LOPES antennas are shown in figure 4.9. The curves for each antenna represent the mean values of measurements performed over two years. The frequency range of the ADC is between 40 and 80 MHz, however, also the filter characteristics at the upper and lower bound can be seen, which gives an effective range of approx. 44 MHz to approx. 75 MHz. The difference in the shape of the individual antenna amplification curves is a result of different types of filters and batches of electronic components installed for the first 10 antennas compared to the later installed antenna setups. At the actual configuration of LOPES the

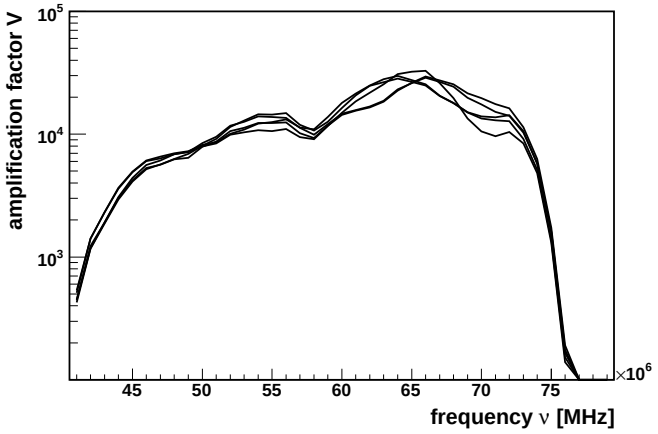

Figure 4.8: All measured amplification factors of antennas 15 show a reasonable stability during the operation of the LOPES experiment.

cable length is either 100 m or 180 m, which might also lead to differences in the amplification factors for different antennas. The loss difference for the 180 m to 100 m cable is $9.4 - 5.2 = 4.2$ dB or about a factor of three. It was found that the total scatter of one order of magnitude between the amplification factors (figure 4.9) does not simply relate to the cable length. Instead, the scatter originates roughly to equal parts from the adjustments of the operating points of the electronic modules, peculiarities for certain antenna field positions, and the different cable lengths.

A common feature of all curves in figure 4.9 and figure 4.8 is a dip at 58 MHz. This feature relates to the antenna gain simulation and is described in more detail in section 3.1.2.

The large overall scatter between the individual antennas of roughly one order of magnitude obviously necessitates the complete amplitude calibration. In the analysis of the shower data we use the amplification factors to correct the raw data in order to get calibrated power values. Moreover, related systematic effects in the determination of these amplification factors $V(\nu)$ have been investigated, which will be described in the following sections.

To implement the obtained amplification factors in the analysis pipeline the relation of the measured quantity voltage U_{ADC} at the A/D-converter to the electric field strength $|\mathbf{E}|$ has to be investigated. The software used for the analysis is based on the AIPS++ - Astronomical Information Processing System (AIPS++ consortium 2006). Calibration tables with system specific informations are generated to manage the antenna selection. The digitized voltage of the ADC results in ADC-counts:

$$P_{\mathrm{ADC}} = \frac{U_{\mathrm{ADC}}^2}{R_{\mathrm{ADC}}} = \frac{\left(\mathrm{ADC-counts}\frac{\text{max. Voltage}}{\text{max. Counts}}\right)^2}{R_{\mathrm{ADC}}} \tag{4.11}$$

The input impedance R of the ADC is 50 Ω. From equation 4.4 one gets the relation of the electric field strength and the received power P_{r}. For a bandwidth $\Delta\nu$ one can write:

$$\frac{|\mathbf{E}|^2}{(\Delta\nu)^2} = \frac{1}{(\Delta\nu)^2} \cdot \frac{4\pi}{G_r\lambda^2} Z_0 P_{\mathrm{r}} \tag{4.12}$$

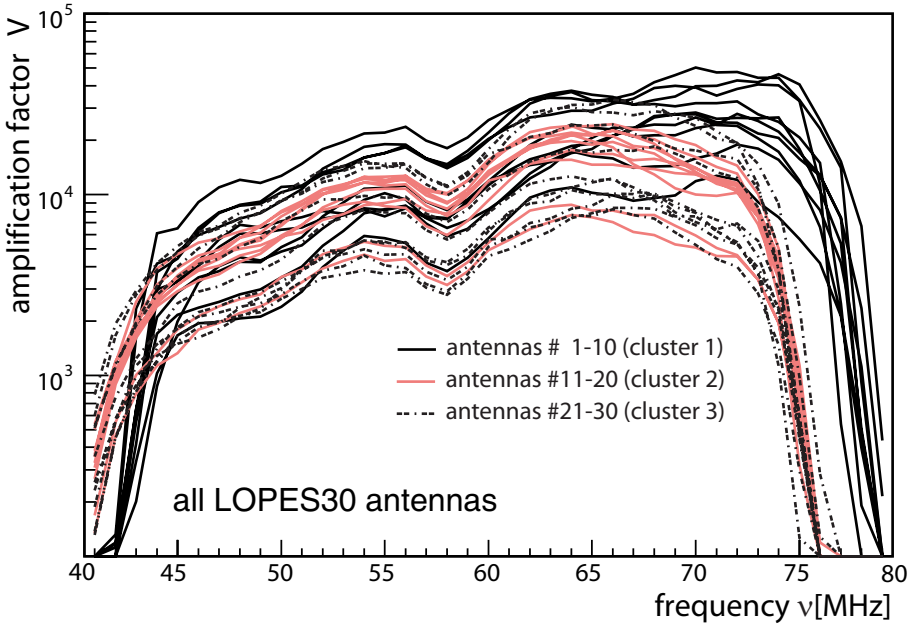

Figure 4.9: Amplification factors of all LOPES antennas. The different colors and line types are used to separate the three antenna clusters. Each cluster combines ten antennas with their individual electronics.

Now, together with equation 4.11 and the fact that the power at the ADC is $P_{\mathrm{ADC}} = V(\nu)P_{\mathrm{r}}$, including the amplification factor from section 4.2.1 one gets:

$$\frac{|\mathbf{E}|^2}{(\Delta\nu)^2} = \frac{1}{(\Delta\nu)^2} \cdot \frac{4\pi\nu^2\mu_0}{G_r c} \frac{U_{\mathrm{ADC}}^2}{R_{\mathrm{ADC}}} \cdot V(\nu) \tag{4.13}$$

The implementation of the calibration tables in the software finally enables the calculation of the field strength per unit bandwidth from the measured ADC values:

$$\epsilon_\nu = \frac{|\mathbf{E}|}{(\Delta\nu)} = \sqrt{\frac{4\pi\nu^2\mu_0}{cR_{\mathrm{ADC}}}} \cdot \sqrt{\frac{V(\nu)}{G_r(\nu,\theta,\phi)}} \cdot U_{\mathrm{ADC}} \tag{4.14}$$

The constant part in equation 4.14 can be summarized in a term with the dimension [m] as it is needed for the conversion of measured voltage [V] to an electric field strength [$\mathrm{V\,m^{-1}}$]. The amplification factor $V(\nu)$ and the model calculation of the antenna gain $G_{\mathrm{r}}(\nu,\theta,\phi)$ are needed input values available via calibration tables in AIPS++.

4.2.4.1 Stability

An important issue of the calibration procedure is its stability over repeated measurements. Besides uncertainties in the position or the alignment of the reference source with the field antenna or by small changes in handling the experimental calibration procedure (see section 4.2.4.3), there could be large differences between the measurements of an antenna due to changing environmental conditions like precipitation, ground humidity, air temperature, vegetation growth etc. If such differences exist to a greater extent, this would cause problems in the applicability of the amplification factors. To verify the influence of such changing environmental conditions

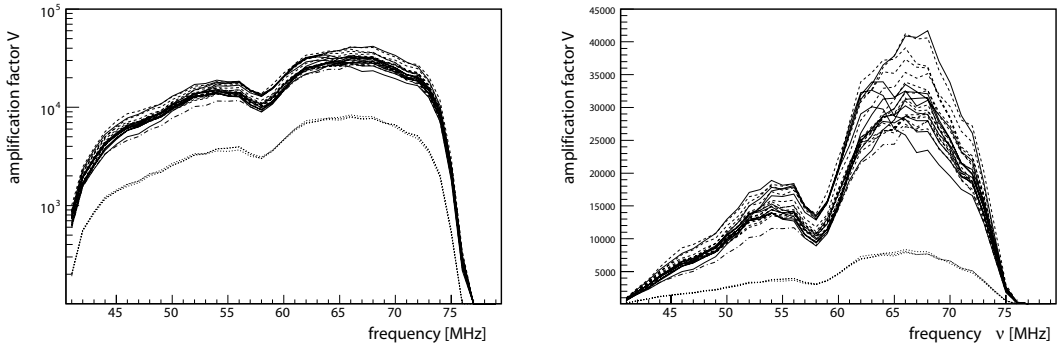

Figure 4.10: Amplification factor of one LOPES antenna from independent measurements. These measurements were spread over the course of more than two years and include 21 calibration campaigns. Left: logarithmic y-axis. Right: linear y-axis.

we performed a series of measurements over more than two years of LOPES operation. In these campaigns one field antenna (antenna #21) was measured each time and therefore under different environmental conditions. The resulting amplification factors for this antenna are displayed in figure 4.10. All amplification factors are given in the appendix A. The two lower lines in figure 4.10 result from a partial damage of the amplifier after some maintenence. The measurements include weather conditions occurring during the year in Karlsruhe, except extremes like snow and thunderstorm. The temperature ranges from around ~ -5 °C up to ~ 35 °C, the soil change from dry in the surface layer (0–60 cm) to a high ground humidity after days of rain, and the ground vegetation varies from recently mowed to a flowery meadow. The variation found is a measure of the systematic uncertainties of the calibration procedure or, on the other hand, reflects the accuracy of this calibration method. In the effective frequency range of the LOPES band pass filter from 44 to 75 MHz an average scatter of about 13 % was found.

It is obvious that the variation from antenna to antenna (fig. 4.9) is much larger than the variation due to changing environmental conditions or conditions of the calibration procedure (note the logarithmic scale in fig. 4.9 compared to the linear scale in fig. 4.10, right). There are many possible sources for the systematic uncertainties and a significant reduction of the observed variation requires deeper investigations. One possible source of the variations is thought to be the LNA temperature. But the temperature of the low noise amplifier at the antenna is not directly available. Also the end part of the long coaxial cable is situated outside, but the remaining part of the cable and the LOPES electronics is either underground or inside an air-conditioned housing. However, variations with the air temperature can be used as a first order approximation.

We use the air temperature at two meters height above ground, which is provided by the KASCADE experiment. With 24 hours continuous monitoring using the VSQ at a fixed position in a distance of 16.5 m and with a zenith angle of 87°, we covered an air temperature range of 3 °C – 26 °C. The measurements have been performed at one day in March (3 °C – 16.5 °C) and one day in April (8 °C – 26 °C). The data taking is similar to the calibration campaigns, except that here the KASCADE trigger is used, giving an average rate of 0.04 Hz. For each ten minutes an averaged amplification factor $V(\nu)$ is calculated. The figure 4.12(a) displays the

average amplification factor $V(73\ \mathrm{MHz})$ (squares, left y-axis) and the air temperature in degrees at 2 m height (circles, right y-axis) over time. To show the relative change of the average amplification factor, the highest value at the day was used for normalization. The daily temperature modulation is well pronounced and shows a minimum in the early morning. The highest temperature was recorded in the early afternoon. As the performance of electronic devices changes with temperature, the LNA circuit connected directly to the antenna at the field has a better performance at low temperature values.

From the figure 4.12(b) one derives that in general the amplification factor decreases to lower values with increasing air temperature. The maximum drop add up to around 15% for the amplification factor at this day and is obtained at 12 pm. For the covered air temperature range one can derive that ten degree difference in temperature causes a change of about 10 % in the amplification factor. This implies that a first order correction of this effect is possible using the air temperature. The uncertainty in temperature stability of about 6 % of the reference signal generator is not corrected for. This value is considered for the temperature range 10 °C – 30 °C. The change in temperature is somewhat higher than this methodical uncertainty, but can not be disentangled. Nevertheless, the LNA temperature should be measured directly to fully verify the temperature dependence of the LOPES system. The top of the antenna with its round socket is waterproof and directly exposed to the sun, therefore the temperature for the LNA is most probably even higher than the air temperature itself. This implies that the observed change of the amplification factor is for a larger difference in temperature and this might decrease the dependence with the air temperature. Furthermore this can explain why there is a loop like structure visible in figure 4.12(b) and the curve does not return to its initial value.

4.2.4.2 Polarization

Since end of 2006 LOPES is operating some antennas in a dual-polarized configuration. In particular, for such a configuration a cross-check of the polarization sensitivity has to be performed during the calibration campaigns. Figure 4.13(a) shows the relative amplification factors for the east-west oriented antenna #5 measured in one campaign where the azimuth angle ϕ was varied in steps of 10 degrees by rotating the VSQ reference source above the field antenna ($\phi_{\mathrm{Ant}} = 90°$, equal to east-west orientation). The amplification factor V at $\phi = 90°$ was used for normalization. From formula 4.8 we know that the received power changes with $\cos^2\beta$, with respect to the linear polarized LOPES antenna. The angle β is defined as the angle between the axes of VSQ and field antenna. The azimuth angle ϕ is related with the angle β by $\phi = \beta - \phi_{\mathrm{Ant}}$.

The results obtained prove the expected $\cos^2\beta$ polarization sensitivity of the LOPES antenna, in figure 4.13(a) exemplarily shown for 63 MHz.

$$V(\phi) = a \cdot \cos^2(\beta + \alpha) \tag{4.15}$$

$$= a \cdot \cos^2(\phi + \alpha + \phi_{\mathrm{Ant}}) \tag{4.16}$$

The fitted function uses two free parameters to describe the measurements: $a = 0.98 \pm 0.01$ as scaling parameter and $\alpha = -3.0° \pm 0.6°$ as angle offset. The theoretical expectation is based on $V(\phi) = cos^2(\phi + \phi_{\mathrm{Ant}})$ with no free parameters. Both curves are very close to each other and show the achieved accuracy for aligning the

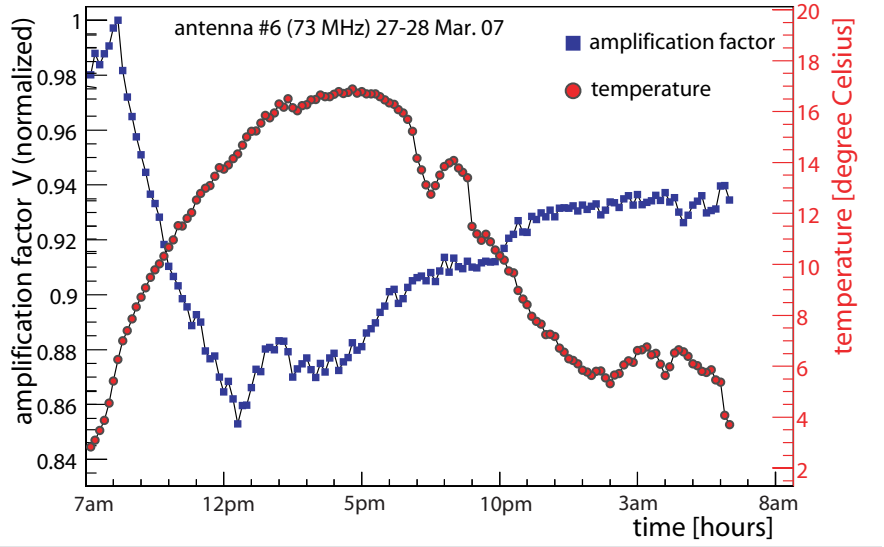

(a) Relation of amplification factor $V(73\ \text{MHz})$, normalized to the highest values, over time and the diurnal cycles of the air temperature at 2 m height over time.

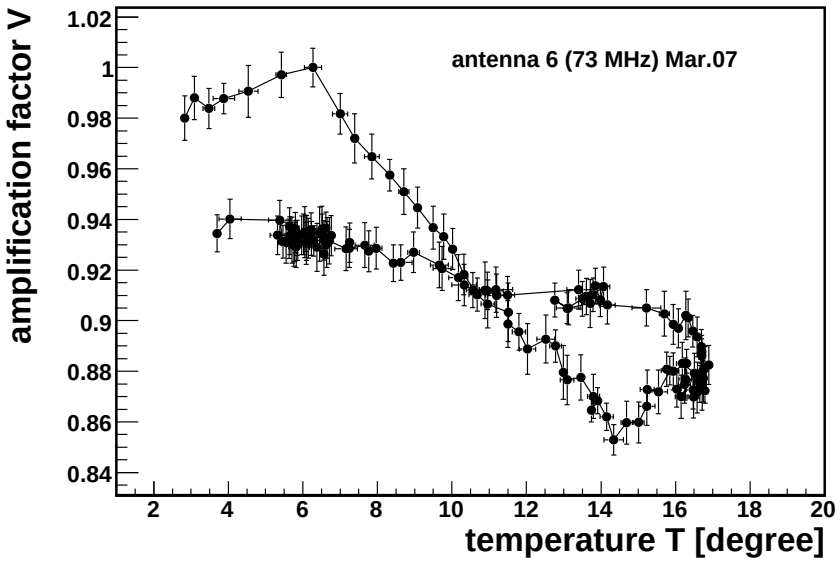

(b) The normalized amplification V for antenna #6 measured at different air temperatures in 24 hours. An increasing air temperature leads to a decreasing amplification factor. The change is about 10 % for about 10 degree change in temperature.

Figure 4.11: Amplification factor of antenna #6 at 73 MHz (left y-axis) and temperature 2 m above ground (right y-axis) plotted against time and each point represents all recorded events within ten minutes. The antenna was monitored over a period of 24 hours with fixed setup started at 7 am and the highest value was used to normalize the amplification factor V. The maximum drop for V is obtained at 12 pm and add up to around 15%.

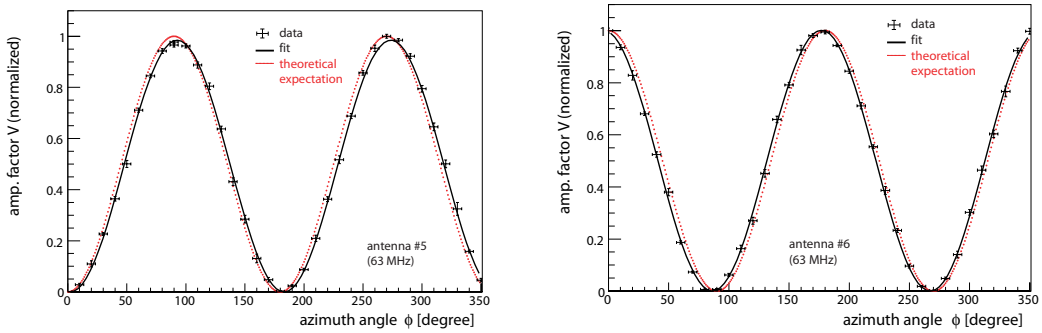

(a) Polarization measurements at 63 MHz for antenna #5, amplification factor normalized to the maximum at $\phi = 270°$

(b) Polarization measurements at 63 MHz for antenna #6, amplification factor normalized to the maximum at $\phi = 0°$

Figure 4.12: Relative amplification factors V at 63 MHz for the dual-polarized antenna #5, but with varying the azimuth angle ϕ and normalized to the amplification factor at $\phi = 270°$. The position of the source was vertical above the LOPES antenna. The fit function is: $V(\phi) = a \cdot \cos^2(\phi + \alpha - \phi_{\mathrm{Ant}})$ and indicated by a black line, whereas the theoretical expectation $V(\phi) = \cos^2(\phi - \phi_{\mathrm{Ant}})$ is drawn by a red dashed line, both are normalized.

polarization axes from VSQ and field antenna. With a systematic offset of $\alpha = -3.0°$ for this measurement we derive a systematic uncertainty of $\sigma_\beta = 7°$. However, in the case of strong disturbing wind the alignment might be worse and can result in a higher loss in the received power.

Figure 4.13(b) shows results of the same measurements at the same antenna station, but the data are analyzed for the north-south oriented antenna #6, i.e. $\phi_{\mathrm{Ant}} = 0°$. Together with figure 4.13(a) the two plots show the capability and applicability of calibration and event data taking with LOPES in a dual-polarized antenna mode.

The measured power ratio of antenna #6 to antenna #5 is less then 2 % for the relevant frequency range. The figure 4.13 shows this exemplarily for 63 MHz, as a function of the azimuth angle ϕ. With $V_{\mathrm{Ant5}} \propto \cos^2\phi$ and $V_{\mathrm{Ant6}} \propto \cos^2(\phi + 90°)$ the power ratio is a $\cos^2\phi/\sin^2\phi$-function, that was fit in figure 4.13, red line. The parameter A_0 represents the absolute power ratio of antenna #5 and #6, b the deviation from a 2π-period, and ϕ_d the angular offset.

Despite this independent calibration there remains the possibility of cross talk between both channels as their low noise amplifiers are mounted in the same box.

4.2.4.3 Uncertainties

In previous sections systematic effects of the calibration source, the temperature dependence, and the polarization sensitivity were described. In this section we will discuss in detail the different sources of uncertainties and summarize them. The statistical uncertainty of the calibration procedure for the amplification factors $V(\nu)$ in the effective frequency range 44–75 MHz are in most cases negligible ($\mathrm{stat}_{\mathrm{calib}} =$ 1.5 %) due to the 20 'trigger'-measurements per individual calibration configuration.

The total systematic uncertainty for one calibration campaign is estimated by a combination of the individual sources. These sources are identified and the resulting standard deviations estimated for:

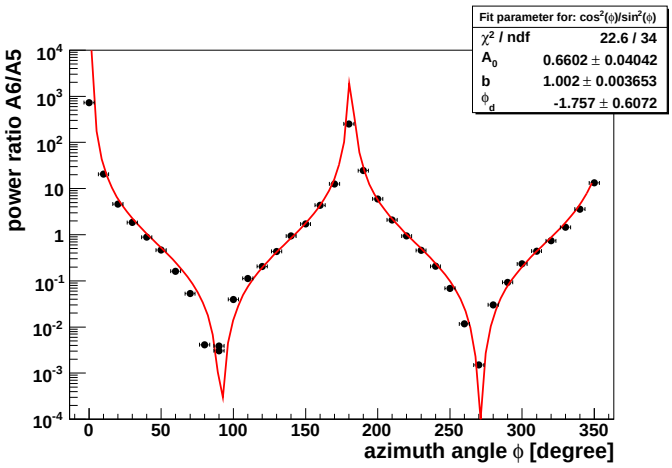

Figure 4.13: To cross check the separation of the two polarizations of antenna #5/#6 the ratio of the measured power is shown against the azimuth angle ϕ. Exemplarily this plot is made at a frequency $\nu = 63$ MHz. The amplified fit function is $cos^2\phi/sin^2\phi$. A power ratio in the turning points larger 10^2 or smaller 10^{-2} indicates the reasonable channel separation.

r: The uncertainty in estimating the distance between reference source and antenna is estimated to $\sigma_r = 0.25$ m.

ν: The deviation in frequency is given by the resolution of the power spectrum after fast Fourier transformation and results to $\sigma_\nu = 600$ Hz, originating from the 1.22 kHz resolution of the FFT data.

G_tP_t: The information from the data sheet of the reference antenna allows only to estimate the uncertainty of the product of gain and power. There is a variation of the output power with changing temperature in the order of $\sigma_{G_tP_t}/G_tP_t = 12\%$. This does not include the systematic uncertainty for the calibration of the reference source itself, which is 2.5 dB for the electric field, respectively $\mathrm{sys}_{\mathrm{reference}} \approx 67$ % for the emitted power.

G_r: The simulated antenna gain. This is second largest source of uncertainty and the largest for the calibration procedure itself and is estimated to be $\sigma_{G_r}/G_r \approx 15$ %, but can be even larger at the expected resonant frequency; see next section.

P_M: The uncertainty of the measured power is given by the data acquisition system and read-out process of the power values and estimated to $\sigma_{P_M}/P_M \approx 5$ %.

β: The uncertainty for the angle between the polarization axis of the reference source and the axis of the LOPES field antenna is estimated to $\sigma_\beta = 7°$, which results in a maximum loss of 2 % for the emitted power.

Environmental effects: Due to the fact that the LOPES antenna uses the ground as a reflector, humidity at the ground can influence the values, despite the metal reflector below the antennas. An estimation of this uncertainty is derived from measurement campaigns over two years (figure 4.10) and results to $\approx$ 13 %. In this uncertainty, effects from the antenna coupling, varying

ground conditions, and a temperature change of the signal generator output are included.

Using Gauss' error propagation law for a function $f(x_1, x_2, ..., x_k)$ the uncertainty $\tilde{\sigma}_f$ is given with:

$$\tilde{\sigma}_f^2 = \sum_{j=1}^{k} \left(\frac{\partial f}{\partial x_j} \right)^2 \tilde{\sigma}_{\bar{x}_j}^2 \tag{4.17}$$

The independent variables $x_1, x_2, ..., x_k$ with their uncertainties $\tilde{\sigma}_{\bar{x}_1}, \tilde{\sigma}_{\bar{x}_2}, ..., \tilde{\sigma}_{\bar{x}_k}$ have been estimated in the previous list. From these systematic uncertainties an overall uncertainty for the amplitude calibration of the LOPES antenna array can be calculated to $\sigma_V/V = 0.70$. This includes the statistical uncertainty $\mathrm{stat}_{\mathrm{calib}}$ and all other uncertainties described above. As these uncertainties are of different kind a separation in three main groups can be done:

$$\begin{aligned} \left(\frac{\sigma_V}{V}\right)^2 &= (\mathrm{stat}_{\mathrm{calib}})^2 + (\mathrm{sys}_{\mathrm{calib}})^2 + (\mathrm{sys}_{\mathrm{reference}})^2 \\ &= (0.015)^2 + (0.205)^2 + (0.67)^2 \end{aligned} \tag{4.18}$$

Ignoring the calibration uncertainty given by the commercial radio source with $\mathrm{sys}_{\mathrm{reference}} = 67\%$ the listed systematic uncertainties sum up to $\mathrm{sys}_{\mathrm{calib}} = 0.205$. Here, the antenna simulation and the environmental effects give the largest contributions. By more detailed studies of the antenna directivity the uncertainty $\mathrm{sys}_{\mathrm{calib}}$ might be decreased (section 3.1.2).

As the weather and environmental effects are difficult to quantify, a correction of a correlation of the system performance with the temperature (as described in section 4.2.4.1) is not yet performed for the amplification factors. On the other hand it will improve the uncertainty for the environmental effects only, which contributes only with ≈ 13 %.

The dominating factor for the total uncertainty is given by the calibration accuracy of the VSQ1000 radio source, provided by the manufacturer. Using another reference source would lead to a different, maybe smaller, total systematic uncertainty.

4.2.5 Directivity

The described calibration procedure also allows us to check at least partly the calculation results of the antenna gain pattern (section 3.1.2). There are three possibilities for this value. We can use the calculations with pedestal or without pedestal, or one just fixes the value to a number, e.g. 4 (gain [dB] at 60 MHz and zenith angle $\theta = 25°$–$30\ °$, azimuth $\phi = 0$). The last value would give the isotropic radiator. That is of course never the case, but one should see how much the antenna really receives.

By moving the source away from the zenith, but tilting the source accordingly to keep the emission and the polarization angles constant, one is able to check the zenithal dependence of the antenna gain. For higher inclinations the amplification factors, i.e. the sensitivity of the antenna, decreases. Figure 4.14 shows the amplification factors for one dual polarized antenna measured at one campaign but the source located at different zenith angles ($\theta \neq 0$).

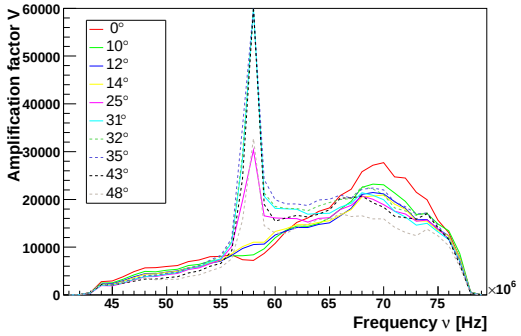

(a) Pattern test at antenna #5 - E-plane including the pedestal

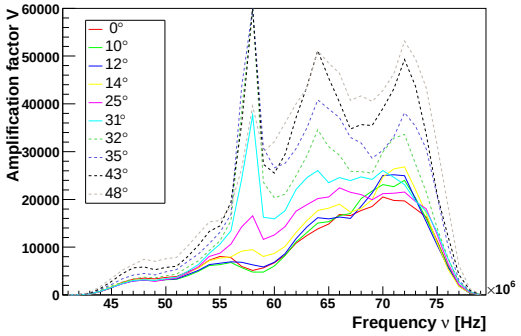

(b) Pattern test at antenna #6 - H-plane including the pedestal

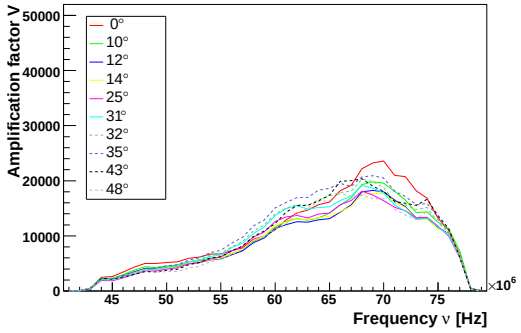

(c) Pattern test at antenna #5 - E-plane without a pedestal below the antenna

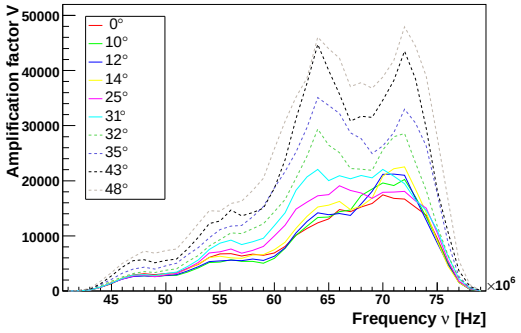

(d) Pattern test at antenna #6 - H-plane without a pedestal below the antenna

Figure 4.14: Comparison of amplification factors for two antennas, equipped as dual polarized antenna, amplification factors for different zenith angles are shown. The calculations include the pedestal (upper row) or use an antenna placed at the ground (lower row). The E-plane (left column) and the H-plane (right column) could be tested with this measurement for different zenith angles up to 48°.

The most eye catching feature in figure 4.14 is the sharp resonance at 58 MHz for zenith angles larger than $\approx 20°$ (figure 4.14(a,b)). This feature is not visible if one uses the gain calculation with no pedestal for the LOPES antenna (figure 4.14(c,d)). Therefore the peak is an artificial feature of the calculation. As an independent test the "isotopic radiator" using a fixed gain also does not shows such a prominent resonance, figure 4.15. If the resonance effect would be present as predicted, a clear peak for vertical positions and a large dip for $\theta = 45°$ should be visible at 58 MHz. As this is not the case we conclude that either the calibration procedure smears out all the effects, which is implausible with the obtained total systematic uncertainty of the calibration, or the antenna gain simulation overestimates the effect of the ground plate.

The prediction of a pronounced resonance at 58 MHz caused a dip, visible in figure 4.9 and 4.10. This feature is no longer visible if one uses the calculation with no pedestal for the LOPES antenna, figure 4.15(c) Beside the 58 MHz there are two more peaks at 64 and 72 MHz in the H-plane, which do not appear in the E-plane. Remarkably they do not disappear even for the "isotropic radiator" (figure 4.16(b)). One has to assume that this is a general feature of an inverted-V dipole and is not

related with the pedestal. However, they are not yet considered correctly by the gain calculation.

In the calculation of the amplification factor V (see equation 4.8) an antenna pattern G_r is included. As an expectation a correct antenna gain calculation should result in overlying curves (figure 4.14), of course only within the uncertainty for the calibration method. For at least zenith angles below 20 degree this seems to be the case (figure 4.15(a)). It also seems that for low frequencies (45-55 MHz) the curves are closer, compared to higher frequencies (65-75 MHz). This is confirmed by measurements at several antennas, even if the precision for determining the zenith angle was less good. This so far is the case for the E-plane. For the H-plane the picture seems to look differently (figure 4.15(b)), but the 58 MHz features behave the same. For higher inclinations the simulation predicts a too low gain, resulting in a large amplification factor, $V \propto 1/G$. Here also the low frequency part is less scattered than at higher frequencies. Talking in terms of wavelengths the short wavelengths are not so well described, at least for small zenith angles. For higher zenith angles the curves start to diverge from each other. This is also the case for the non-pedestal calculations, see figure 4.15(d), and looks even worse for the simulation with pedestal, figure 4.15(b). There could be an influence of the definition of the ground characteristics. The resistance, ground humidity, and conductivity will play a more important role for high zenith angles and they were fixed for the antenna gain calculations, but do not need to match to real conditions at the LOPES antenna field.

A comparison of all three gain cases shows that the LOPES antenna is nearly a isotropic radiator for small zenith angles. In all three cases the amplification curves are close to each other, within the measurement uncertainty, for the E-plane as well as for the H-plane. This can be derived from the the fix gain analysis (figures 4.15) and holds for both gain cases, figure 4.15(a) and 4.15(c).

Furthermore there is an interesting effect about the absolute value of the amplification factors for the three cases. For the tested E-plane (figure 4.15(a) and 4.15(c)) the amplification factor at, e.g. 65 MHz, changes from $\approx$ 15100 non-pedestal gain to $\approx$ 17200 pedestal gain, giving a difference of 2300 or $\approx$ 15 % in the zenith, or from $\approx$ 14600 non-pedestal gain to $\approx$ 17000 pedestal gain, giving a difference of $\approx$ 2400 or $\approx$ 16 % at a zenith angle of 14°. This does not change very much for lower frequencies at around 48 MHz ($\approx$ 4500 to $\approx$ 5100 = 13 %, at a zenith angle of 14°). From comparison with the fix gain analysis (figure 4.16(a)) there is only a small difference to the non-pedestal calculation of about 3-4 % (14100 fix to 14600 non-pedestal = 500 or $\approx$ 3 %, at a zenith angle of 14°). This can probably be interpreted as the influence of the antenna height from the surrounding ground. At least for low zenith angles this is also valid for the H-plane. The difference between pedestal and non-pedestal is $\approx$ 12 %, but only $\approx$ 4 % from fix to non-pedestal. The question is now what represents better the LOPES antenna gain, the higher values for the pedestal or the lower for the non-pedestal calculation? This question is of importance for the correct calculation of the electric field strengths measured by LOPES, but need a re-analysis of the antenna gain. Anyhow there is a systematic uncertainty assumed for the gain calculation of about 15%, see section 4.2.4.3, which cover this, but can be improved by more detailed investigations.

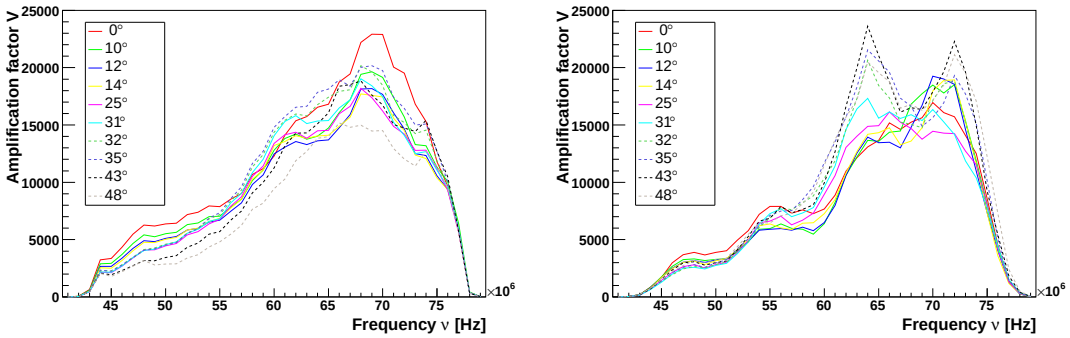

(a) Pattern test at antenna #5 - E-plane using a fix antenna gain of 4.

(b) Pattern test at antenna #6 - H-plane using a fix antenna gain of 4

Figure 4.15: Amplification factors obtained using a fixed antenna gain. Left: antenna #5 sensitive to the E-plane. Right: antenna #6 sensitive to the H-plane.

Another aspect of the pattern test comes from the comparison of the fixed gain to the simulation at high inclinations. Choosing for $G_{\mathrm{r}}(\theta, \phi, \nu) = 4.0$ the antenna pattern corresponds with an isotropic radiator. If one assumes that the calibration method does not have hidden systematic uncertainties for the measurement at higher inclinations, one should see a change in the amplification factor as the antenna should measure less power P_{M} ($V \propto P_{\mathrm{M}}$). Only if one considers an increasing additional contribution from reflected signals to the measured power one can understand the increasing amplification factor for the fixed gain plots in the H-plane, figure 4.16(b).

In general, the very inclined measurements for the E-plan were difficult to perform. The crucial point for the measurement is to get the main radiation direction of the radio reference source aligned with the antenna position that has to be calibrated. The 43 and 48 degree lines indicate this alignment problem as they shown lower amplification factors (figure 4.16(a)).

From the analysis of the measurements one further derives the increasing influence of the gain calculation at high inclinations. The simulation strongly enhances the amplification factors artificially at higher inclinations in the H-plane. For the E-plane the effect is not that much dominant as for the measured antenna #6. One problem remains, why is there an increase for V in the H-plane? For the gain calculation one might argue that the effect is overestimated, but why did it remain even for the fixed gain?

A minor aspect which one can observe is the bumpiness of the amplification factor curves in the H-plane, figure 4.16(b) but also weaker in E-plane, figure 4.16(a). There have been made laboratory measurements of this part of the electronics and one can clearly re-identify the bumps there at 47, 55-56, and 62-63 MHz. These effect is due to the amplifiers in the electronic chain.

4.3 Calibration Summary

For the analysis of the stored data of the LOPES experiment the system requires a calibration for the timing and the absolute amplitude.

Delay Calibration

The delay calibration consists basically of two parts. First, the delay for each electronic channel is verified with laboratory and solar burst measurements of single component behaviors. This delay is considered to be stable over the operation time of LOPES. Second, a phase calibration is performed in order to catch short-time fluctuations in the trigger signal distribution and the data read-out. The delay calibration is always performed in reference to one antenna and the absolute time is connected to the data using a KASCADE-Grande clock.

The rough delays from the laboratory measurements are adjusted using solar burst data and reach already sub-sampling time accuracy. For any change at the hardware the delay has to be verified again, here especially during the minimum of the solar cycle this is difficult to perform with solar bursts.

LOPES is operating three independent sub-stations with front-end electronics and requires the provision of the KASCADE-Grande trigger in each station. Here a jitter due to long transmitting intra-station cables can be introduced. On basis of a known reference source with constant phase relation these disturbing effects can be fixed. This finally gives a timing precision for the data analysis, which allow an angular resolution for a beam of 2° FWHM close to the zenith. Until 2007 a TV-transmitter could be used for the phase calibration, after its shutdown a new technique was developed.

With a self-made radio reference source the solar-burst rough delay correction as well as the TV-transmitter phase fine-tuning is replaced. For this purpose a discrete timing information, like a solar burst, and a constant phase at two or more frequencies, will be generated by this reference source. Then the relative delays and phases can be corrected on a single data file basis.

Amplitude Calibration
The absolute amplitude calibration was successful and detailed investigations of possible sources of systematic uncertainties lead to a total uncertainty of $\sigma_V/V = 70$ %. This total uncertainty also includes e.g. environmental effects, like those caused by different weather conditions present over nearly two years of calibration campaigns ($\mathrm{sys}_{\mathrm{calib}} = 20.5$ %), and a systematic uncertainty from the used reference source ($\mathrm{sys}_{\mathrm{reference}} = 67$ %).

Electronic modules are temperature dependent and we have shown that there is a relation between air temperature and amplification factor $V(\nu)$ for the LOPES antenna system. A more precise correlation analysis and following correction can improve the overall precision for measuring electric field strengths.

The systematic uncertainty of the calibration of the reference radio source itself contributes with ≈ 67 % to the total uncertainty. Using another, more precisely calibrated reference radio source would improve the accuracy.

The measurements at a dual-polarized antenna setup with two low noise amplifiers and cables next to each other indicate that a calibration of such a system is possible and reliable. There seems to be no significant cross-talk between the channels. The electric field strength for such a configuration can be measured with the same accuracy as for a single polarized antenna.

The antenna gain simulation contributes with large amount to the total uncertainty. The investigation of the predicted resonance at 58 MHz shows that it is artificial and

should be re-evaluated or interpolated in the gain calculations. It does not appear during the investigation using a spherical antenna gain pattern. For low inclinations the antenna is nearly isotropic in E-plane and H-plane, but changes significantly towards higher inclinations. The E-plane is in better agreement with the measurements, whereas the H-plane shows clearly some strong features not considered so far in the gain calculations. The pedestal is changing the absolute gain value by $\approx 15\%$ towards higher amplification factors. Finally, the 64 MHz and 72 MHz resonances in the H-plane are not properly understood. Therefore the calculations used for the antenna gain have to be checked in greater detail to reveal the influence of the pedestal. Measurements with an increased coverage of the directional pattern can help to improve the calculations.

An important conclusion is that the discussed strategy of calibration can be adapted for future radio antenna arrays measuring cosmic ray air showers. Especially at locations with much lower RFI an astronomical source, e.g. the galactic background radiation, can be used to cross-check the proposed amplitude calibration of a radio antenna system.

5. Lateral Distribution of EAS Radio Emission

Since the first discovery of radio emission in EAS in the last century (Jelley et al. 1965) until nowadays (Falcke et al. 2005), there was no suitable experiment that could investigate the absolute field strength properly. In recent times many effort went into detailed Monte Carlo simulations to close the gap between measurements and theoretical models (Huege et al. 2007a,b). The expected spectrum of the radio emission extents from the kHz range to several 100 MHz. The short radio pulses at observation level last for a few tens of nanoseconds in the shower center up to about 200 nanoseconds at 500 m distance.

With the existing LOPES experiment all requirements are fulfilled for a dedicated measurement to gain radio signal information that allow to perform direct comparisons with expectations from the theoretical calculations, see also section 2.3.1. In particular, with the performance of the delay and amplitude calibration for the LOPES experiment this goal is achieved, but also due to the fact that KASCADE-Grande is a well understood EAS detector. Given the rich information obtained for each detected event the radio detection technique can be tested and evaluated extensively. In the work of Ardouin et al. (2006) electric field profiles (EFP) for several events are discussed, that are quantitatively comparable with the lateral distributions presented here. However, a one to one comparison is not possible as the data sets are obtained for different frequency bands. Moreover, for the LOPES data set, only east-west oriented antennas are used, compared to both orientations for the CODALEMA data set.

In the following analysis the lateral extension of the radio signal in air showers will be investigated in detail and compared to predictions from parameterizations and simulations. The overall magnitude of the electric field strength can be investigated can compared with previous results.

5.1 Event Selection

The antenna configuration of LOPES has changed several times and different aspects of the radio emission could be studied with the corresponding configurations.

After the extension of the antenna field from 10 to 30 antennas in 2005 (LOPES30) the baseline, the number of antennas, and the LNA performance at the antennas improved (as described in section 3.2.1). The data set taken in the period from 16 November 2005 until 8 December 2006 is uses for the analysis. This data set uses a configuration of all antennas set up in east-west orientation. But with a linearly polarized LOPES antenna not only the east-west part of the total emission is measured. Due to the inverted-V geometry also an unknown fraction from a possible vertical component enters in the antenna. This effect can not considered in the estimation of the systematic uncertainty of the measured field strength, as the shower geometry and the position of the antenna very much changes the magnitude of the vertical component. The data taking was interrupted in Summer 2006, at 27^{th} of July. During a thunderstorm an over-voltage in the trigger distribution system occurred, breaking the trigger electronics. The whole antenna field was back in data acquisition in September 2006. Also in autumn 2006 a first step towards full emission measurement was done, by equipping three antennas with electronics for measuring the second polarization direction(north-south). For this reason the underground cabling of three antennas were re-routed and the necessary reliability tests for the operation were performed (section 4.2.4.2). For consistency, the affected antennas are flagged and not used in the analysis.

The trigger for the coincidence measurements of LOPES and KASCADE-Grande for the period of the data analysis was only the KASCADE 10/16-cluster condition. Nevertheless, the Grande stations have taken data as well most of the time. In the relevant period KASCADE generated 966.000 trigger that were sent to the LOPES DAQ-system. Not all of them could be processed due to the dead-time during the read-out of the radio data from the memory boards. About 860.000 data were recorded in LOPES, corresponding to a trigger efficiency of almost 90 % for the LOPES-DAQ. The main reasons for the dead-time are due to the internal data transfer and the writing process at the central DAQ.

5.1.1 KASCADE-Grande Reconstruction

For about 70 % of the reconstructed events also Grande reconstruction information is available and used for the data analysis. This available data set was reconstructed with the standard analysis software of KASCADE-Grande - KRETA. The EAS data reconstructed with KRETA (version V 1.17/01) and the stored LOPES radio data files are merged using their common time stamp. For each EAS, a corresponding time stamp is searched for in the LOPES data, resulting in a positive match only if the KASCADE-Grande experiment was in common data taking. This matching procedure provides the basis for a selection of data files of radio signal candidates.

The KASCADE-Grande experiment provides the reconstructed shower parameters, like number of electrons, number of muons, arrival direction, and core position. The reconstructed particle numbers are shown in figure 5.1. This two-dimensional shower size spectrum illustrates the distribution of all triggered showers, including showers that are not recorded by the LOPES system. The majority of the showers are at low particle numbers, respectively low primary energies, due to the steeply falling energy spectrum of primary cosmic rays.

Due to the fact that the total electric field strength scales nearly linear with the primary energy (equation 2.16; 2.18) the radio signal will be very low for most of

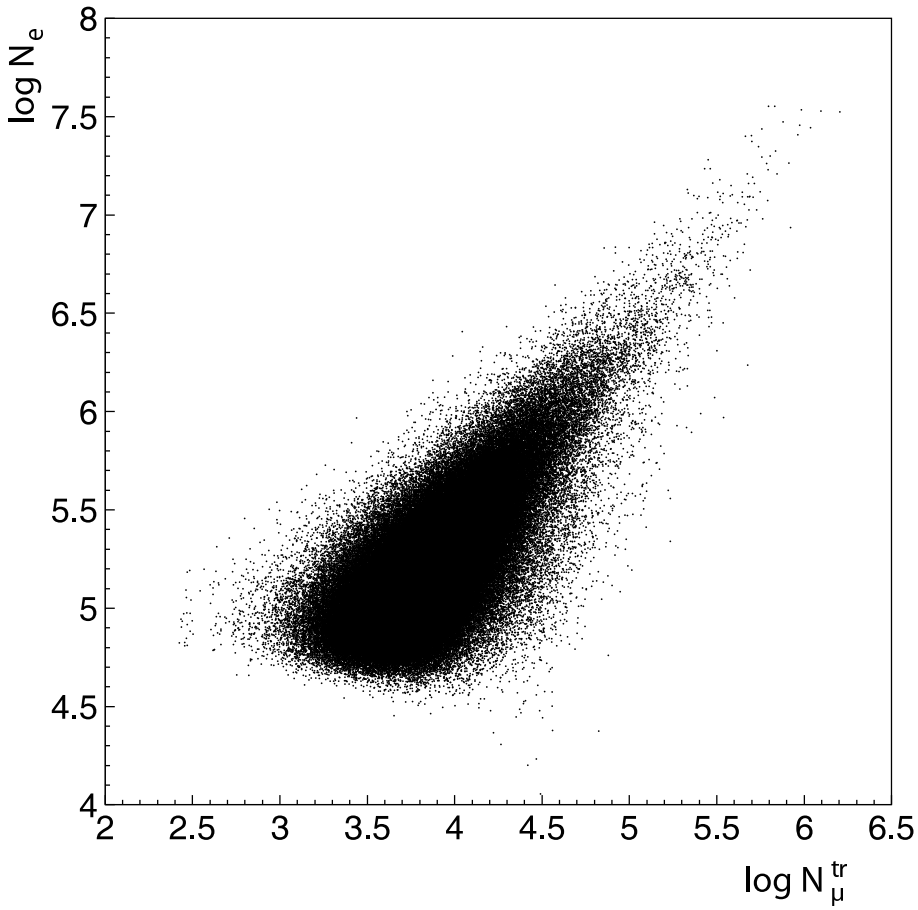

Figure 5.1: Two dimensional shower size spectrum with electron number N_e and truncated muon number N_μ^{tr} as reconstructed by KASCADE-Grande.

the showers, below the ambient noise level and, hence, the detection threshold of the LOPES antennas.

5.1.2 Selection of Radio Signal Candidates

The event reconstruction for the data set, as described in the previous section, was performed for all 860.000 showers. Only a small fraction of this large amount of data will show radio signals above the background, due to the high RFI at FZK and the present antenna sensitivity. This was one result from the analysis in, e.g. Falcke et al. (2005) or LOPES Collaboration et al. (2006).

Two chosen selections of the highest energy EAS can give promising radio signal candidates. The criteria of the two selections are listed in table 5.1. Both selections are based on the KASCADE-Grande reconstruction and the corresponding LOPES events. To achieve reliable reconstruction information, quality cuts have to be applied to the data set. The position of the shower core has to be inside the lateral extension of KASCADE-Grande, where a quadratic area of 580 m side length is used. The center position of the quadratic area is at -200, -200 in the KASCADE coordinate system and the area is about 0.3 km^2. The area was chosen to cover the KASCADE-Array as well as the center of Grande, to investigate shower at different distances from the antenna field. The lateral shape parameter s, the so-called shower age, has to be inside the range $0.4 < s < 1.4$ and no flag about a failed

Table 5.1: Parameter of the two selections used for the investigation of the EAS radio signal properties.

	Selection 2e7	Selection 5e5
Area for core position	580×580 m^2, center at x=-200, y=-200	
Particle number	$N_e > 2 \cdot 10^7$	$N_\mu^{tr} > 5 \cdot 10^5$
Candidates	176	232

reconstruction in KRETA has to be set. Showers with zenith angles les than 60° are selected since the KASCADE-Grande reconstruction quality drops significantly for larger angles.

The selection 2e7 contains all EAS with an electron number $N_e > 2 \cdot 10^7$ and the selection 5e5 contains all EAS with a truncated muon number $N_\mu^{tr} > 5 \cdot 10^5$. The truncated muon number is the reconstructed number of muons within 40–200 m of the shower core. A truncated muon number of about $\log_{10}(N_\mu^{tr}) \approx 5.5$ corresponds approximately to a primary energy of $3 \cdot 10^{16}$ eV. The systematic uncertainty of the reconstructed total muon number is around 15% (van Buren et al. 2005). For events with $N_\mu^{tr} \approx 5 \cdot 10^5$ the primary energy will be approximately $5 \cdot 10^{16}$ eV.

The sum of the selected events is $N = 408$, but the selection cuts are chosen in a way that they partially overlap each other. Therefore the number of unique events is $N = 296$ for this two selections and $N = 112$ events are common in both selections. In a second cut the zenith angle range is set below 44°, again because of the reconstruction performance of the EAS parameters in KASCADE-Grande. $N = 12$ events were found above a zenith angle of 44° and the resulting number of unique events, which are used for the present analysis is $N = 284$. The selected events are first analyzed with a pipeline tool in order to distinguish between events with significant radio signals above the background and events with no positive detection of radio signals. The criteria for a positive detection is a successful cc-beam fit (see section 5.2.1) which was fulfilled for nearly all selected high energy events and a radio pulse height larger than the background noise.

5.2 Pulse Height Calculations

For the investigation of the radio emission properties of the EAS one has to quantify the field strength from the radio data. The radio pulse from the EAS creates a voltage in the antenna that is digitized finally. The equation 4.14 is expressing the relation of the measured voltage and the field strength ϵ. Usually a distributed radio antenna field like LOPES or LOFAR is used as an interferometer. The advantage of such a system is that even signals not visible in a single antenna can be detected with the whole system. This is done by shifting the time series of the individual antennas channels to reproduce a coherent superposition of the signals arriving from a specific source direction. The phased array is superimposing the individual antenna signals and revealing the signal of, e.g. an astronomical source. This method is called beam forming.

5.2.1 Beam Forming of Radio Data

For the LOPES experiment beam forming is also used to recover the weak radio pulses from EAS. For the beam forming in a certain direction, the data of the antennas has to be shifted in time according to the antenna positions. This can be done for the antennas in reference to one antenna or for a certain position at ground, where all antenna have to be shifted. The shifts will be calculated in the rotated coordinate system according to the direction of the source. For distant sources, the incoming signal has a plane wave-front and the corresponding delays are then the relative differences in signal travel time to the specific antennas. The shifts are done in the frequency domain by Fourier transforming the time domain data and then multiplying a phase gradient to the data. This allows to do shifts by sub-sample steps, as the sampling rate of 80 MHz gives a 12.5 ns spacing of the time data.

In the case of the EAS radio emission, the source is not located at infinity. Typically a spherical wave-front is considered. This assumption is oversimplifying the time structure of the real radio emission front, but gives a better representation than a plane wave-front. The radius of this sphere, for an imaginary source location at a given distance, will modify the delays strongly for small curvature radii and at large distances from the axis to the source. From air shower studies of the longitudinal development, the maximum of particles is reached at altitudes below 10.000 m and, therefore, the radio signal is expected to originate from heights less than 10.000 m.

The studies of the antenna gain in section 3.1.2 have shown that the field of view of the individual LOPES antennas covers a large fraction of the sky. Consequently all radio sources in this region will contribute to the received signal. In figure 4.2 a spectrum from a LOPES data file is shown, revealing many features that can be ascribed to radio emitters. These narrow band radio emitters exceed the noise floor by orders of magnitude. During the analysis procedure these narrow band radio frequency interferences (RFI), e.g. the radio signals from a TV-transmitter are suppressed. The needed RFI mitigation will not affect the underlying spectrum of the radio emission. For the suppression, the mean value of the spectrum is calculated and frequency channels exceeding the mean by more than three standard deviations will be set to a reference values, which is one standard deviation above the mean. After this step is done the background in the data is significantly reduced and the radio pulse can be detected more easily. The individual antenna signal can be sometimes distorted by broadband RFI, that can not be filtered out. If the antenna performance is not properly operating the antenna will be flagged and not used for the analysis afterwards. This information is partly available in calibration tables. The antennas with good performance are used for the analysis, considering their status as a function of time.

With beam forming, one can calculate quantities that represents the averaged field strength of the detected radio pulse. There can be different beams calculated with the data, the beam that was used for the determination of the parameterization in equation 2.18 is the cc-beam. The data of each unique pair of antennas is multiplied, the resulting values are averaged, and then the square root is taken while preserving the sign:

$$cc(t) = \pm\sqrt{\left|\frac{1}{N_{\mathrm{P}}}\sum_{i=1}^{N-1}\sum_{j>i}^{N} s_i(t)s_j(t)\right|} \tag{5.1}$$

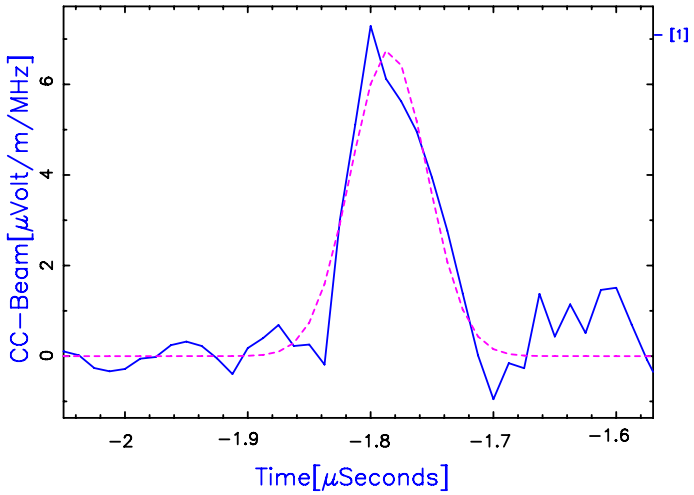

Figure 5.2: The calculated cc-beam for an EAS is fit with a Gaussian function after block-averaging with a window of 37.5 ns. The height [μV/m/MHz] and the center in time [μs] of the fit are used as parameters for the radio analysis.

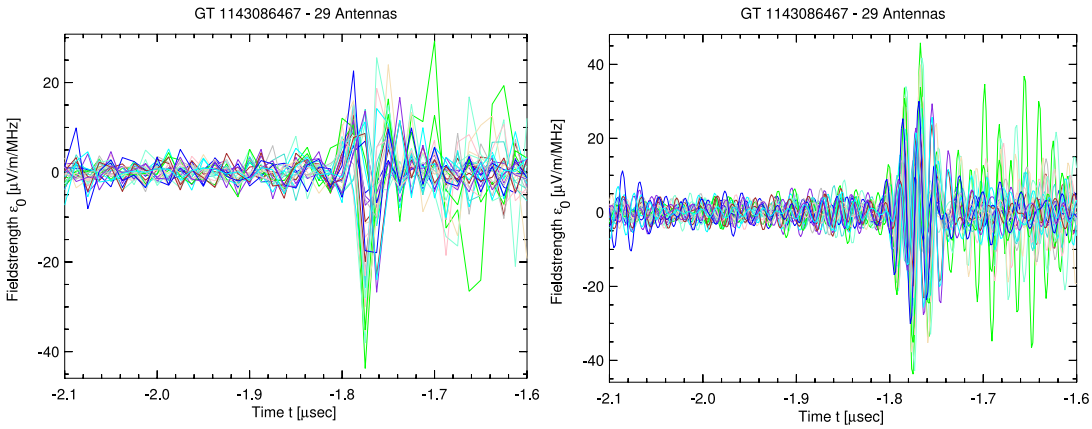

Figure 5.3: Left: The sampled data with 12.5 ns spacing of the digitization with 80 MHz, in the second Nyquist domain. Right: The upsampled signal shape between 40 MHz and 80 MHz with an upsampling factor $n = 3$.

From the number of unique pairs of antennas $N_{\mathrm{P}} = (N-1)N/2$ the normalization is determined. The cc-beam conserves the sign and the negative sign is taken if the sum was negative, before taking the absolute values, and the positive sign otherwise. The coherence of the single antenna signals systematically influences the height of the cc-beam. In other words, the cc-beam is sensitive to and reflects the coherence of the radio pulse. For the case of full incoherence the cc-beam becomes even negative. For the determination of the cc-beam pulse height, a Gaussian function is fitted to data, as shown in figure 5.2.

5.2.2 Upsampling of Radio Data

The analysis of the data using the cc-beam is based on the RFI cleaned raw data. However, the sampling of the data is done in the second Nyquist domain and a reconstruction of the original 40–80 MHz signal shape is needed to further investigate the radio emission properties. An upsampling of the data is preformed to reconstruct

the original signal form between the sampled data points with 12.5 ns spacing. The method used for upsampling is zero padding. The zero padding is a method to extend a time series or a spectrum. There will be zeros added in one domain and after Fourier transformation an interpolated series is obtained in the other domain. For the radio data the zero padding is applied in the frequency domain and gives a band limited interpolation in the time domain. The upsampling of a data set with N samples leads to a new data set with M samples. The size of M does not need to be an integer multiple of N. This is how ideal sampling rate conversion is accomplished. The sample rate conversion is the process of converting a signal from one sampling rate to another. The upsampling rate is given by $M/N = 2^n$, with $n = 0, 1, 2, \ldots$. The method can be applied, because the needed information after sampling in the second Nyquist domain are contained in the stored data.

An example how the method reconstructs the original signal shape is shown in figure 5.3. The zero padding can theoretically work up to infinity but the method will be limited by computing power and storage requirements. Therefore, one is enforced to choose an optimal upsampling rate. The zero padding is a method that results in convergence for the reconstructed signal shape and this will not change very much for large upsampling factors n. For the right plot in figure 5.3 an upsampling factor of $n = 3$ was used and the apparent asymmetric pulse height in the left plot turned out to be an effect of the second Nyquist sampling. After applying the zero padding to the LOPES data, the radio signals can be used to reconstruct the electric field strength in each individual antenna. The reconstruction informations from KASCADE-Grande are used to beam-form the data in the arrival direction of the shower and with an applied block-averaging the cc-beam is calculated. The center of a Gaussian fit gives the center of a time window with 45 nanoseconds width. In this time window the maximum of the absolute field strength for the upsampled data is searched for. The window width is chosen to exclude the RFI appearing soon after the radio pulse signal. The RFI is due to high currents in the particle detectors cables during the penetration of the EAS.

5.2.3 Systematic Uncertainty

The accuracy of the pulse height value depends on the performance of the system and this performance has systematic uncertainties. The result of the amplitude calibration in chapter 4 was not only an absolute value for the amplification of the LOPES antennas, but also an estimation of the systematic uncertainty for the method. The pulse height calculation will give an electric field strength ϵ that is measured by each antenna. Following equation 4.14 the measured voltage in the system is related to the electric field strength being present at the antenna. The quantities that enters in this relation, antenna gain $G_r(\nu, \theta, \phi)$ and amplification factor $V(\nu)$, have their own systematics. From the calibration, the power related systematic uncertainty was 20.5%, not including the uncertainty given for the reference source.

As a second source of uncertainty, the contribution of the background to the signal, has to be taken into account. To evaluate the background the mean value of the electric field strength from a time window before the expected radio pulse is calculated. The window width was chosen to 520 ns and the calculation is done for each antenna individually, ending 300 ns before the observed radio pulse. This value has to be added to the uncertainty for the field strength.

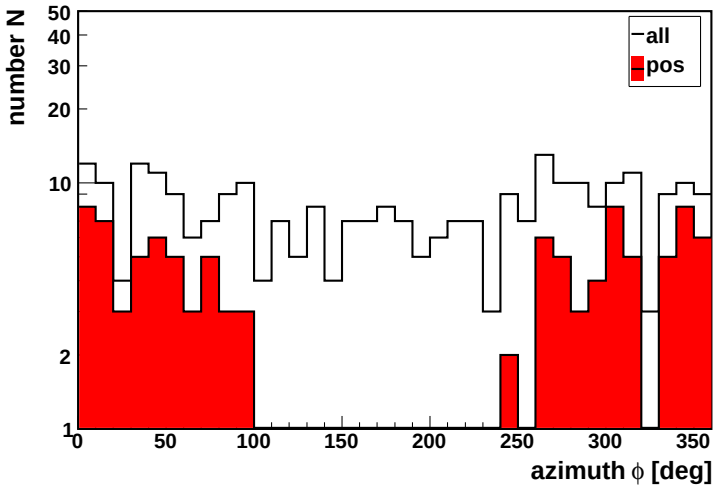

Figure 5.4: Distribution of the azimuth angle for all candidate events (white histogram) and the positive detected EAS (filled red). The logarithmic y-axis is chosen to reveal the very low number of detected EAS. No showers from south ($\phi \approx 180°$) could be detected. This indicates the importance of a geomagnetic field component transverse to the shower axis for a positive detection and, hence, the geosynchrotron mechanism.

There also could be a possible contribution to the systematic uncertainty from the upsampling procedure, as the upsampling rate influences the radio signal shape and therefore the estimated pulse height. Another contribution to the uncertainty is caused by the inverted-V antenna geometry and a possible reception of vertical components in the radio emission, but this contribution changes with the shower geometry and the relative location of the antenna field to the shower center.

The systematic uncertainty of the estimated electric field strength used for the analysis estimated to 19%, but not including contributions from the upsampling, other radio emission components, and the noise background. The uncertainty due to the background noise will be added afterwards to the combined systematic uncertainty.

5.3 Investigation of the EAS Parameter Properties

The EAS properties of the radio events satisfying the previously introduced cuts are now compared with the properties of the full KASCADE-Grande selection. The number of stored data (860.000 processed triggers) is much larger than the number of unique events for the two selections ($N = 284$) giving a fraction of ≈ 3000. 3000 is about the same number for the triggers that LOPES processes per day, respectively one high energy candidate event per day is saved. Figure 5.4 gives the azimuth and and figure 5.5 the zenith angle distribution for all positive detected events (filled red histogram) and for all selected events (underlying white histogram). The criteria of positive detection was the successful cc-beam fit and a radio signal over noise per antenna, for the radio pulses found in the 45 ns window around the cc-beam center.

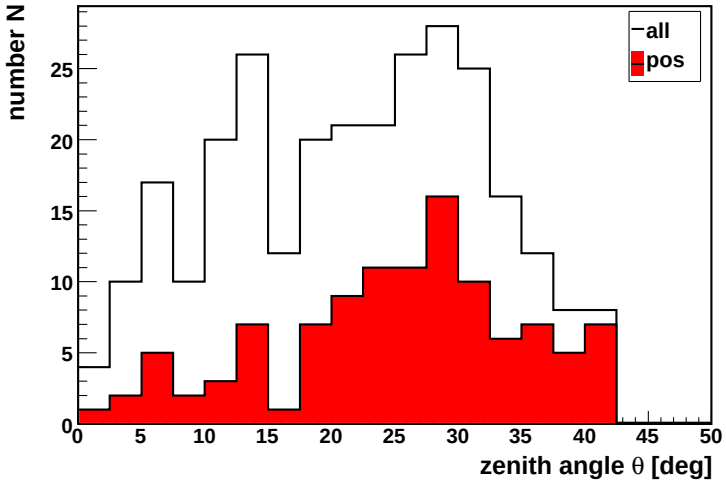

Figure 5.5: Distribution of the zenith angle for all candidate events (white histogram) and the positive detected EAS (filled red histogram). The fraction of positive detected EAS is about one half for zenith angle below 35 degrees. Above the fraction is significantly higher.

The mean value for the azimuth angle of all selected events is 181.3° and the events are almost uniformly distributed over the whole angular range. An azimuth angle of 180° corresponds to shower arriving from the South. For this direction the angle to the geomagnetic field is lower than for shower coming from the North. The declination of the geomagnetic field is $D = 0.998$ degrees from the South and the inclination is $I = 64.806$ degrees. The orientation and total intensity of 48177 nT at coordinates 49° 5' 33" N, 8° 25' 33" O, 110.4 m NN are taken from the 10^{th} Generation International Geomagnetic Reference Field (IGRF), (Maus & Macmillan 2005), released by the International Association of Geomagnetism and Aeronomy (IAGA) [4]. Therefore, showers from south are almost parallel to the magnetic field and the resulting Lorentz force (equation 2.11) is very small. If, in addition to an incoming direction from south, the zenith angle of the shower direction is about 25 degrees the magnetic field lines are virtually parallel and almost no radio emission is expected. The distribution in figure 5.4 is a first indication, that there is a geomagnetic origin of the radio emission.

The zenith angle distribution in figure 5.5 has a mean of 22°, which is in agreement with the distribution of zenith angles of all KASCADE-Grande reconstructed events. For zenith angles below 20° the fraction of detected events to selected events is below 50%. Above 35° the detection efficiency becomes much higher. Furthermore, the absolute number of candidates and the absolute number of detected events decreases towards the zenith.

In figure 5.6 the distribution of the geomagnetic angle α is shown for the selected events. The detection efficiency is very high for large geomagnetic angles and this can be taken as another indication for the underlying geosynchrotron mechanism. For large angles, $\alpha > 50°$, the fraction of positive detected events to the full selection is

[4] Via the web page interface http://www.geomag.bgs.ac.uk/gifs/igrf_form.shtml for a certain location the magnetic field can be obtained.

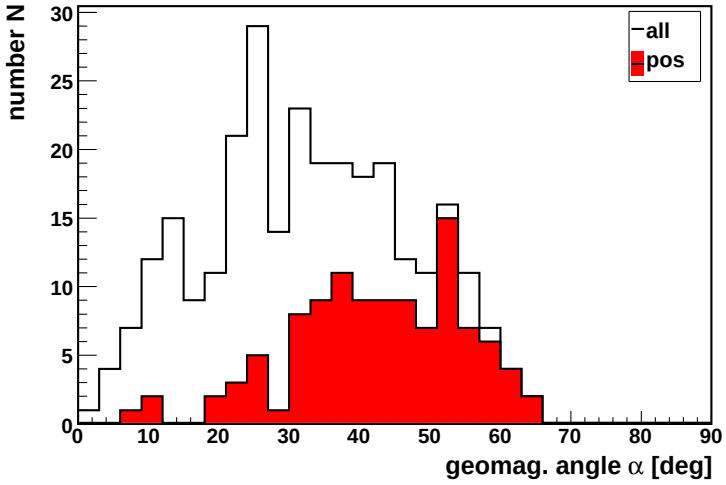

Figure 5.6: The geomagnetic angle α of the EAS from the two selections 2e7 and 5e5 is shown. The fraction of positive detected events is very high at large angles (red filled histogram) compared to almost no events for small angles and the full candidate list (white histogram).

larger than 90%. The geomagnetic angle incorporates the azimuth and zenith angle distributions, as both angles have to be used to calculate the geomagnetic angle α:

$$\cos\alpha = \cos\phi \sin\theta \cos\phi_b \sin\theta_b + \sin\phi \sin\theta \sin\phi_b \sin\theta_b + \cos\theta \cos\theta_b \tag{5.2}$$

The orientation of the magnetic field at the LOPES location is given by $\theta_b = 25°$ and $\phi_b = 180°$.

Concluding from this discussion, a general rule can be derived, that inclined showers with large geomagnetic angles will have a larger signal-to-noise ratio, compared to nearly vertical showers, being close to the orientation of the Earth's magnetic field. Therefore, any experiment for radio detection of EAS should have a good performance in the zenith angle range, that gives large geomagnetic angles at the experiment location. Furthermore, a high detection efficency should occur in the corresponding parameter space. This is especially crucial in for detections at the threshold, or high noise background, as in the case for the LOPES experiment.

The cut on large muon numbers N_μ^{tr} already selected high primary energies. The primary energy E_{guess} is roughly estimated from KASCADE reconstructed shower observables. This estimation is valid up to zenith angle $\theta \approx 40^c irc$ and works only in the KASCADE energy range.

$$\log_{10} E_{\mathrm{guess}} = 0.3015(\log_{10} N_e + A) + 0.6762(\log_{10} N_\mu^{\mathrm{tr}} + B) + 1.856 \tag{5.3}$$

The two factors $A = 14.9(1/\cos\theta - 1.025)$ and $B = 2.86(1/\cos\theta - 1.025)$ are corrections, that include the zenith angle θ. A systematic uncertainty for the primary energy of about 15% is considered. The calculation for the primary energy in Grande is based on a similar parameterization equation:

$$\log_{10} E_{\mathrm{guess}} = 0.319 \cdot \log_{10}(N_e) + 0.709 \log_{10}(N_\mu) + 1.236/\cos(\theta) + 0.238 \tag{5.4}$$

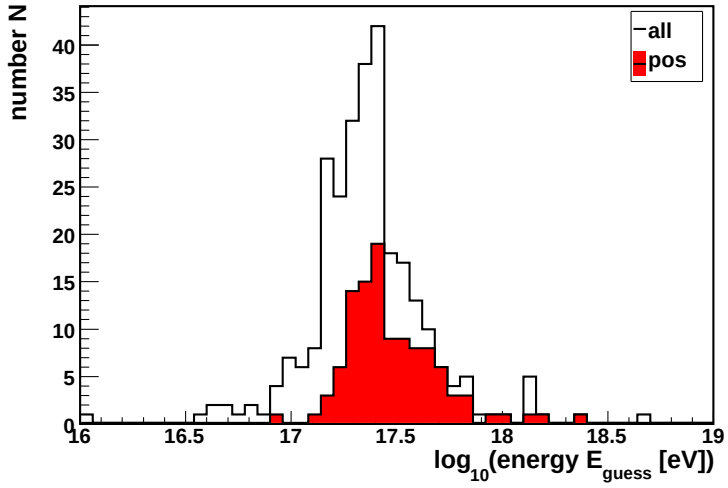

Figure 5.7: The histogram shows the distribution of the estimated primary energy E_{guess} for all candidate events (white histogram) and the positive detected EAS (filled red histogram). The majority of the EAS has energies above $\log_{10} E > 17.2$.

The valid range for the parameterization is for zenith angles below 50 degrees, with an rough uncertainty in energy of $\log_{10} E = \pm 0.15$ in the valid angular range. The obtained distribution of the guess primary energy is shown in figure 5.7. Only showers with an energy $\log_{10} E > 17$ are present in the selections, which indicate that there is a high detection threshold for radio emission at the LOPES location. This is additionally a consequence of the selected high energy events.

Figure 5.8 (left) shows the relation of the total muon number to the guessed primary energy E_{guess}. It is obvious that one can derive easily that they are very strongly correlated, which is not the case of the more zenith angle dependent electron number N_e (figure 5.8, right). That means, that a selection based on either muon number or energy is giving a similar set of radio signal candidates. The truncated muon number turned out to be a good tracer for the primary energy at KASCADE, $E_{\text{guess}} \propto (N_\mu^{tr})^{0.9}$ (KASCADE Collaboration et al. 2002). For EAS reconstructed by KASCADE or only by Grande a possible systematic shift could occur in the energy estimation, but the calibration of both detector components give reasonable agreement and no shift is observed.

5.4 Lateral Distribution of the Radio Signal in EAS

The aim of the high energy selection was to pre-select EAS with an expected high signal-to-noise ratio for the radio signals. The high noise background at the location of LOPES requires this already, in order to detect a showers at all. From the previous discussions we obtained, that the even not all of these high energy events ($> 10^{17}$ eV) give a positive detection. Nevertheless, the coincidence measurements with KASCADE-Grande allow us to investigate them. For investigations of the lateral behavior of the radio signal in individual antennas the positive detected events can be used only, giving a total number of events of 110.

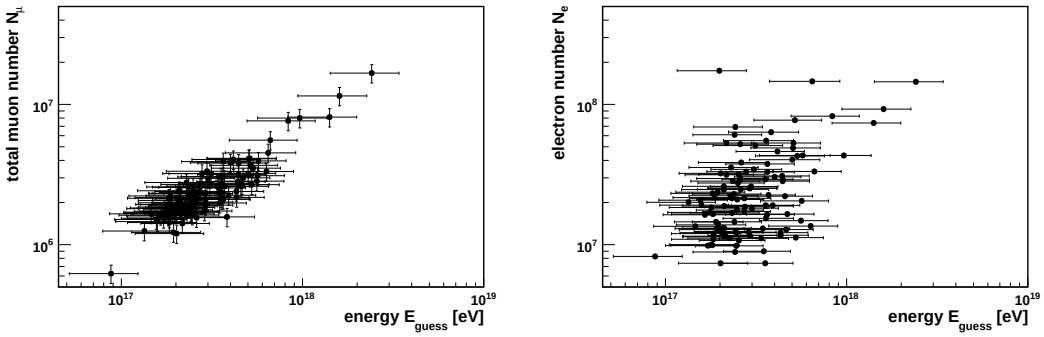

Figure 5.8: Correlation of the primary energy E_{guess} and the measured particle numbers from KASCADE-Grande. Left: For the total muon number N_μ a systematic uncertainty of about 15% is assumed and for the energy the uncertainty is obtained from parameterizations. Right: Distribution of electron number N_e and primary energy E_{guess}.

The quantity that describes the lateral behavior is the scale parameter R_0 in an exponential function, as introduced in the equations 2.16 and 2.18. The exponential decline of the electric field strength has a decay constant of $1/R_0$ and the value of this decay constant will be investigated in several aspects. The constant of integration ϵ_0 denotes the quantity at distance equal to zero, here, it is the maximum field strength for the radio emission of EAS at the shower core. From the measurement point of view a large scale parameter would be preferred, as it allows to measure still at large distances from the shower core. Moreover, the field strength in the shower core is expected to scale with primary energy, which has to be verified.

5.4.1 Lateral Distribution Antenna Sub-sets Investigations

The parameterization equations 2.16 and 2.18 are based on averaged quantities, that are derived from all antennas of an experimental setup. With the extended antenna field and sufficient enough large baseline the investigation can be extended to groups of antennas. The calculation of the cc-beam requires a minimum number of antenna pairs, that can be used for the beam forming. With a suitable shower geometry it is possible to form sub-sets of antennas, to reconstruct the lateral distribution.

The choice of antenna sub-sets can be seen as an intermediate solution to investigate the lateral distribution of the radio emission in EAS. The method is based on the cc-beam calculation, which limits the accuracy of this investigations. There are equidistant radial ranges in the shower coordinate system composed, in order to get reasonable number of antennas for all ranges. There are two showers in the selection with very similar EAS properties (table 5.2). The shower geometry allow to find sub-sets with enough antennas to calculate the cc-beam for them (see figure 5.9). The radial distance ranges are rings with 50 m width, starting at the shower core and ranging up to more than 150 m. According to this ring width and the shower geometry, there are four ranges for the first shower and three ranges for the second shower. For these rings the cc-beam pulse heights are determined. There are 5, 9, 10, and 5 antennas in the four rings of shower 1 and 7, 12, 13 antennas in the three rings of shower 2. The core of shower 2 is more inside the antenna array, which gives shorter lateral distances, than for showers at the edge of the antenna

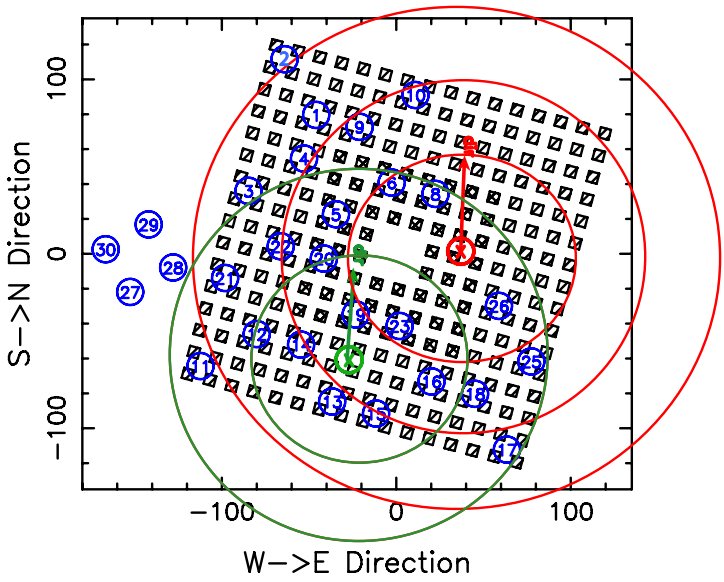

Figure 5.9: For two very similar EAS (red and green) with shower core inside the KASCADE-Array (cross and arrow), circles for distance ranges of about 50 m illustrate the sub-sets of antennas that are used to calculate the cc-beam pulse height.

	Shower 1	Shower 2
Core x,y [m]	35.29, 10.98	-9.24, -65.00
Direction ϕ, θ [deg]	2.33, 24.06	4.89, 23.82
N_e, N_μ^{tr}	$1.82 \cdot 10^7$, $9.01 \cdot 10^5$	$1.86 \cdot 10^7$, $8.13 \cdot 10^5$
Primary energy [eV]	$(3.0 \pm 1.2) \cdot 10^{17}$	$(2.75 \pm 1.1) \cdot 10^{17}$
cc-beam, all antennas [μV/m/MHz]	6.8 ± 0.5	6.5 ± 0.8

Table 5.2: EAS parameters of the two showers used for the sub-set investigation of the lateral distribution.

field. The optimum for such investigations will be a balance between detectable field strength and large lateral extents. Both plots in figure 5.10 show the field strength [μV/m/MHz] as a function of time. The field strength of the antennas for each ring are color-coded, starting with red for the closest, then black, green, and finally blue.

In section 5.2.1 it was described, who the cc-beam calculation is performed. For the sub-sets of antennas one cc-beam per ring is calculated and the pulse height CC_{ri} is derived (figure 5.11). Only the uncertainty of the peak height of the Gaussian fit is used as uncertainty for the height. The distance R of the data points is derived from the mean of the single antenna distances in each ring. The distance is calculated in the shower coordinate system and the RMS is used as uncertainty. The lateral distributions for both showers are very similar, as expected due to of the very similar initial EAS parameters. Furthermore, the lateral distribution shows the expected exponential decay and the function that is used for the fit is:

$$CC_{ri} = \epsilon_0 \cdot \exp(-R/R_0) \tag{5.5}$$

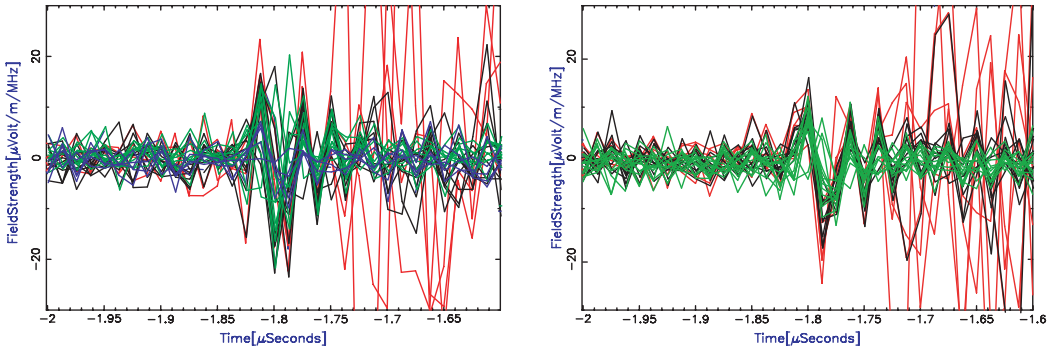

Figure 5.10: Field strength [μV/m/MHz] for sub-sets of antennas for two similar showers as a function of time t. The color-code represents the radial distance ranges from the shower core, red - 0–50 m, black - 50–100 m, green - 100–150 m, blue - >150 m. Left: Shower 1 Right: Shower 2

The fit is applied to all data points, treating the two showers like one event. The parameters of the fit are: $\epsilon_0 = (14.71 \pm 1.74)\mu$V/m/MHz and $R_0 = (131.8 \pm 21.4)$ m. These values are comparable with results that one can obtain from the parameterization in equation 2.16, where for vertical showers a scaling parameter of $R_0 = 110$ m at 55 MHz is used. But also the parameterization results from Horneffer et al. (2007) are within their range of uncertainty in agreement with the fit results.

The method itself can be applied to data that are at the detection threshold of a radio antenna array, which makes use of the interferometric superposition of individual antenna signals. The noise background, the amplitude calibration uncertainty, and the timing precision will be the limiting quantities for the applicability of this method.

5.4.2 Lateral Distributions by Single Antennas

An investigation of the lateral distribution by single antennas requires clear radio signals in almost all antennas. The method that is used to determine the radio pulse height on a single antenna basis was described in section 5.2. The field strength per unit bandwidth is calculated from the measured voltages using equation 4.14. The cc-beam is calculated for each event and afterwards the raw data of the event are upsampled (see section 5.2.2). In a time window of 45 nanoseconds width the absolute field strength for each antenna is determined. The present background for each antenna will be calculated in a time window (520 nanosecond width) before the radio pulse and added to the systematic uncertainty. The analysis of sub-sets of antennas used a fit function that contains two parameters ϵ_0 and R_0 for describing the lateral distribution based on single antennas. Now the cc-beam pulse height will be replaced by the field strength ϵ of a single antenna.

$$\epsilon = \epsilon_0 \cdot \exp\left(-\frac{R}{R_0}\right) \tag{5.6}$$

The number of antennas for the determination of the two fit parameters can change from event to event, because of an event by event evaluation of the single antenna signals. An antenna can be flagged, if the signal is disturbed by too high noise, a lack

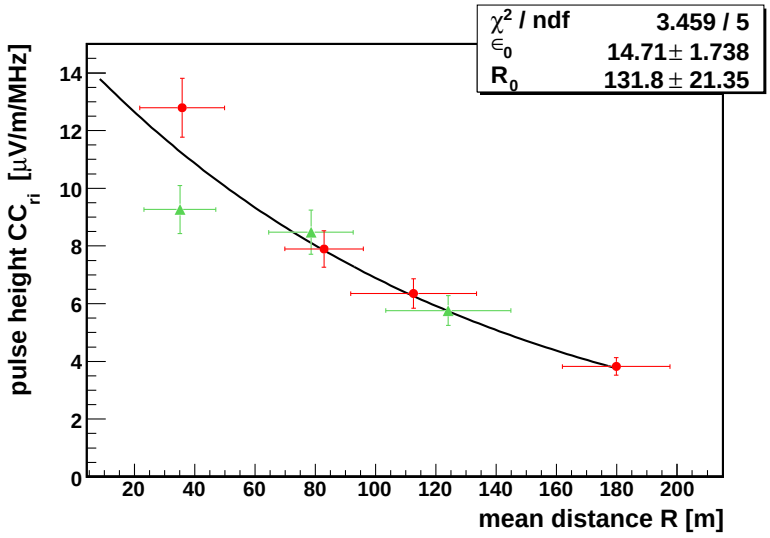

Figure 5.11: Lateral distribution for two very similar events, giving the pulse height CC_{ri} as function of the distance R. The fit function $CC_{\mathrm{ri}} = \epsilon_0 \cdot \exp(-R/R_0)$ is applied to all data points.

of signal strength, or a bad timing. Furthermore, in the later period of the analyzed data set, three antennas that have been rotated to the north-south direction and they are flagged as well. These antennas will either not appear or will be marked red in the following lateral distribution plots.

5.4.2.1 Lateral Distribution of Sub-set Showers

The upsampled data of the two showers investigated in sub-sets of antennas are shown in the upper part of figure 5.12 and after calculating the field strength for each antenna the lateral distribution can be plotted, lower part of figure 5.12. For the reconstruction of the original signal shape an upsampling rate of $n = 3$ is applied. The upsampled data are analyzed on a single antenna basis and the scale parameter R_0 and the maximum field strength ϵ_0 are determined from a fit, see equation 5.6. Once again, the large post-shower RFI from the KASCADE detectors is very pronounced in many antennas. There have been made approaches to reduce this RFI, but no final solution was found and the recommendation for other experiments and studies is: choose a radio quiet environment.

The two legends in all lateral distribution figures give in the middle box the event ID, the guess energy E, and the orientation of the shower axis (ϕ, θ), and on the right-hand side box the fit results. In the lower part of figure 5.12 the lateral distributions of the two showers investigated with sub-sets of antennas are shown and there fit results are:
Shower 1 - $R_0 = (160 \pm 12)$ m and $\epsilon_0 = (25 \pm 1)$ μV/m/MHz
Shower 2 - $R_0 = (144 \pm 12)$ m and $\epsilon_0 = (17 \pm 1)$ μV/m/MHz

These values do not differ very much from the result of the cc-beam pulse height CC_{ri} analysis, which results in values of $\epsilon_0 = (14.71 \pm 1.74)\mu$V/m/MHz and of $R_0 = (131.8 \pm 21.4)$ m. The field strength at $R_0 = 0$ m is somewhat lower for the cc-beam field strength, compared to the lateral distribution by single antennas. Due to a different handling of the antenna flagging, the lateral distributions by single

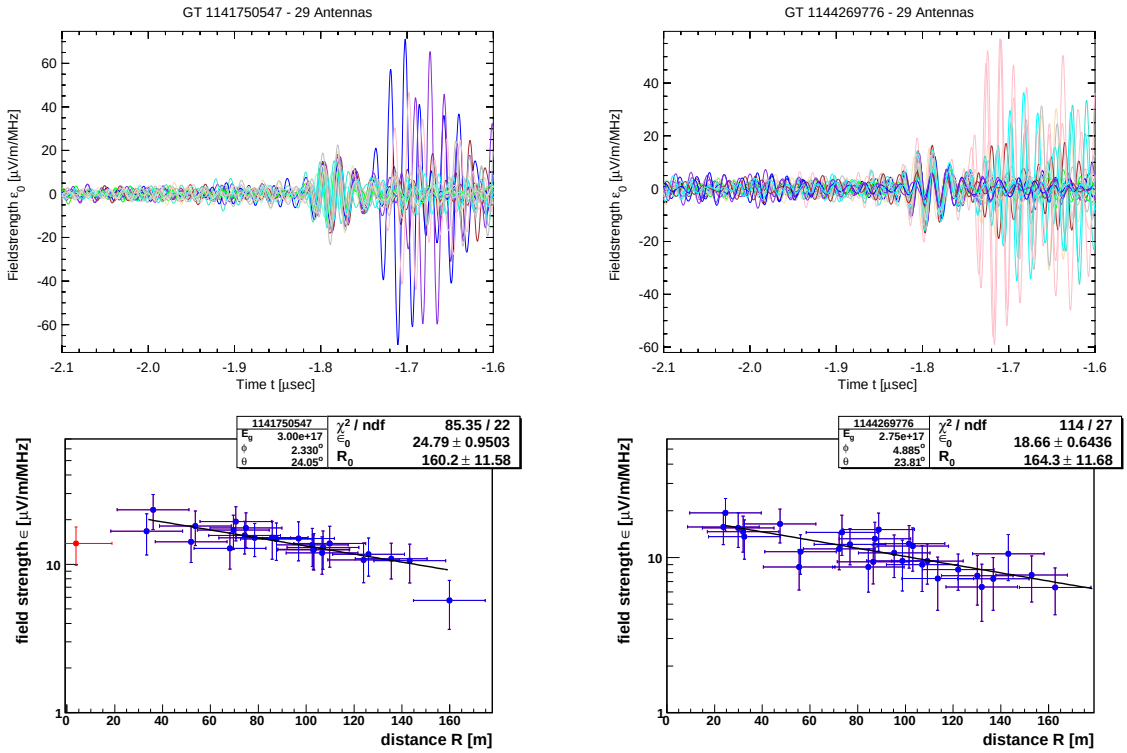

Figure 5.12: Top: Upsampled data of the two sub-set showers, using an upsampling rate of $n = 3$. Bottom: Lateral distribution reconstructed from single antenna signal, shown for the two showers investigated in section 5.4.1, with similar EAS properties. Left: Shower 1 Right: Shower 2

antennas do not extend to the same large distance, as given for shower 1 (compare figure 5.11 and lower left panel of figure 5.12).

The two showers, which were investigated also by the antenna sub-set method, are shown here exemplarily for almost all 110 investigated events. The lateral distributions using single antenna radio signals of all detected showers can be found in the appendix B. In most cases the exponential decay with increasing distance to the shower axis was found. The expectation from simulation studies is as well an exponential decay for the lateral distribution.

5.4.2.2 Discussion of Special Distributions

For some events lateral distributions were found, which do not show the expected exponential decay. Four of these special distributions are shown in figure 5.13. A common feature of all of them is, that they have a zenith angle of $\theta > 30°$. The shower in figure 5.14(a) shows apparently an exponential decay as others do, but there appears a flattening for distances smaller than about 140 m. Maybe, a fit of two exponential functions could better describe the lateral profile. One exponential function to describe the almost flat part close to the center and afterwards a second exponential function to describe the usual decay. There are some of these showers in the two selections that exhibit such a slope change in the lateral distribution. Also, for the shower in figure 5.14(b) a slope change at a distance of about 90 m can be seen. In addition, this particular shower shows a lateral distribution that is very flat for the distance range up to 90 m.

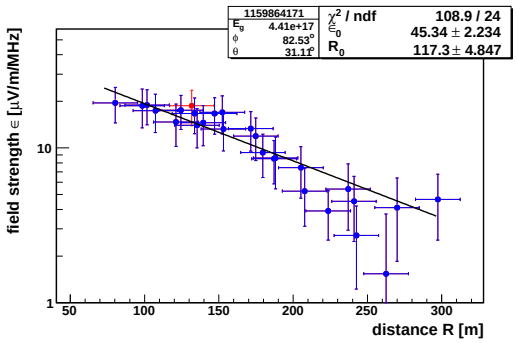

(a) Slope change at about 140 m. Flattening of the lateral shape closer to the shower center.

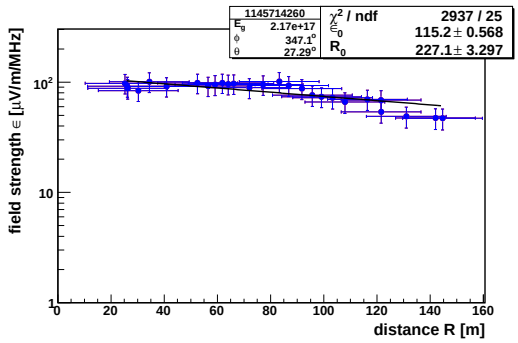

(b) More flat lateral shape, including an index change at about 90 m.

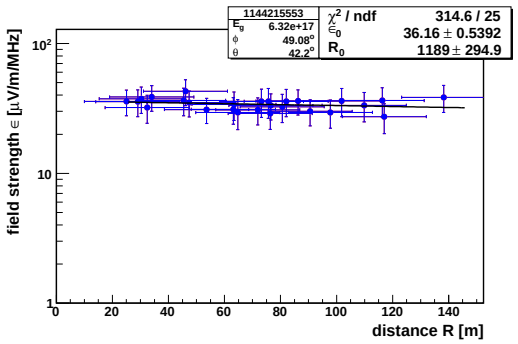

(c) Almost no exponential decay in the full range.

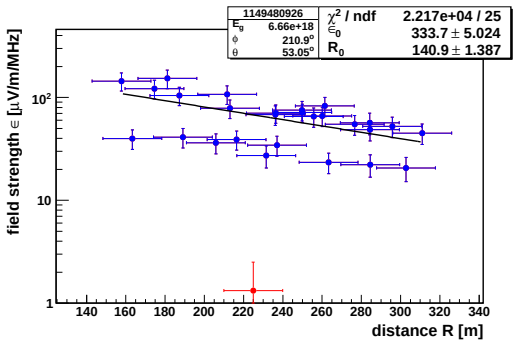

(d) Very unusual distribution with seemingly two groups of lateral distributions.

Figure 5.13: Four lateral distributions with special shapes.

The even more extreme case of a flat lateral distribution is shown in figure 5.14(c). Over the whole distance range that could be measured, there is almost no exponential decay observed. The field strength is at a level that the ambient noise background can not effect the measurement. For a statistically reliable analysis there are just measured too few of such flat lateral profiles. Nevertheless, instrumental effects can be excluded as the explanation of such shapes, which makes them even more astonishing.

The last discussed special lateral distribution (figure 5.14(d)) is an exception in all concerns, e.g. this shower is not included in the final selection. The reconstruction lead to an inclined shower at zenith angle of $\theta = 53°$ and a shower core found in the center of the Grande array. This means, that all antennas are located in the north-east of the shower core and relatively distant. No reason could be found to explain the splitting in two parts of the field strength. Neither antennas could be distinguished by their geometric location in the shower coordinate system nor there are strange environmental conditions present, like a thunderstorm. But, the positive detection indicates that measurements of radio signals far outside the antenna area are possible, at least for high energy inclined events and that the nature of theses lateral distributions seems to be not well understood.

The case studies of special lateral distributions is presently limited in statistics and demands a much larger data set. However, the found lateral distributions show unexpected features, which requires also detailed informations about all shower aspects. In this connection the EAS properties can be very important to understand

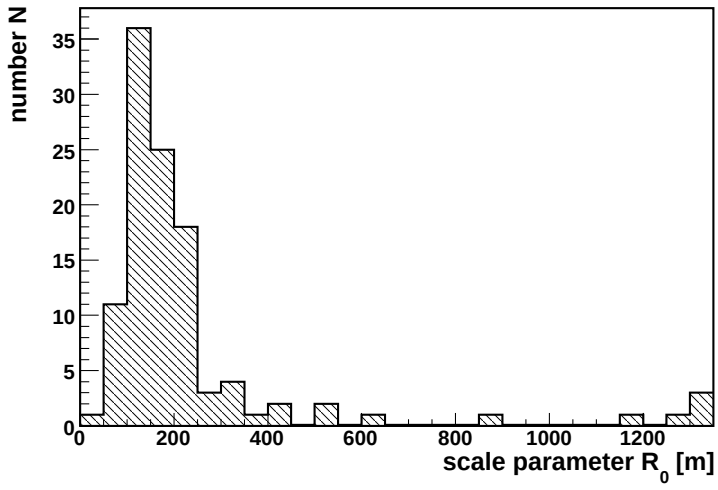

Figure 5.14: Histogram of the scale parameter R_0. The majority of the events have a values smaller than 200 m. There are four events at $R_0 = 1300$ that have are overflows, with actually higher values.

the obtained lateral profiles. Also the role of possible polarization effects and the contribution from vertical components, measured with the LOPES antennas, have to be considered. That there are generally lateral distributions found with special shapes is an advantage of the method. A single cc-beam pulse height can not study such features. Most probably also the intermediate solution using radial bins for the cc-beam pulse height can not fully investigate such features.

5.4.3 Investigations of the Scaling Parameter R_0

One of the two fit parameters in equation 5.6 is the scale parameter R_0. For studies of lateral distributions it is important to investigate the properties of this scale parameter and possible correlations with EAS parameters. In case of the LOPES experiment this can be done easily, as the shower parameters are obtained from the KASCADE-Grande measurements. From the investigation of the showers a distribution of the scale parameter R_0 can be obtained, see figure 5.14. Most of the showers have a scale parameter smaller than 300 m. There are some showers with extremely large scale parameter, $R_0 > 1300$, that are set in the plot to $R_0 = 1300$. They appear as the peak in the right part of the histogram. The distribution peaks at a scale parameter $R_0 \approx 125$ m and has a mean value of $R_0 = 237$ m for the complete selection.

The scale parameter describes the shape of the lateral distribution. From the discussion of the unusual distributions one implication can be, that the shower direction can play a role for the obtained shape of the lateral distribution. In order to test this, the scale parameter is correlated with the geomagnetic angle α (using $1-\cos\alpha$), the azimuth angle ϕ, and the zenith angle θ (figure 5.15). No correlation is found between any of the angles and R_0. The azimuth angle distribution shows significantly less positive detected showers from south $\phi = 180°$, which is already seen in figure 5.4. The tendency that inclined showers exhibit a larger scale parameter can not be directly proven, as the quality cut for the zenith angle larger than 44° inhibits any further conclusions.

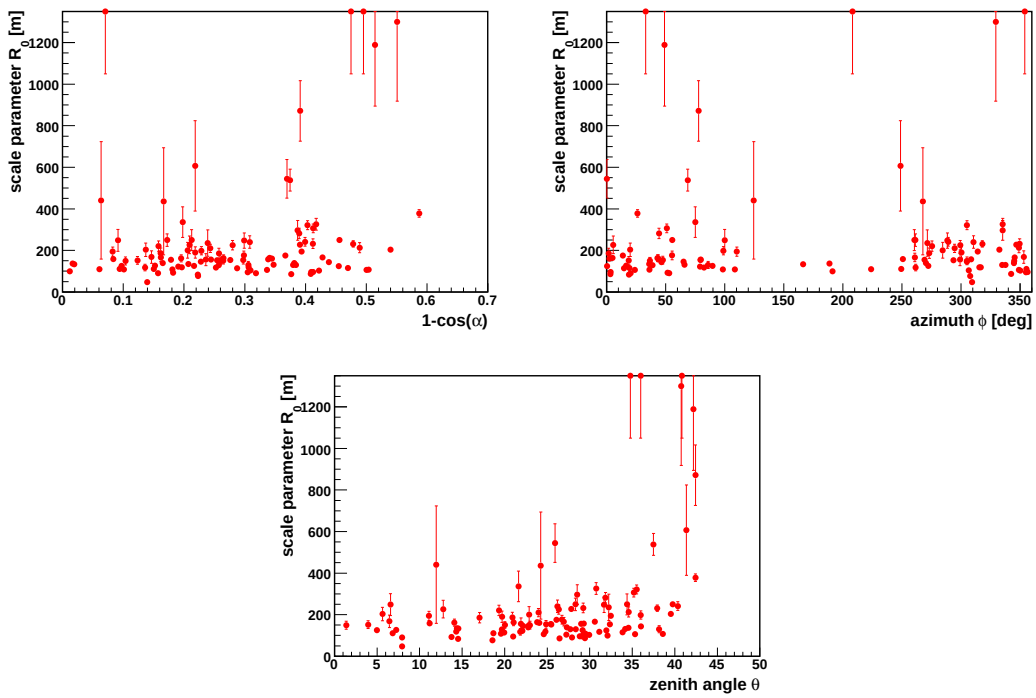

Figure 5.15: Relations of the scale parameter R_0 with geomagnetic, azimuth, and zenith angle. The data points at the upper border of the plots are set to $R_0 = 1300$ m, but their actual value is higher.

The particle numbers are basic observables of the EAS reconstruction. Therefore, the scale parameter has to be checked about correlations with the electron number N_e and the total muon number N_μ, upper panels of figure 5.16. For the total muon number N_μ no correlation is present, recalling that the muon number was a rough estimator for the primary energy. Large scale parameters can be found for small electron numbers, which can be an effect of the shower development. Inclined showers have smaller electron number, due to the large absorption in the atmosphere. The comparison of the scale parameter with the zenith angle does not show a strong correlation. Another comparison for the scale parameter is done with the guessed primary energy (lower panel in figure 5.16). Like the comparison with the muon number, the scale parameter shows no dependence on the guessed primary energy.

The scale parameter R_0 as shape describing quantity, obtained from a fit of an exponential function to the lateral distributions using single antenna radio signals (equation 5.6), has a peak value of $R \approx 125$ m and a mean of $R = 237$ m, which is consistent with previous results, (Allan 1971; LOPES Collaboration et al. 2006; Horneffer et al. 2007). Furthermore, no direct dependence on EAS parameters could be found, which indicates that the shape of the lateral distribution is an intrinsic property of an individual shower.

5.4.4 Investigations of the Field Strength ϵ_0

The second fit parameter in equation 5.6 is the field strength ϵ_0. This parameter is representing the field strength at the shower center, which one could measure there. For studies of lateral distributions, it gives the absolute scale of the distribution and their relation with the primary energy was already suggested in equation 2.18,

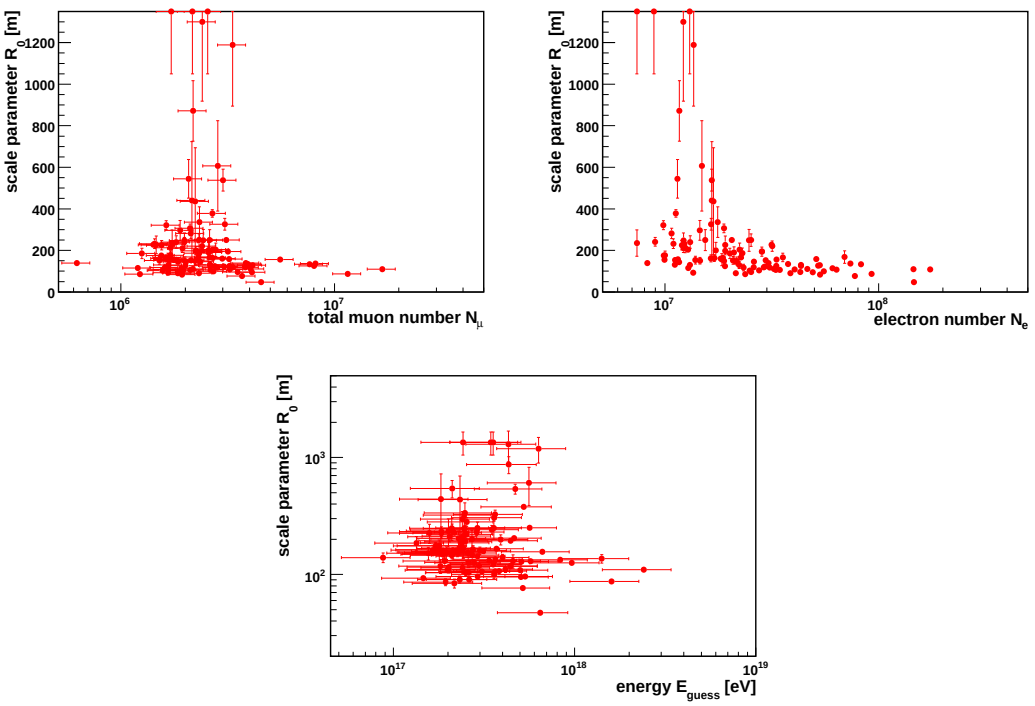

Figure 5.16: Relation of the scale parameter R_0 with particle numbers of muons, N_μ, and electrons, N_e, in the upper panel. The comparison with the guessed primary energy E_{guess} is shown in the lower panel.

which relates shower observables with the radio emission field strength. In this parameterization the power law index for the term of the primary energy is $\kappa = 0.95 \pm 0.04$. Also from simulations a relation is expected, that can be described with an index κ, like $\epsilon_0 \propto E^\kappa$, with a range between 1 and 0.75. It can change with the depths of the particle number maximum (X_{max}) as a function of primary energy.

For the lateral distributions the fit for the field strength ϵ_0 yields in most cases a reliable value, as the corresponding fit uncertainties are low, except for some cases with larger scatter for the individual antenna signals. Figure 5.17 shows the relation of the ϵ_0 versus the guess primary energy E. One outlier, with $\epsilon_0 \approx 200\mu$V/m/MHz and $\approx 2 \cdot 10^{17}$ eV, belongs to the group of shower that flattens to the center, and therefore, the fit overestimates the field strength close to the core. The reconstruction uncertainty for the primary energy, as well as the systematic uncertainty in the amplitude calibration was taken accurately into account, to exclude possible contributions. The diagonal in figure 5.17 is following a power law with index $\kappa = 1$ and does not originate from a fit. The absolute scale for the diagonal was set to $\epsilon_0 = 8\mu$V/m/MHz at $1 \cdot 10^{17}$ eV according to the parameterizations given in equation 2.16 and equation 2.18.

Due to the high detection threshold for the radio emission from EAS and the limit in the energy range for the KASCADE-Grande experiment most of the showers are at low energies. The obtained correlation supports the expectation of a scaling of the field strength ϵ_0 with the primary energy E_0.

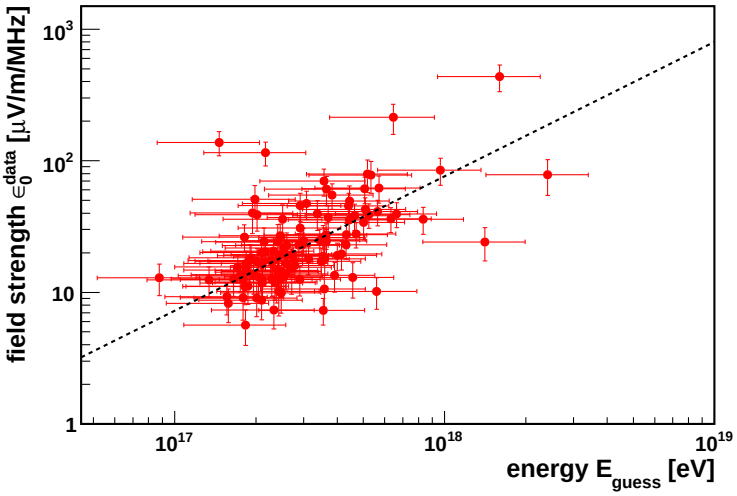

Figure 5.17: The field strength at the shower center ϵ_0 as a function of the primary energy E_{guess}. ϵ_0 is the result of a fit to the lateral distribution of single events. The diagonal is following a power law with index $\kappa = 1$.

5.5 Comparisons with Parameterization Results

The parameterizations described in equation 2.16 and 2.18 are derived from investigations of the radio emission using antenna arrays, but combined the detected electric field strength ϵ in a single quantity, like done with the cc-beam pulse height for the LOPES experiment. Using results of lateral distributions comparisons with the results of these methods can be performed. For the parameterization in equation 2.18 the calculated cc-beam for all antennas uses an averaged antenna distance. For a present baseline of about 270 m for LOPES30 the mean distance to the shower center is averaged over 30 different distances ranging from 0 to 300 m, in shower coordinates. For the lateral distributions one can have antenna distances even below 20 m to the shower core. In addition, the lateral profile ranges almost always up to 150 m, and more, when the shower core is outside the antenna field.

The expected field strength ϵ^{para} from the parameterization of the cc-beam pulse height are calculated, where the distances R from the shower core was set to different values in the exponential term:

$$\epsilon^{\text{para}}(R) = 11\,(1.16 - \cos\alpha)\cos\theta \cdot \exp\frac{-R}{R_0^{\text{para}}} \cdot \left(\frac{E_{\text{p}}}{10^{17}\text{eV}}\right)^{0.95} \left[\frac{\mu\text{V}}{\text{m MHz}}\right] \qquad (5.7)$$

$R_0^{\text{para}} = 236$ m is taken from the parameterization (equation 2.18). According to this, the field strength $\epsilon^{\text{data}}R$ for the each antenna was calculated using the fit parameters (equation 5.6). The comparison of the two different estimated field strengths, for various distances $R = 0, 75, 150, 225$ m, is shown figure 5.18. In case of an agreement between data and parameterization the data points should slightly scatter around a diagonal, which can not be observed for any chosen distance. A quantification of the deviation in field strength ϵ^{data} and ϵ^{para} is given by calculating the logarithm of the ratio between them:

$$\text{deviation(R)} = \log_{10}\left(\frac{\epsilon_R^{\text{data}}}{\epsilon_R^{\text{para}}}\right) \qquad (5.8)$$

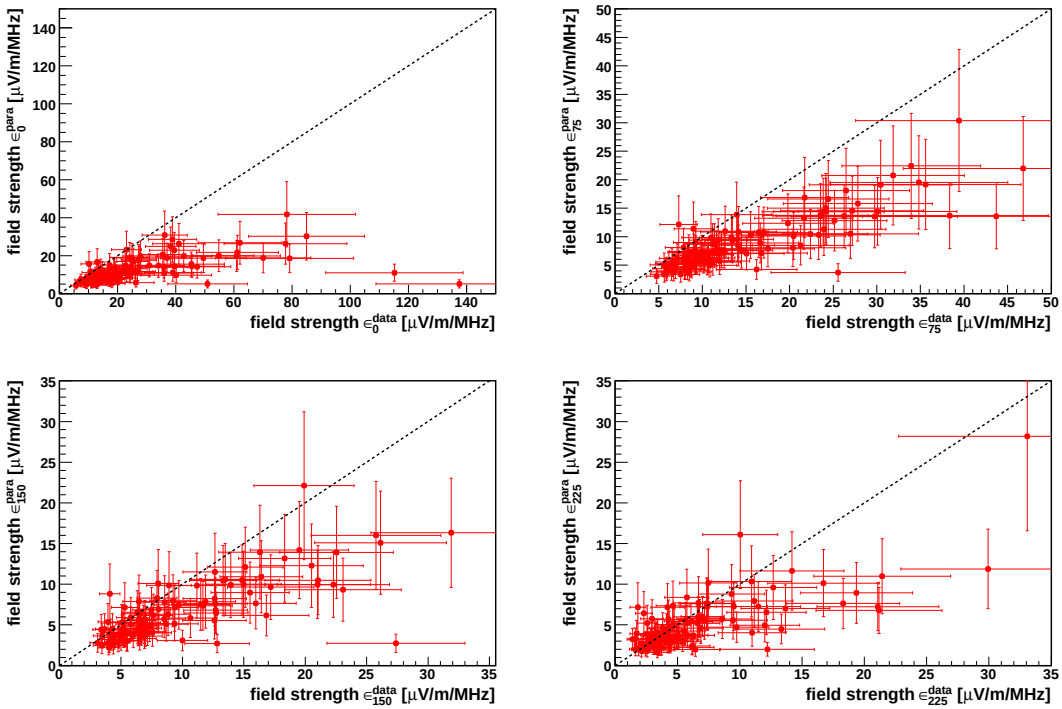

Figure 5.18: Comparison of the electric field strength ϵ at different distances $R = 0, 75, 150, 225$ m from the shower core. The diagonal represents equal values for the single antenna lateral distribution field strength ϵ^{data} and the field strength ϵ^{para} of the parameterization using the cc-beam pulse height.

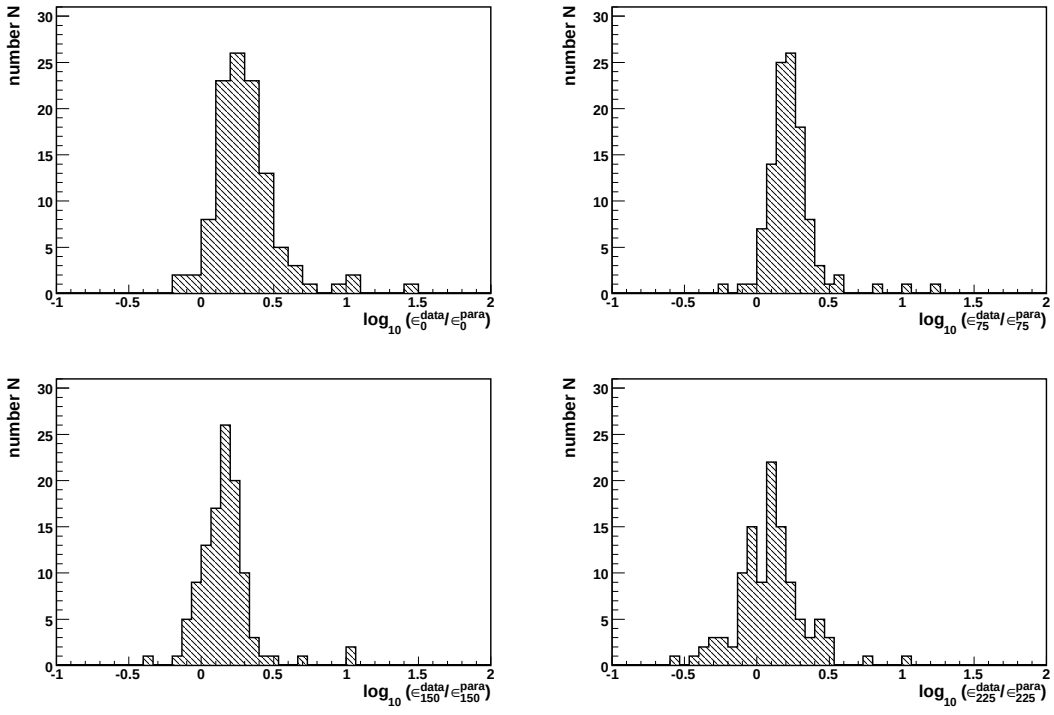

Figure 5.19: The logarithm of the ratio of the electric field strength $\epsilon^{\text{data}}/\epsilon^{\text{para}}$ at different distances $R = 0, 75, 150, 225$ m from the shower core.

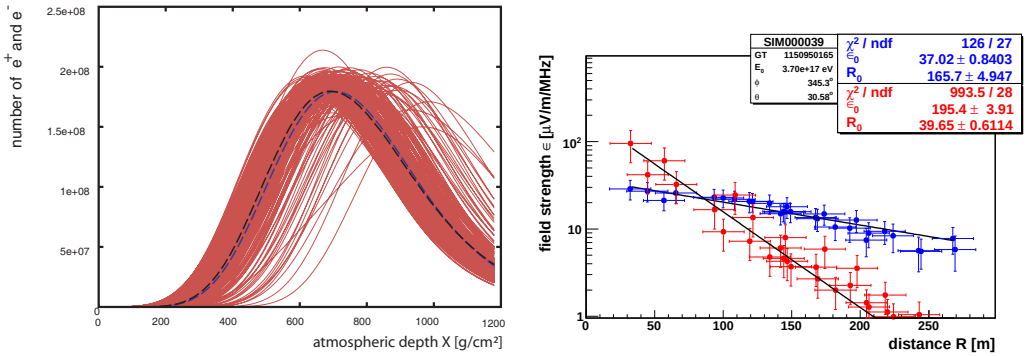

Figure 5.20: Left: 250 showers simulated with CONEX (red lines) and one representative (black line), that was used for a CORSIKA simulation (blue line). Right: Lateral distribution shown for data (blue) and simulations (red) with fits (equation 5.6).

The four panels in figure 5.19 show the obtained distributions for the calculated deviation at distances $R = 0, 75, 150, 225$ m. The field strengths ϵ_0^{data} are always below the diagonal for the chosen distance ranges and a very strong deviation at $R = 0$ m is obtained.

At a distance of $R = 225$ m, the field strength ϵ_{225} from lateral distribution and parameterization have its best relation to each other, with only 23% deviation. Whereas the values at the shower core ($R = 0$ m) differs by a factor of 2. The method of using a not upsampled cc-beam pulse height needs reasonable coherence, otherwise the absolute value is systematically decreased. In addition, an applied block averaging reduces the obtained pulse heights further. It also broadens the pulse and does not properly represent the pulse height of upsampled data. The limitation of the method for investigating lateral distributions based on single antenna signals is, that a confidential reconstruction works only for signals above background.

5.6 Comparison between Data and Simulation

Finally, the measurements of the radio emission are compared with results from Monte Carlo simulations. This is now possible, due to the performed amplitude calibration of LOPES. It is as a basic necessity in order to get the absolute scale for the field strength. Due to a new simulation strategy, using more realistic air shower models with precise, multi-dimensional histograms derived from per-shower CORSIKA simulations, a detailed comparison can now be done.

The REAS2 Monte Carlo simulation code (Huege et al. 2007c) is used to simulate the geosynchrotron radio emission for all the showers detected in the investigated data set. For each single event 250 showers were simulated with CONEX (Bergmann et al. 2007), using the same values for the shower core position, the direction and the guessed primary energy under the assumption of a proton induced shower. CONEX is a hybrid simulation code that describes the EAS development numerically, based on the solution of the corresponding cascade equations and combines this with an explicit Monte Carlo simulation of the most energetic part of an air shower.

The CONEX shower that represents the mean of all 250 simulated showers is selected (see left panel in figure 5.20). The selected shower is drawn as a black dashed line,

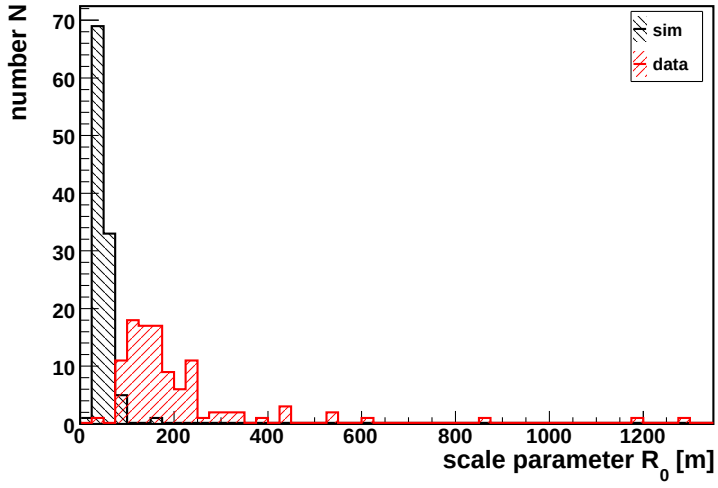

Figure 5.21: Distribution of the scale parameter R_0 obtained from measurements (red histogram) and simulations (black histogram).

whereas the full set of simulated showers with CONEX are drawn with red lines. The shower-to-shower fluctuations can be derived from the scatter of the 250 showers. The maximum of the number of electrons and positrons in the simulated shower is denoted as $X_{\max}$. The atmospheric depth X is ranging from the point of first interaction up to the observation level at ground for LOPES.

From the selected CONEX shower the particle stack after the first interaction is used as input for a full CORSIKA simulation. The result of the CORSIKA simulation should result in a shower similar to the selected one (figure 5.20, left panel, blue dashed line). CORSIKA writes out separate information for electrons and positrons sampled in several layers between the point of first interaction and the observer position. This information is used in the REAS2 code to calculate the radio emission. The output are unlimited bandwidth pulses, that are digitally filtered with a rectangle filter from 43 to 76 MHz. The field strength is calculated for the LOPES bandwidth of 33 MHz and for the known antenna positions at ground. With the input parameter of the shower direction a lateral distribution in shower coordinates is calculated. This distribution can be directly compared with the measured lateral distribution. In figure 5.20 (right) this is illustrated for one shower, showing both lateral distributions. The red data points and fit belong to the simulation result and the blue data points and fit to the measurement of the LOPES antennas. In section C are some more figures given with direct comparisons of data and simulation.

5.6.1 Comparisons of the Scale Parameter R_0

The set of 110 showers have been simulated and the lateral distribution of the radio emission calculated. The number of showers is caused by the selection process of the data sets for the lateral distributions. After applying the same fit function (equation 5.6) to both lateral distributions the scale parameter R_0 and the field strength ϵ_0 are obtained.

The comparison of the distributions of the scale parameter from measurement and simulation is shown in figure 5.21, where the red area represents the distribution

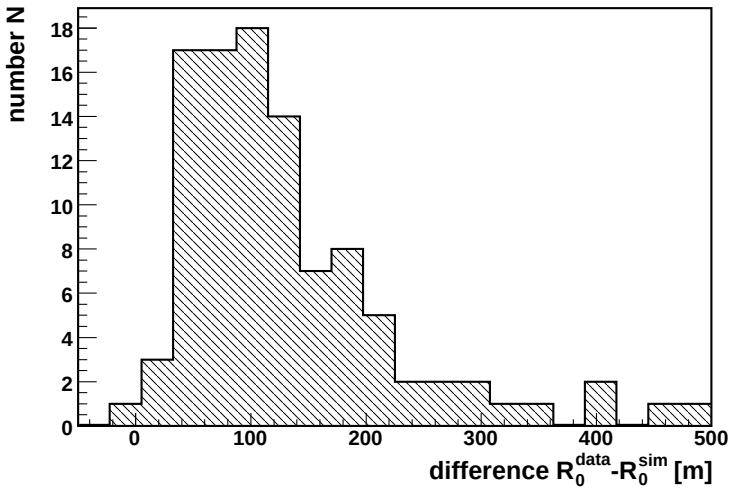

Figure 5.22: Difference of the scale parameters R_0 from data and simulations.

of the measurements and the black area the distribution of the simulations. The mean for the distribution of the scale parameter from the simulation is $R_0 = 50$ m. Such small values represent a steep lateral decrease of the field strength. The most probably value, that was obtained from measurements (section 5.4.3) is ≈ 125 m and the mean values of the distribution is higher.

The differences for the scale parameters (R_0^{data}-R_0^{sim}) for each single shower is calculated and displayed in figure 5.22. The lateral distributions of the measurements are systematically flatter, compared to the shape in simulations and give a mean difference of about 75 m. The showers observed with very flat lateral distributions show a much larger discrepancy, as such flat distribution never occur in the simulations.

Large scale parameters allow us to measure the same field strength at larger distances from the shower core, which will be helpful for large scale applications of the radio detection technique.

5.6.2 Comparison of the Field Strength ϵ

The second free parameter from the fit function (equation 5.6) is the field strength ϵ_0. For the measurements and the simulations this second parameter is obtained independently, but using the same shower. Now one can make use of the fit function and calculates the field strengths ϵ_R^{data} and ϵ_R^{sim} at a distance R. The resulting field strength ϵ_R can be compared in the same way as in case of the parameterized field strength.

The distances $R = 0, 75, 150, 225$ m were chosen to calculate the corresponding field strengths ϵ_R^{data} and ϵ_R^{sim}, that are shown in figure 5.23. The diagonals represent equal values for the field strengths calculated from simulation and from measurements. The investigations of the scale parameter R_0 have shown, that the measurements give much larger values. This therefore results in lower field strengths ϵ_0^{data} at the shower core, (figure 5.23, upper left). For the field strength ϵ_{75} the results from measurement and simulation are very similar in size and scatter only slightly around the diagonal. This correlation is less strong for a distance of $R = 150$ m, but still

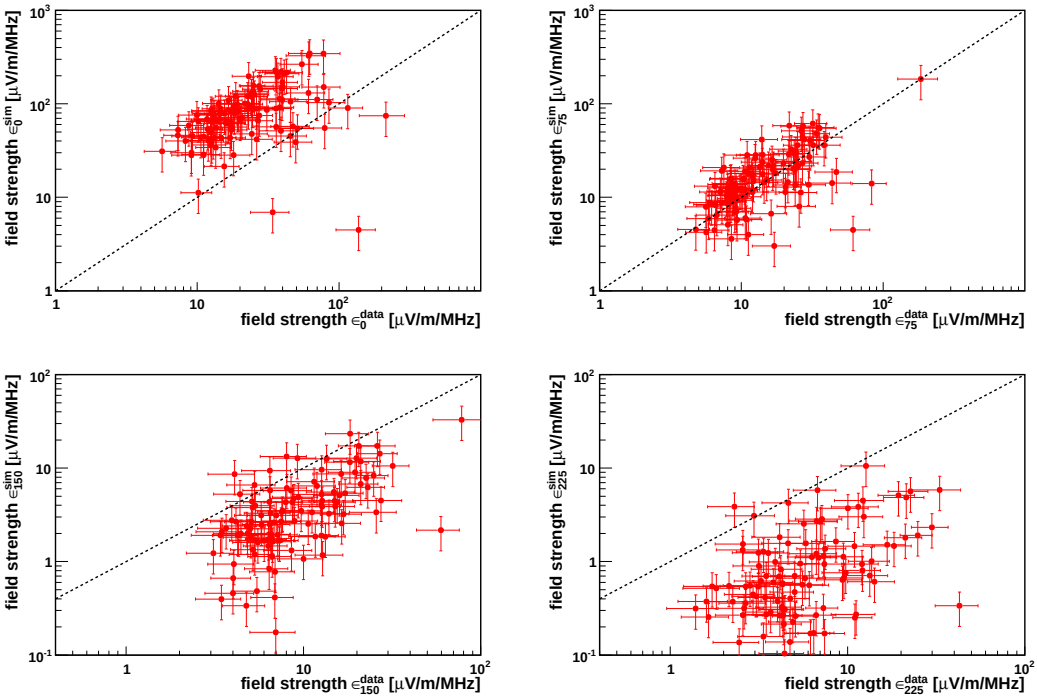

Figure 5.23: Correlations ϵ_R^{data} obtained from measurements and ϵ_R^{sim} obtained from simulation for different distances $R = 0, 75, 150, 225$ m to the shower center. The diagonal is representing equal values from simulation and measurement.

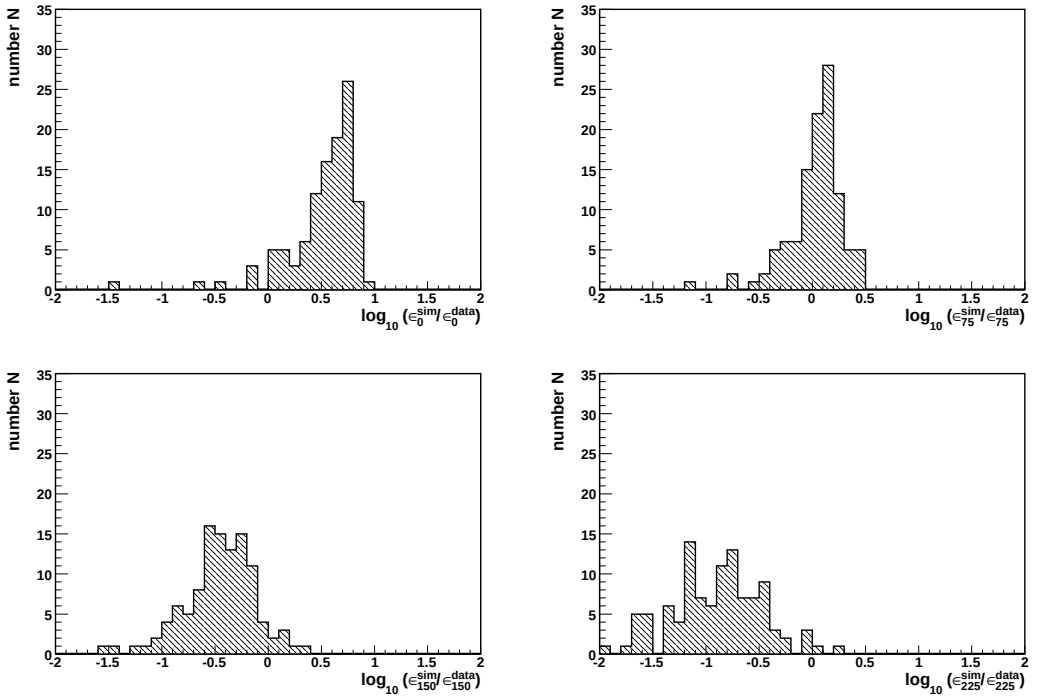

Figure 5.24: The logarithm of the ratio of the electric field strength $\epsilon^{\text{sim}}/\epsilon^{\text{data}}$ at different distances $R = 0, 75, 150, 225$ m from the shower core.

sufficient. The data points for the field strength ϵ_{225} are almost always below the diagonal, which is due to the fact that the scale parameter R_0 in the simulations is smaller. Hence, the lateral distribution obtained from simulations gives very low values at larger distances. The lateral distributions of the measurements with larger scale parameter R_0 give significantly higher field strengths for this distance.

Using equation 5.8 the logarithmic deviation $\log_{10}(\epsilon_R^{\mathrm{sim}}/\epsilon_R^{\mathrm{data}})$ at different distances R from the shower can be investigated. In figure 5.24 the histograms of the deviation at distances $R = 0$, 75, 150, and 225 m are shown. That the deviation for measurement and simulation is $\log_{10}(\epsilon_{225}^{\mathrm{sim}}/\epsilon_{225}^{\mathrm{data}}) = -0.89$ for the distance $R = 225$ m (figure 5.24, lower right), could be already seen in figure 5.23, lower right. For $R = 0, 150$ m the distributions reveal a systematic difference of factor ≈ 5.

For the distance $R = 75$ m the spread of the values is the smallest and the mean values deviate only about 10%. This is a very promising result, as a detailed comparison between measurements and simulations was performed for the first time with LOPES data. Nevertheless, there are differences between measurements and simulations outside this distance range, due to the difference of roughly factor 2 in the scaling parameter.

5.7 Summary of the Lateral Distribution Measurements

For the analysis of lateral distributions of the EAS radio emission a data set of showers was selected, which is amplitude calibrated. The developed method uses upsampled signals from individual antennas to derive the electric field strength ϵ. With help of the reconstructed shower parameters from KASCADE-Grande the lateral distribution of the radio signal in EAS for individual events is obtained.

Scale Parameter R_0
The equation 5.6 describes the measured field strength and contains two free parameters, where the scale parameter R_0 describes the lateral profile. For 110 showers, which have large enough radio signal in all antennas, i.e. the radio signal is well above background, correlations with global shower parameters, like direction and energy were studied.

From the distribution of the scale parameter (figure 5.14) one derives, that the scale parameter peaks at $R_0 \approx 125$ m and has a mean value of $R_0 = 237$ m for the detected events. Here, the distribution comprises showers with an expected exponential decay as well as events with a very flat lateral distribution.

Comparing the obtained scale parameter with that one got by a parameterization of LOPES showers measured at lower energies (equation 2.18), we conclude that there is agreement between these values. Including the tail of the distribution in figure 5.14 the mean value agrees with the cc-beam based scale parameter in the parameterization of Horneffer et al. (2007), whereas an exclusion of the tail obtains a scale parameter that agrees with the parameterization of Allan (1971).

The found lateral distributions with very flat lateral profiles (examples shown in figure 5.13) are remarkably and require further investigations and more statistics. The fact that the lateral distribution becomes flat towards the shower center, or

more extreme, is flat over the whole observable distance range, can not be simply explained with instrumental effects.

Comparison with Parameterization
The existing parameterizations can also be used for a direct comparison of the field strength ϵ. In particular, the parameterization based on LOPES data was investigated and for distances $R = 0, 75, 150, 225$ m the corresponding field strengths ϵ_R^{data} and ϵ_R^{para} where calculated. The comparisons revealed (figure 5.18), that the two methods give comparable results for the intermediate distant range. The two methods gain different values at the shower center and at large distances. This is attributed to the calculation of the cc-beam pulse height, where a lack of coherence and an applied block averaging can systematically decrease this field strength. The single antenna lateral distributions describe the lateral profile much better and therefore the field strength at the shower center is determined more reliable.

Comparison with Simulations
A very important comparison for the understanding of the radio emission observed in EAS, the geosynchrotron radiation, was performed with detailed Monte Carlo simulations on an event-to-event basis. This was done for a sub-set of the investigated showers. The simulations used the known shower parameters, like core, direction and energy, to calculate the bandwidth normalized field strength for each LOPES antenna. This allows to compare measurements and simulations one-to-one.

In general the measurements gives less steep lateral distributions, i.e. larger scale parameters R_0 and the deviation is in the order of 75 m (figure 5.22). In addition, it was derived that the differences between measurements and simulations can be very large and that the unexpected very flat lateral profiles are never reproduced in simulations. In order to understand the underlying systematic effects significantly more statistics is needed.

The deviation in the scale parameters enters in systematically lower field strengths ϵ_0^{data}, compared to the field strengths ϵ_0^{sim} obtained from simulations at the shower center. The difference is a factor of three at the shower center. On the other hand we obtained at $R = 75$ m a fairly good agreement between simulations and measurements. This is a promising result at all, as such comparisons are performed for the first time for LOPES data.

6. Summary and Outlook

The present work is based on coincidence measurements of the LOPES radio antenna array and the air shower experiment KASCADE-Grande. This is a unique combination of two different detection techniques for EAS investigations. Furthermore, the obtained data of both experiments are well calibrated and can therefore be used to compare in detail the properties of the radio emission with EAS parameters. In the frame of this thesis a calibrated data set of showers was analyzed to study the lateral distribution of the radio emission in individual air showers and compare the results with the results of a parameterization of earlier LOPES data or with dedicated Monte Carlo simulations.

The LOPES experiment is a radio antenna array set up at the Forschungszentrum Karlsruhe. With thirty inverted V-shaped dipole antennas radio signals can be measured in the frequency range from 40 MHz up to 80 MHz. The location of the KASCADE-Grande air shower experiment was chosen in order to measure in coincidence many EAS parameters. The aim of the measurements of LOPES is to investigate the origin and the properties of the radio emission in EAS, which is known since the late 1960's (Jelley et al. 1965). After a period without new experiments and measurements the detection technique experienced a renaissance.

In 2003 the LOPES experiment started to measure the radio emission from EAS and after an initial setup of ten antennas (LOPES10) in 2005 an extension to thirty antennas was accomplished (LOPES30). The configuration of LOPES has changed several times according to the scientific questions to be answered, but the operation and calibration of the antennas was ensured for the complete period.

The calibration of the detector is for any experiment a requirement to translate the measured values into a physical quantity. Therefore, one part of this thesis was to perform an **amplitude calibration** that was missing for the LOPES10 configuration. The developed method uses a commercial reference source to quantify the input power and to compare this with the power that is recorded per individual electronic channel. During the entire operation time of the LOPES30 antenna array calibration campaigns were performed to monitor the system health and performance. The characteristic quantity is the so-called amplification factor $V(\nu)$, which is studied

extensively (Nehls et al. 2008). Especially the influence of the antenna gain calculations was a major subject. The systematic uncertainties from several possible sources were investigated and a systematic uncertainty of $\sigma_V/V = 20.5\%$ was obtained for the calibration procedure, not including the uncertainty of the reference source.

The amplitude calibration allow to calculate the magnitude of the electric field strength ϵ that is measured by the antenna. For the operation time from end of 2005 until end of 2006 a data set with 860.000 files was recorded, with antennas oriented in east-west direction. For this data set the reconstructed shower parameters are provided from the KASCADE-Grande measurements. Using this data set, radio signal candidates were selected and the radio pulses reconstructed after some quality cuts. Finally, for 110 high energy radio events the lateral distribution on an event-to-event and antenna-to-antenna basis was studied. Compared to the total number of triggered showers this is a very small fraction, but the present RFI situation at the LOPES location does not sufficiently allow the detection of low energy events. On the other hand, the coincidence measurements at the KASCADE-Grande location allow to perform direct comparisons between the different measurement techniques. Future experiments will certainly be able to chose a more radio quiet environment.

The investigation of properties of the radio emission in EAS can be performed in different ways. The **lateral distribution** is reconstructed from the radio signals in individual antennas, which is performed for the first time for LOPES data. To derive the lateral distributions using individual antennas an upsampling of the raw data via zero-padding was performed. From the restored signal shape in the upsampled data the height of the radio pulse is determined. Using these radio pulse heights the lateral distribution is reconstructed. Here, the uncertainty of the amplitude calibration and an antenna-by-antenna event-by-event background calculation enters in the uncertainty of the determined field strength ϵ. The uncertainty of the reconstructed geometry of the shower contributes to the uncertainty for the lateral distance R of each antenna. The applied fit function that is used (equation 5.6) has two free parameters, the field strength ϵ_0 at a distance of $R = 0$ m, and the scale parameter R_0.

The scale parameter R_0 is a quantity that describes the lateral profile. The found scale parameter distribution shows a most probable value of $R_0 \approx 125$ m and has a mean value of $R_0 = 237$ m. No direct evidence for a dependence on shower parameters like direction, geomagnetic angle, or primary energy could be found. This indicates that the lateral profile is an intrinsic property of the radio emission and the shower development. Comparing the obtained scale parameter with published values of earlier experiments a good agreement is found.

Studying the lateral distributions, there have been showers detected that show a **very flat lateral distribution** or become flat towards the shower center. They compose the tail of the distribution for the scaling parameter R_0. Presently there are too few showers to derive any correlation with specific shower parameters. Hence, the result is an indication, that significantly more data are needed for more detailed investigations.

Measurements of the radio emission in EAS were used to parameterize the dependence of the field strength ϵ with shower observables, e.g. performed by Horneffer et al.

(2007). The results of the lateral distribution investigations can be compared with these parameterizations. The field strength ϵ_0^{data} at the shower core obtained from lateral distributions is **systematically higher** than the field strength for the parameterization based on LOPES data (equation 2.18). A lack of coherence and an applied block averaging can systematically decrease the field strength ϵ_0^{para}, which is as well not upsampled. The method used for this thesis is a significant improvement in describing the lateral behavior of the radio emission. For a distance of $R = 150$ m the deviation in the field strength becomes smaller, but gives still no full agreement.

The measurements of the radio emission in EAS were historically triggered by models predicting short radio pulses (Askar'yan 1962, 1965). Since some time detailed air shower Monte Carlo simulations are used to calculate the geosynchrotron radio emission (Huege et al. 2007c). For a sub-set of the investigated showers these simulation were carried out, using the corresponding shower parameters. Output of these detailed simulations is the bandwidth normalized field strength for each LOPES antenna position per individual event. This work presents the **first one-to-one comparison** of measurements and simulations for the LOPES experiment. It is known that, due to the LOPES antenna geometry, not only the dominant east-west polarization is received, but also contributions from the vertical enters in the antenna. Nevertheless, the effects will be much more important for large zenith angles, which are not investigated in the present work.

The result of the performed comparison is, that the simulations predict a much **steeper lateral profile** than the measurements show up. The difference of both scale parameters is about 100 m and even larger for the showers with flat distributions (high R_0). The presence of flat distributions in the data is unexpected from the simulations and not present in the simulated radio emission.

Comparisons of the field strength ϵ at different distances have shown, that the absolute scale of simulations and measurements are in good agreement at a distance of $R = 75$ m. This result is a further indication for the **geosynchrotron mechanism** for the radio emission observed in EAS. However, due to the predictions of steeper lateral distributions in the simulations, there are significant differences in the field strength close to the shower core and at large distances. Considering in addition the possible flattening of the lateral distribution close to the center of the shower, we conclude that the simulations do not adequately describe the lateral shape, but the absolute scale is in reasonable agreement.

The studies in the frame of this thesis have shown that the radio detection technique experience a renaissance. The gap in knowledge between parameterizations, simulations and measurements became closer. Nevertheless, due to the improved accuracy of the measurements new questions arise, in particular on the role of the polarization in the radio emission and on the properties of flat lateral profiles. However, the LOPES experiment has shown once again its potential for investigating the properties of the radio emission in EAS.

A. Amplification Values of All Calibration Measurements

For all antennas the result of the individual calibration campaigns and the mean values are given. The numbers in the boxes give the date of the campaigns. If there was a change of the antenna in the polarization direction, it is also indicated.

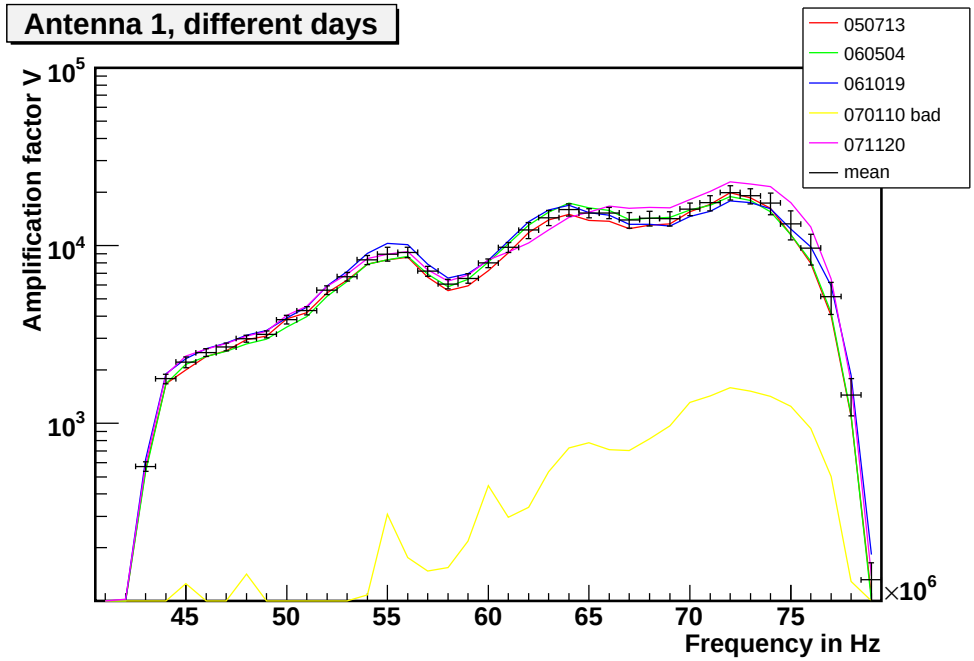

Figure A.1: Amplification factors of antenna #1 from calibration measurements.
070110 - wrong polarization measured.
070124 - EW -> NS.

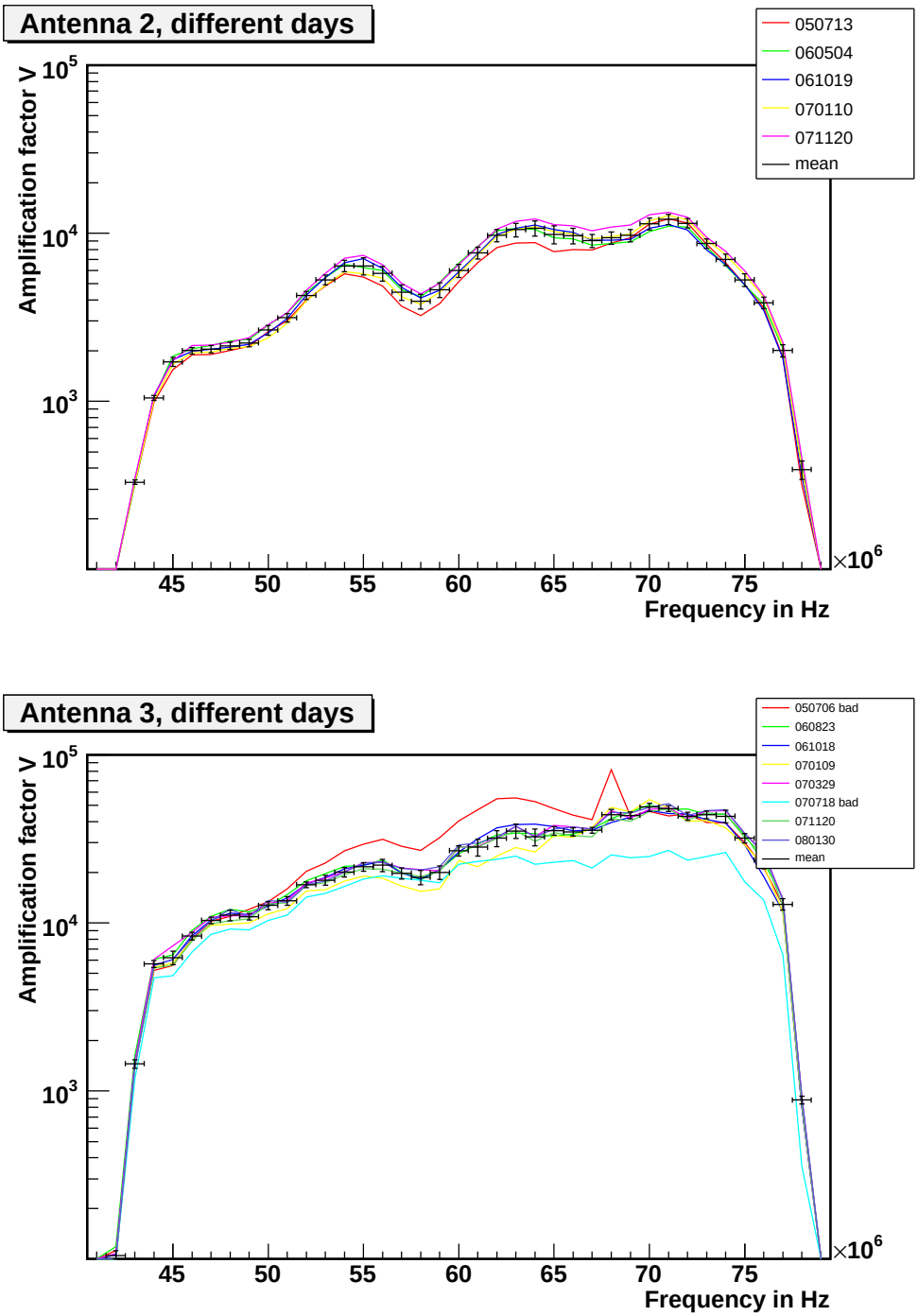

Figure A.2: Up: Amplification factors of antenna #2 from calibration measurements. Low: Amplification factors of antenna #3 from calibration measurements.
050706 - bad measurement.
070718 - bad - wrong distance at last measurement.
061208 - EW -> NS.

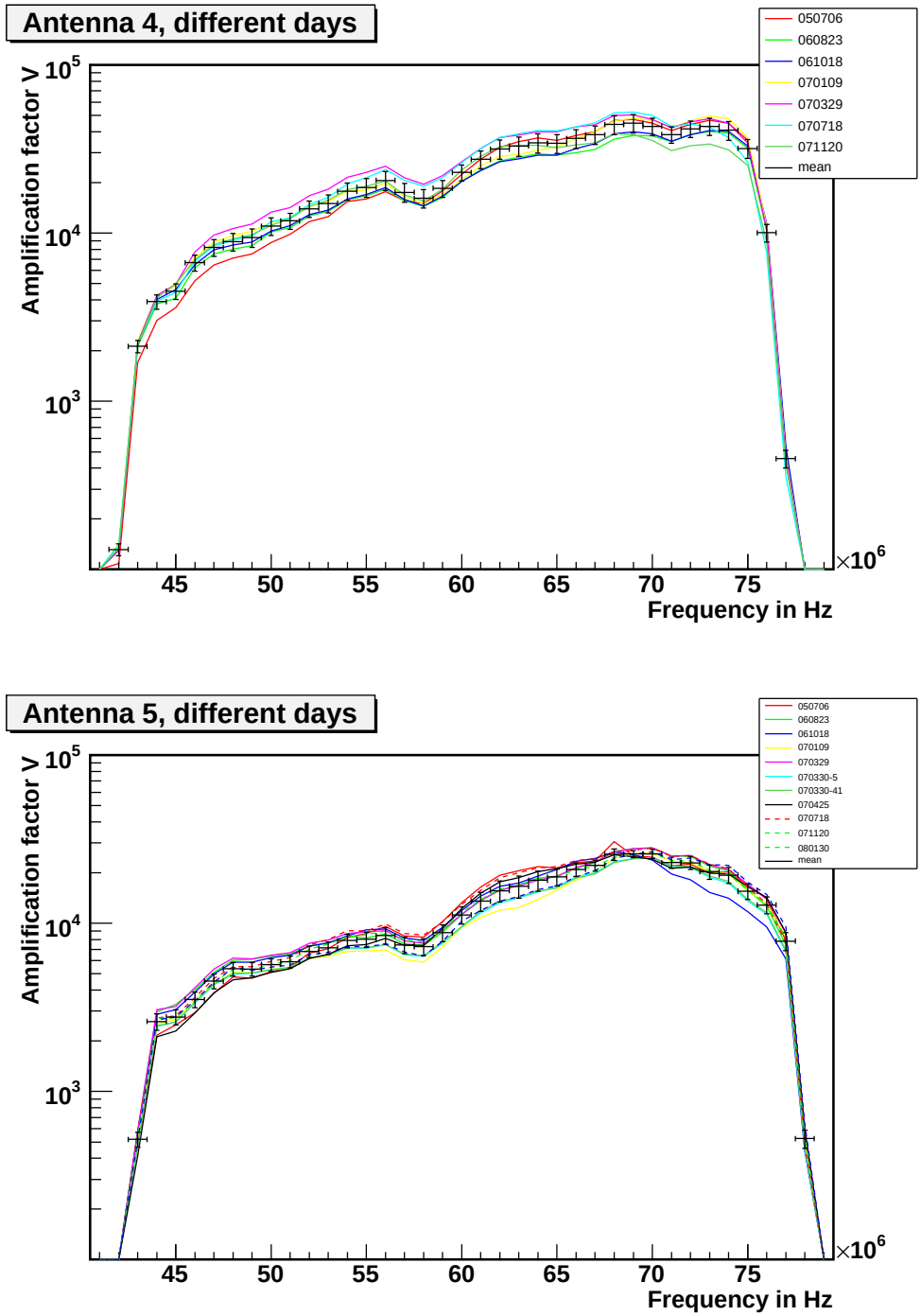

Figure A.3: Up: Amplification factors of antenna #4 from calibration measurements. 48 MHz interpolated.
Low: Amplification factors of antenna #5 from calibration measurements. 50 MHz interpolated.

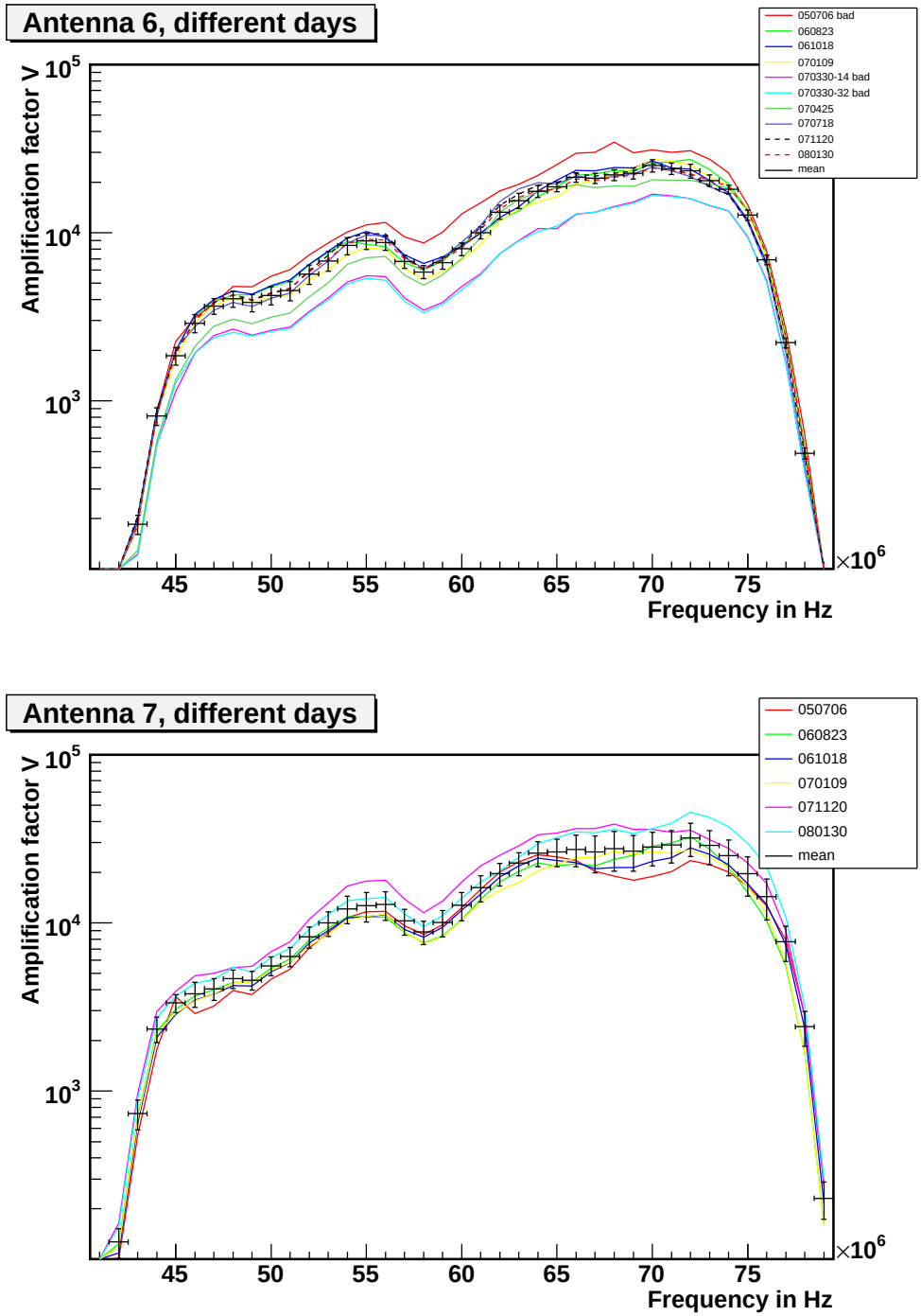

Figure A.4: Up: Amplification factors of antenna #6 from calibration measurements.
50 MHz interpolated.
050706 - bad measurement
070330-x - bad measurement
061208 - mounted as NS polarization at antenna #5.
Low: Amplification factors of antenna #7 from calibration measurements.
50 MHz interpolated.
060812 - EW -> NS.
070427 - delay measurements, larger amplification factors now.

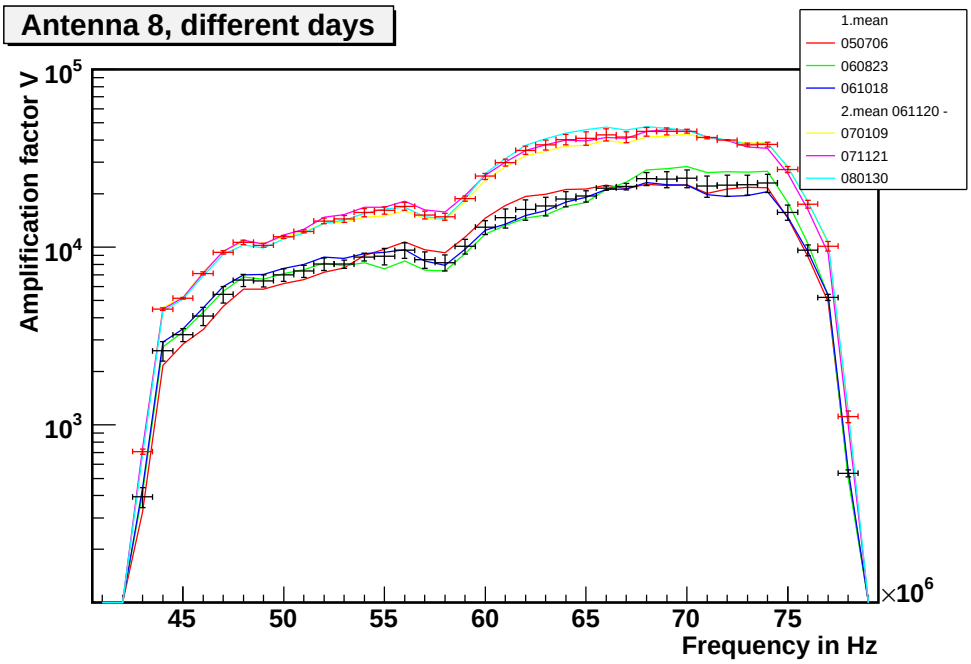

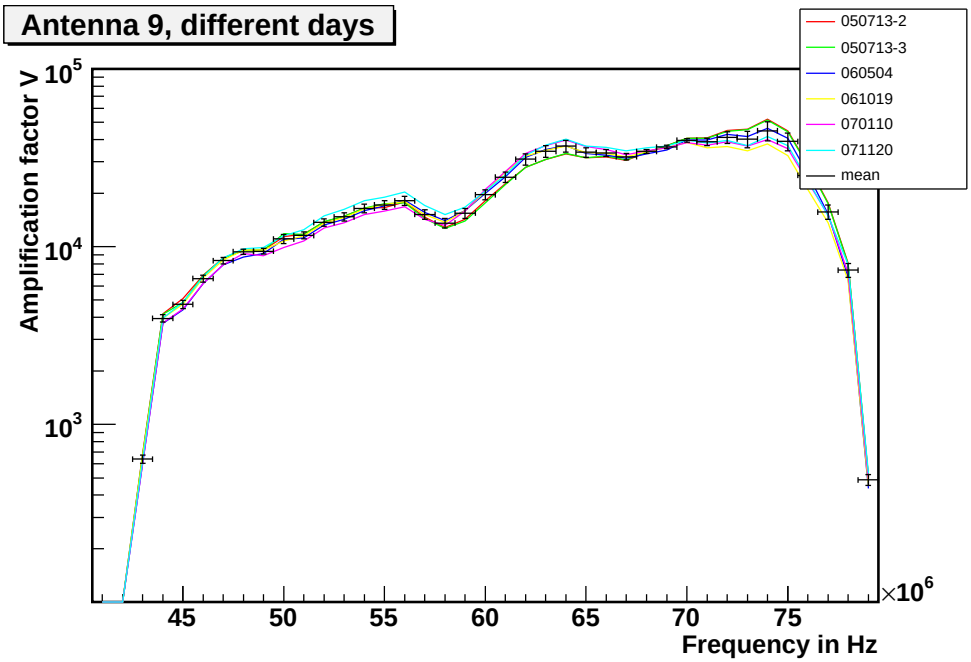

Figure A.5: Up: Amplification factors of antenna #8 from calibration measurements.
50 MHz interpolated.
2 amplification factors!
061120 - LNA test measurements, larger amplification factor now.
Low: Amplification factors of antenna #9 from calibration measurements.

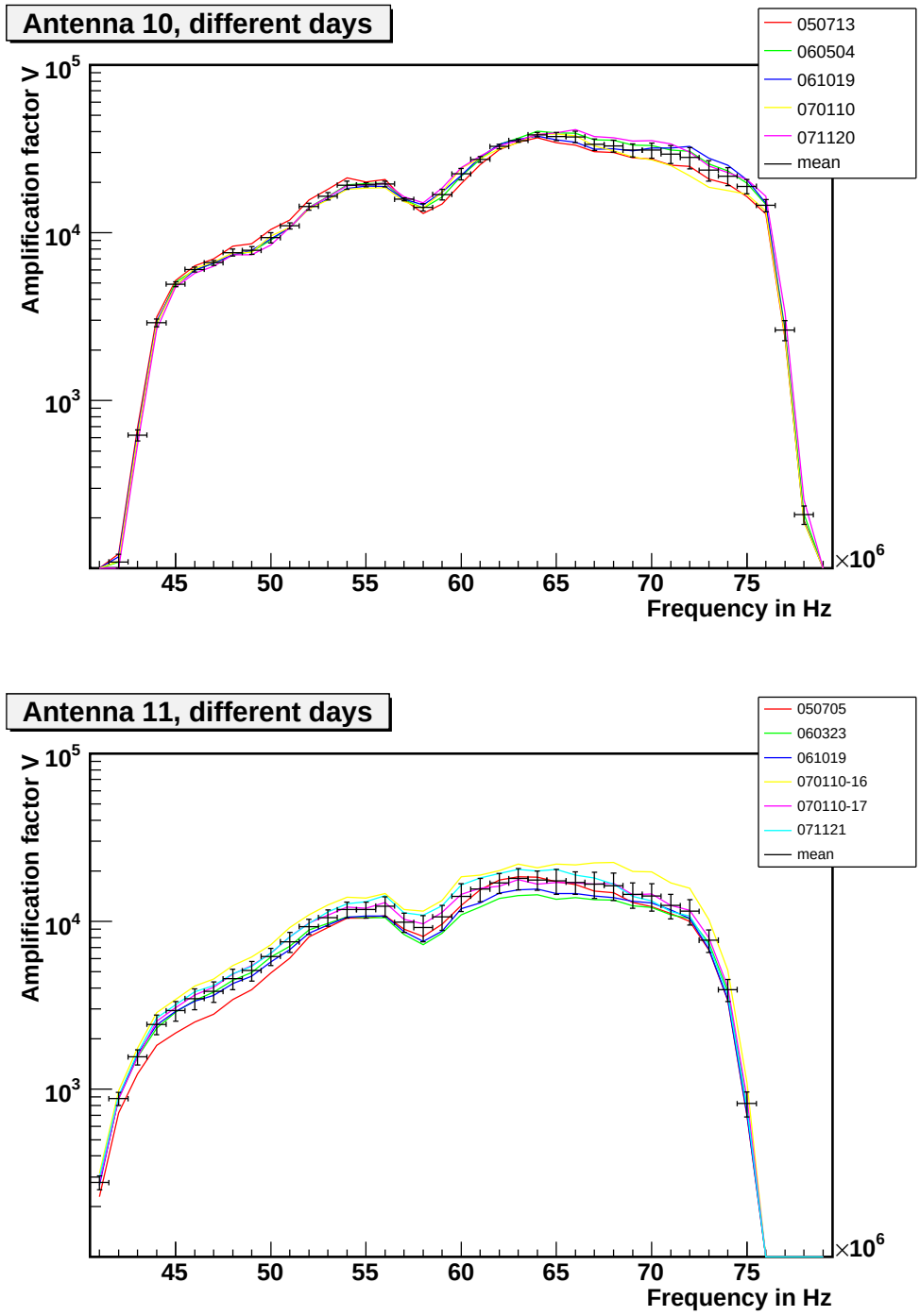

Figure A.6: Up: Amplification factors of antenna #10 from calibration measurements.
061208 - EW -> NS.
Low: Amplification factors of antenna #11 from calibration measurements.
48 MHz interpolated.
061208 - EW -> NS.

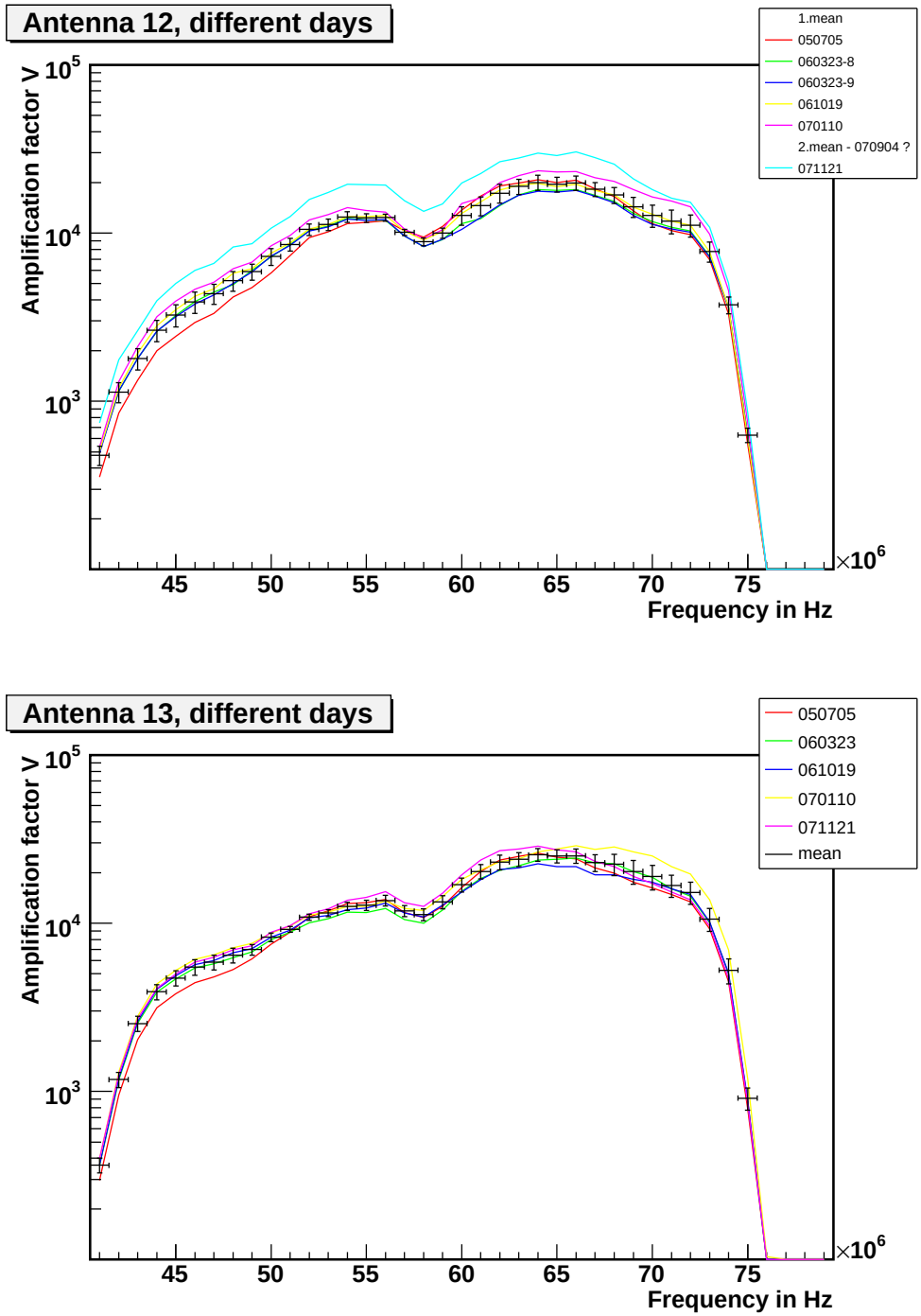

Figure A.7: Up: Amplification factors of antenna #12 from calibration measurements.
070904 - delay measurements, larger amplification factor now.
Low: Amplification factors of antenna #13 from calibration measurements.

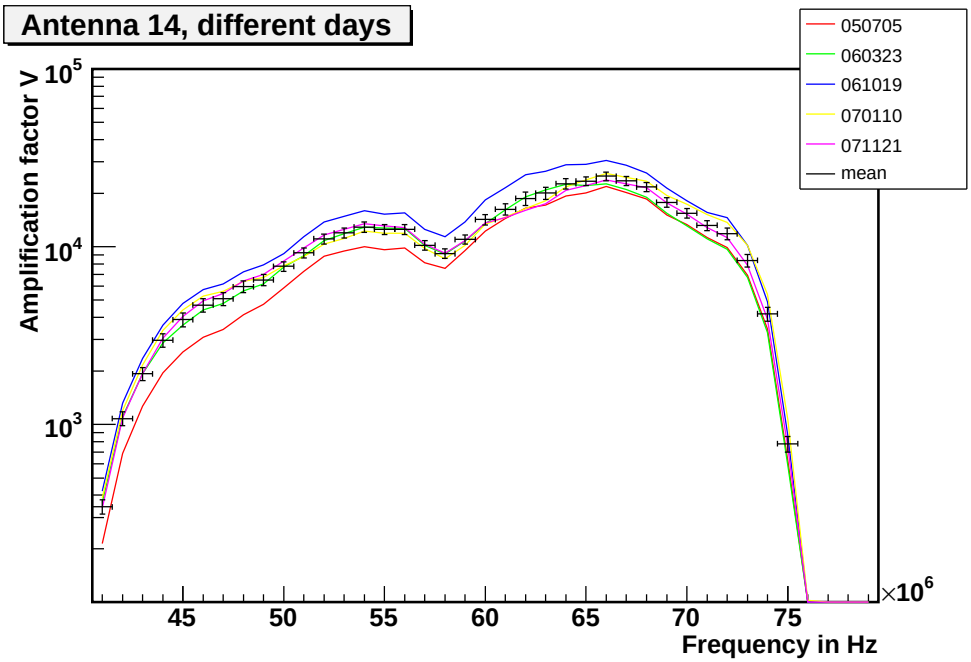

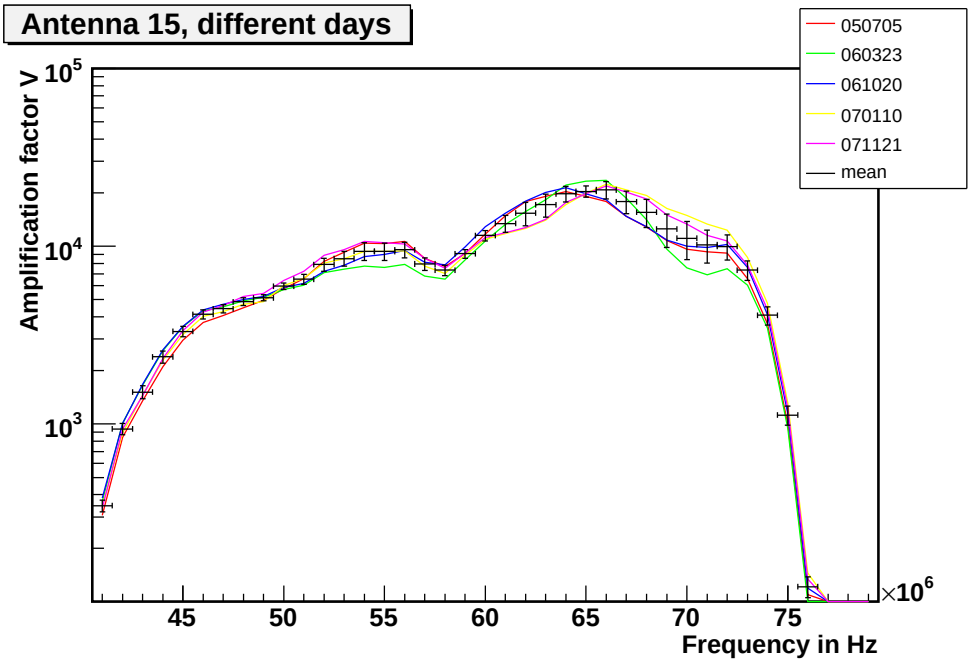

Figure A.8: Up: Amplification factors of antenna #14 from calibration measurements.
061208 - EW -> NS.
Low: Amplification factors of antenna #15 from calibration measurements.
061208 - EW -> NS.

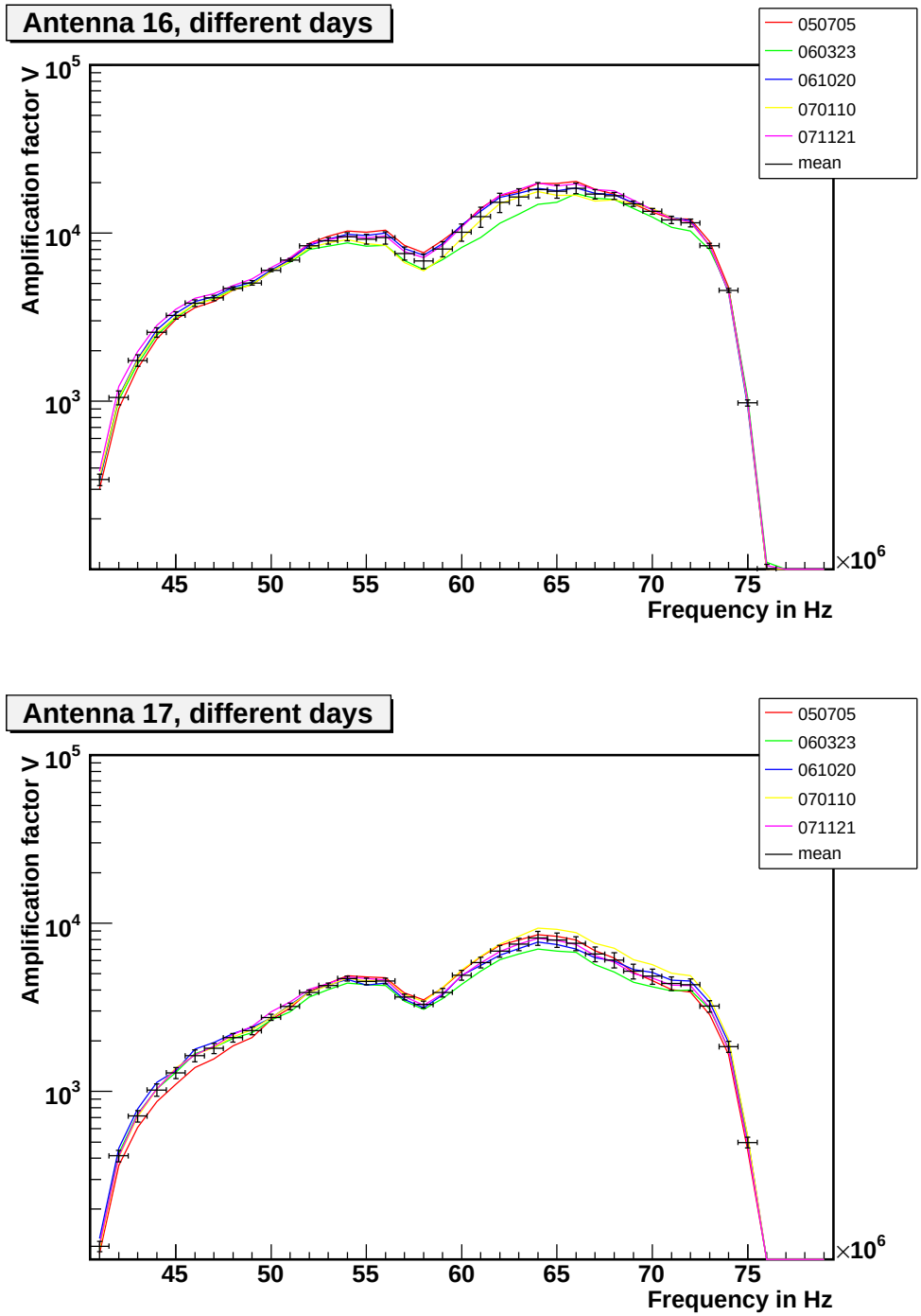

Figure A.9: Up: Amplification factors of antenna #16 from calibration measurements.
Low: Amplification factors of antenna #17 from calibration measurements.
48 MHz interpolated.

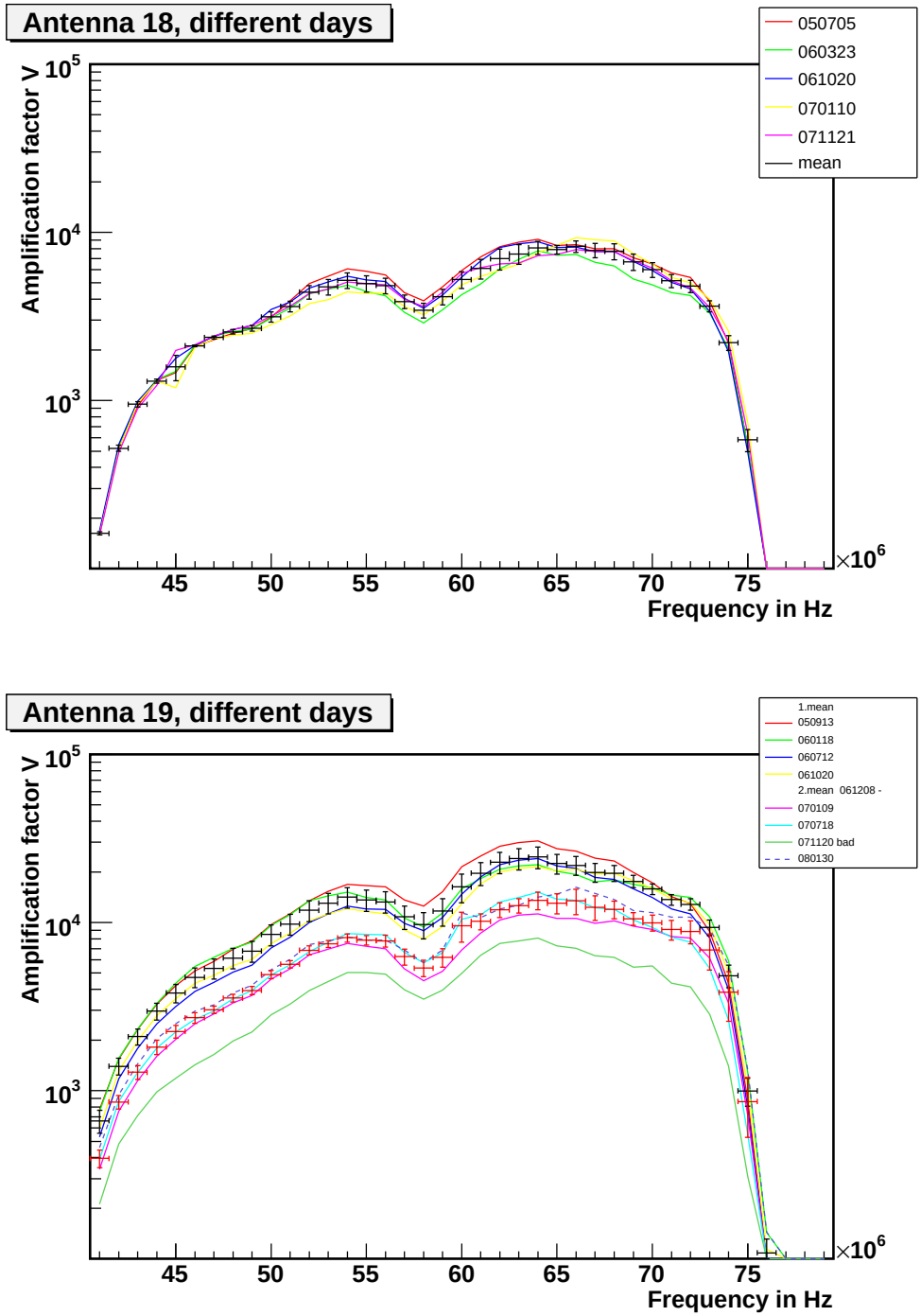

Figure A.10: Up: Amplification factors of antenna #18 from calibration measurements.
48 MHz interpolated.
061208 - EW -> NS.
Low: Amplification factors of antenna #19 from calibration measurements.
48 MHz and 50 MHz interpolated.
2 amplification factors!
061208 - dual polarized antenna - lower amplification factor now.
070914 - delay measurements, amplifier damaged, lower amplification factor! BAD period.
080117 - amplifier exchanged. BAD period ends.

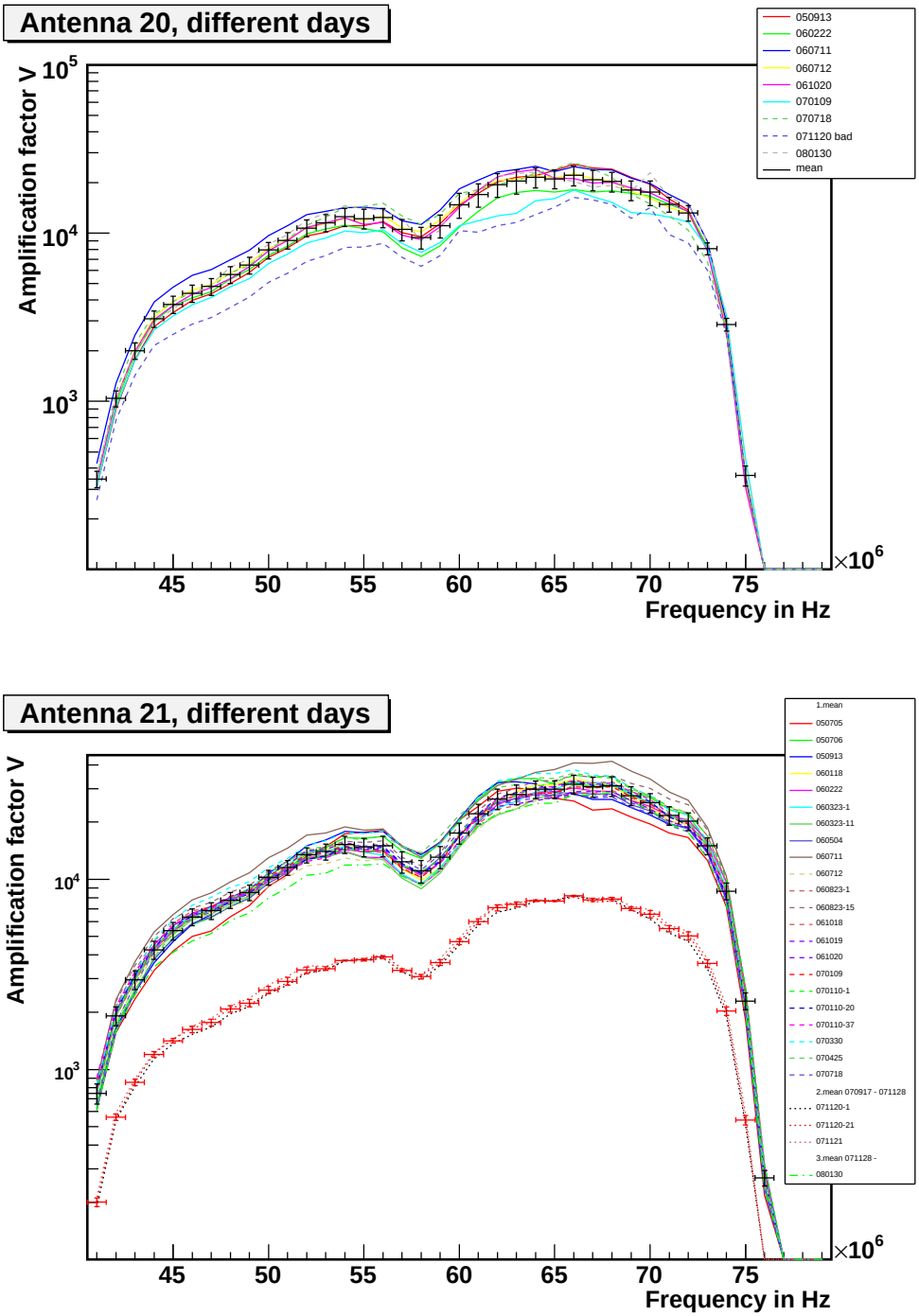

Figure A.11: Up: Amplification factors of antenna #20 from calibration measurements.
50 MHz interpolated.
061208 - mounted as NS polarization at antenna #19.
071120 - delay measurements, amplifier damaged, lower amplification factor! BAD period.
071128 - amplifier exchanged. BAD period ends. Low: Amplification factors of antenna #21 from calibration measurements.
50 MHz interpolated.
2 amplification factors!
070917 - delay measurements, lower amplification factor!
071128 - amplifier exchanged, higher amplification factor.

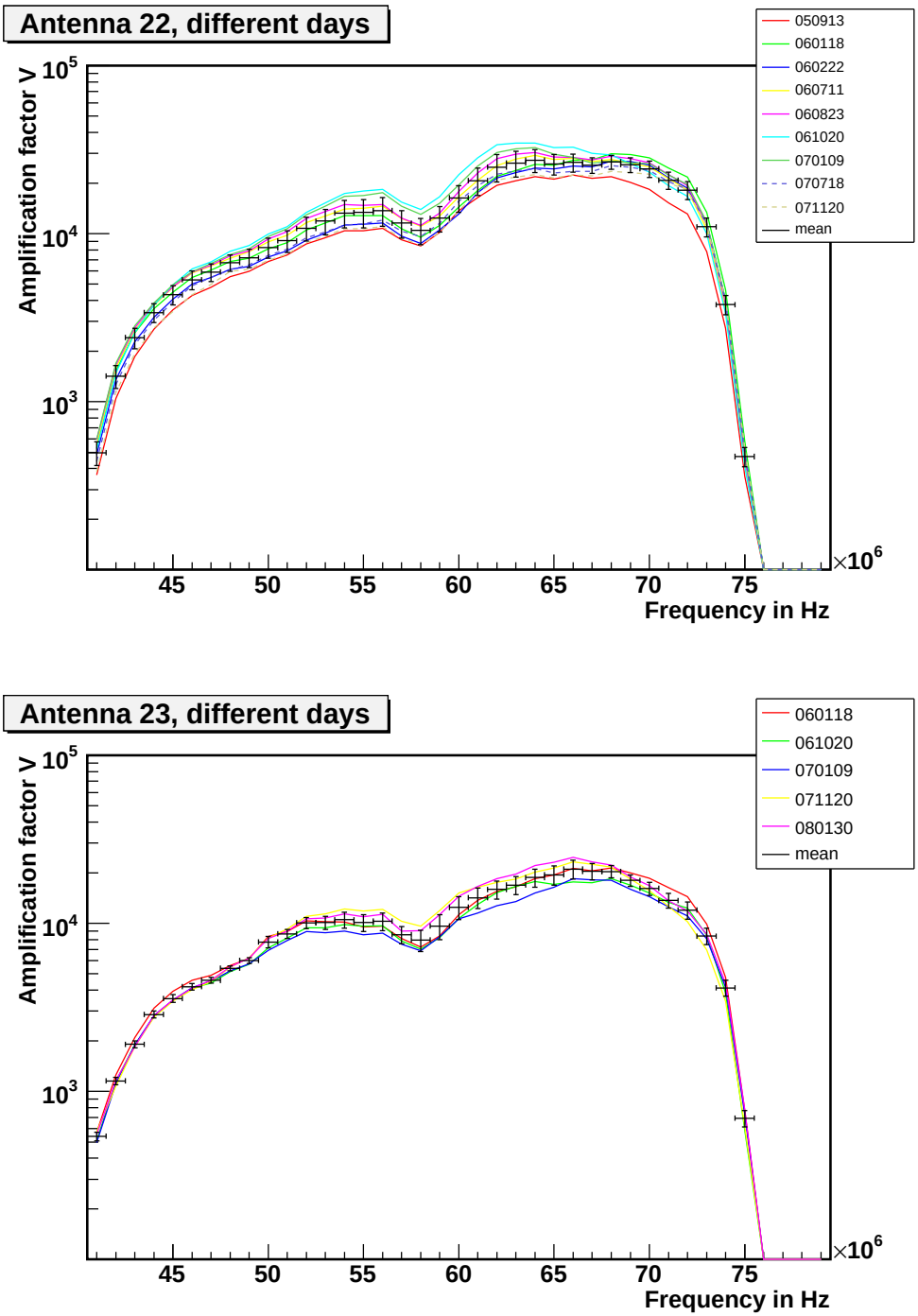

Figure A.12: Up: Amplification factors of antenna #22 from calibration measurements.
50 MHz interpolated.
Low: Amplification factors of antenna #23 from calibration measurements.
48 MHz interpolated.

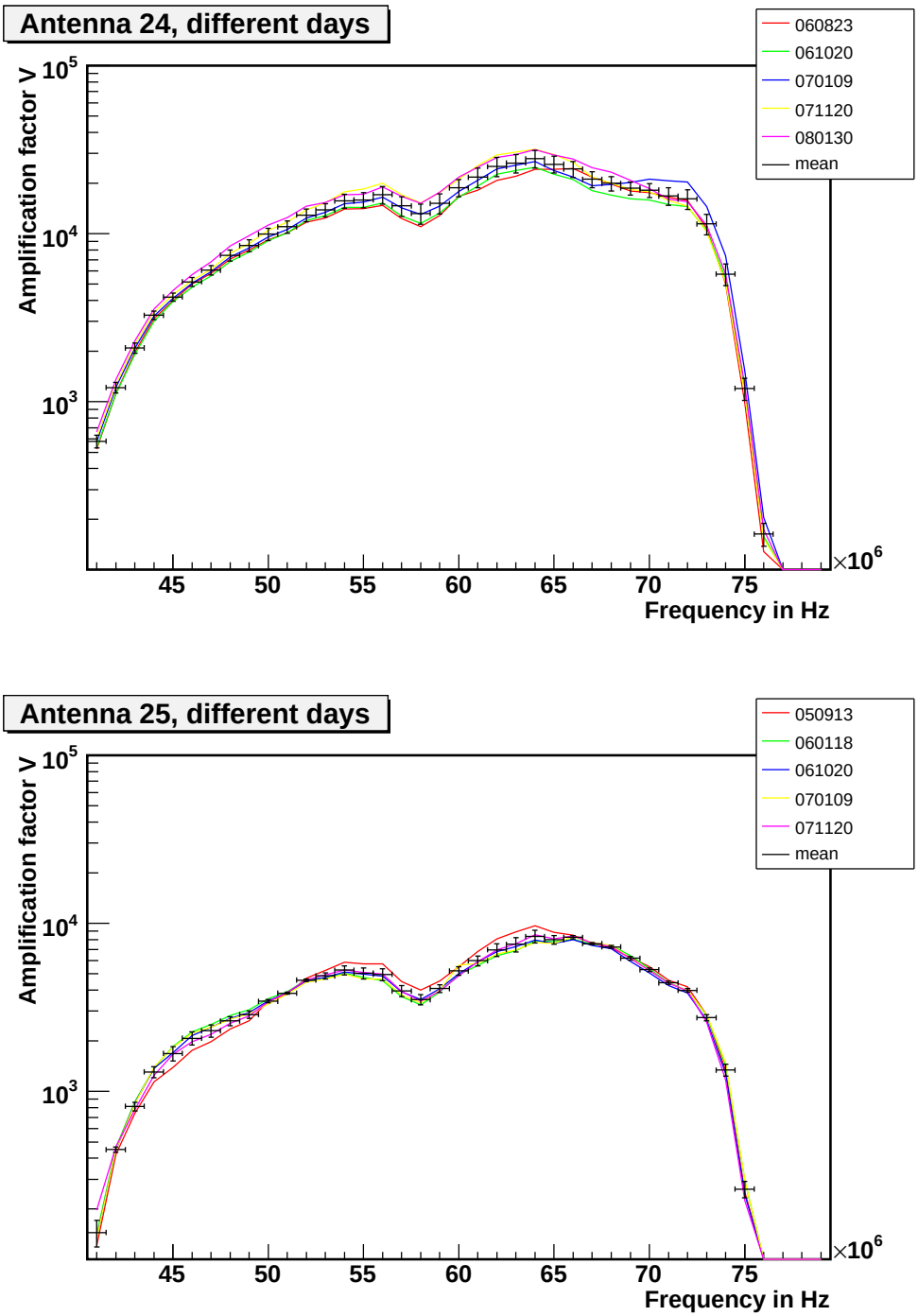

Figure A.13: Up: Amplification factors of antenna #24 from calibration measurements.
48 MHz and 50 MHz interpolated.
Low: Amplification factors of antenna #25 from calibration measurements.
48 MHz interpolated.

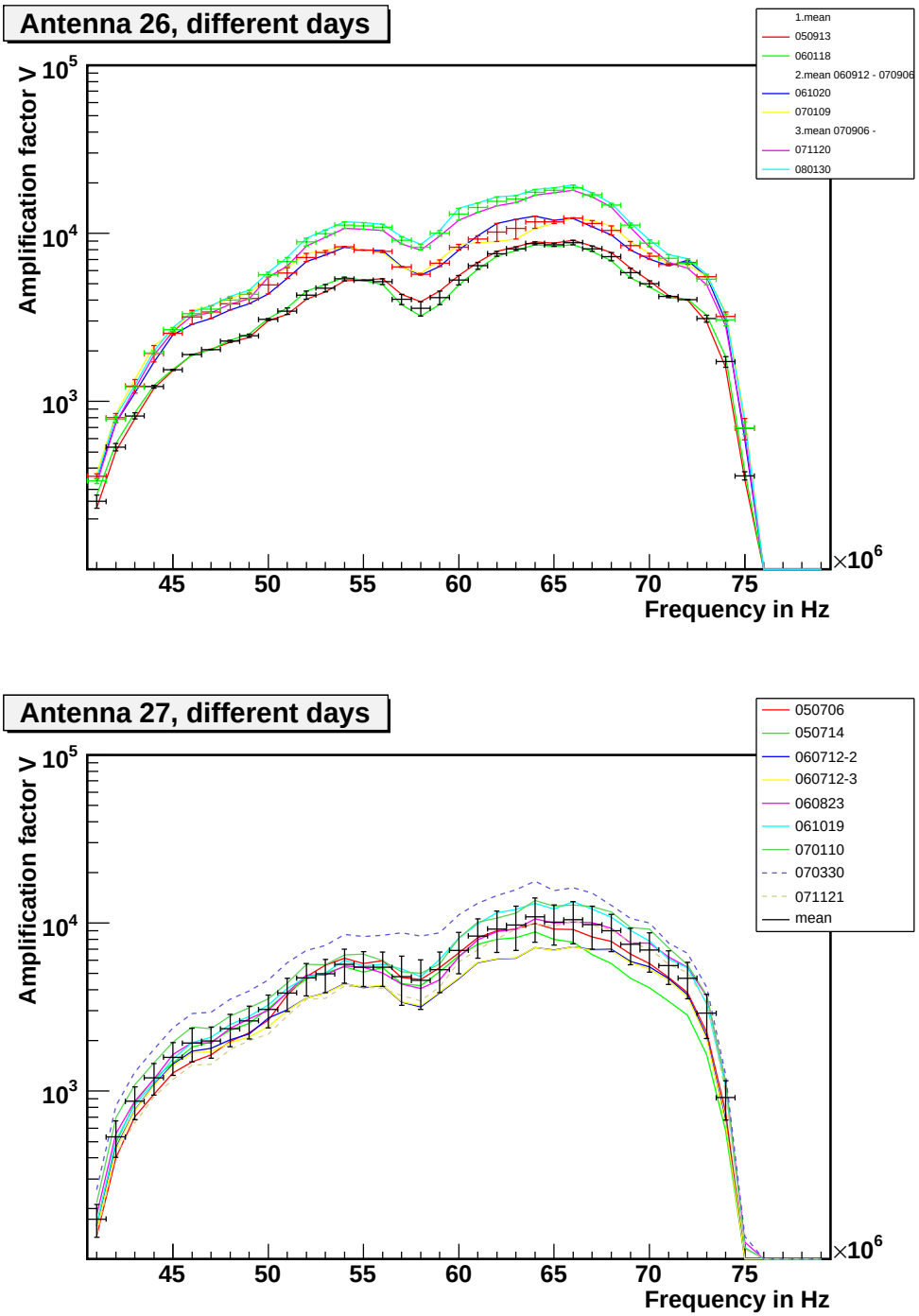

Figure A.14: Up: Amplification factors of antenna #26 from calibration measurements.
48 MHz interpolated.
3 amplification factors!
060912 - back to DAQ, higher amplification factor now.
070906 - delay measurements, higher amplification factor now.
Low: Amplification factors of antenna #27 from calibration measurements.
48 MHz interpolated.
0608xx - mounted as NS polarization at antenna #28.
070330 - bad measurement, maybe like at antenna #3.

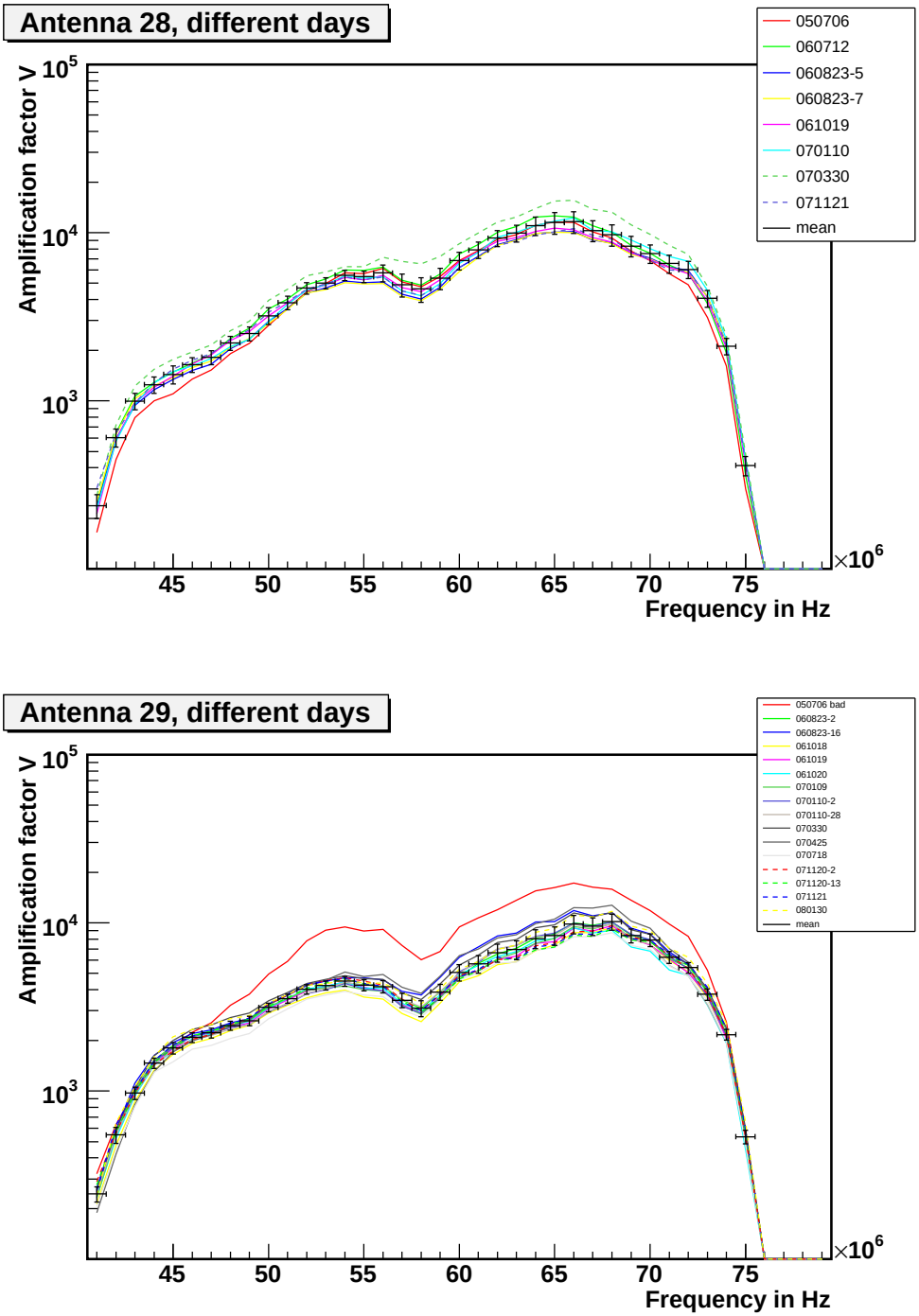

Figure A.15: Up: Amplification factors of antenna #28 from calibration measurements.
Low: Amplification factors of antenna #29 from calibration measurements.
48 MHz and 50 MHz interpolated.
050706 - bad measurement.
0608xx - mounted as NS polarization at antenna #21.

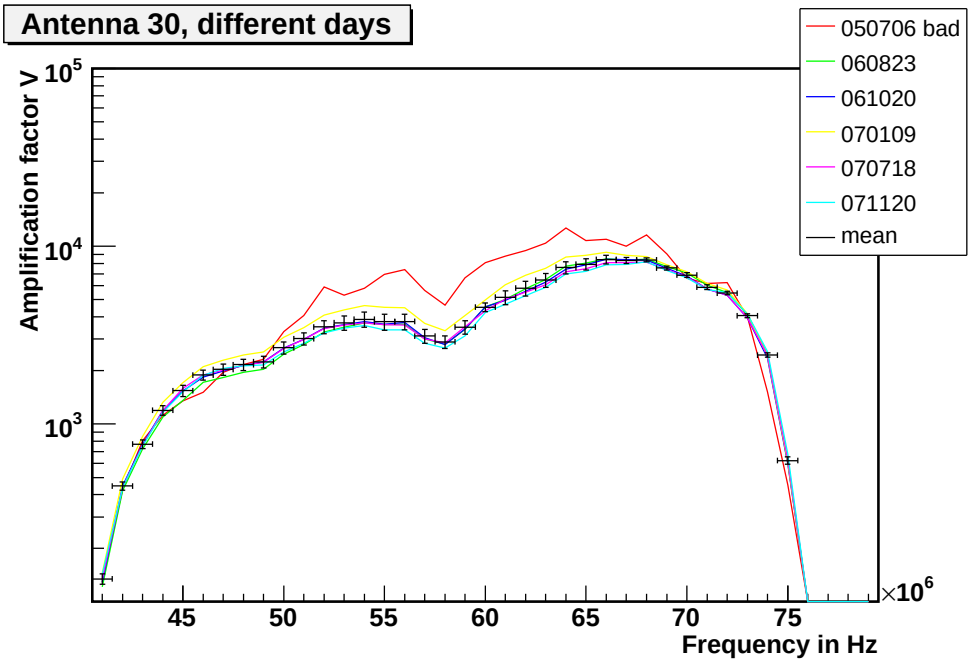

Figure A.16: Amplification factors of antenna #30 from calibration measurements. 48 MHz and 50 MHz interpolated.
050706 - bad measurement.
0608xx - mounted as NS polarization at antenna #22.

B. Radio Emission Lateral Distributions

In this appendix all lateral distributions from the positive detected EAS are shown. There are some events shown, that do not survive the zenith angle cut but their lateral distributions were calculated. The legend boxes in the figures show the EAS parameters (left box) and the fit parameters for the lateral distribution (right box). In the left box the UTC time stamp, the guess primary energy E_g, azimuth angle ϕ, and zenith angle θ are shown. For the right box the χ^2 of the fit, the obtained scale parameter R_0, and the maximum field strength ϵ_0 are shown.

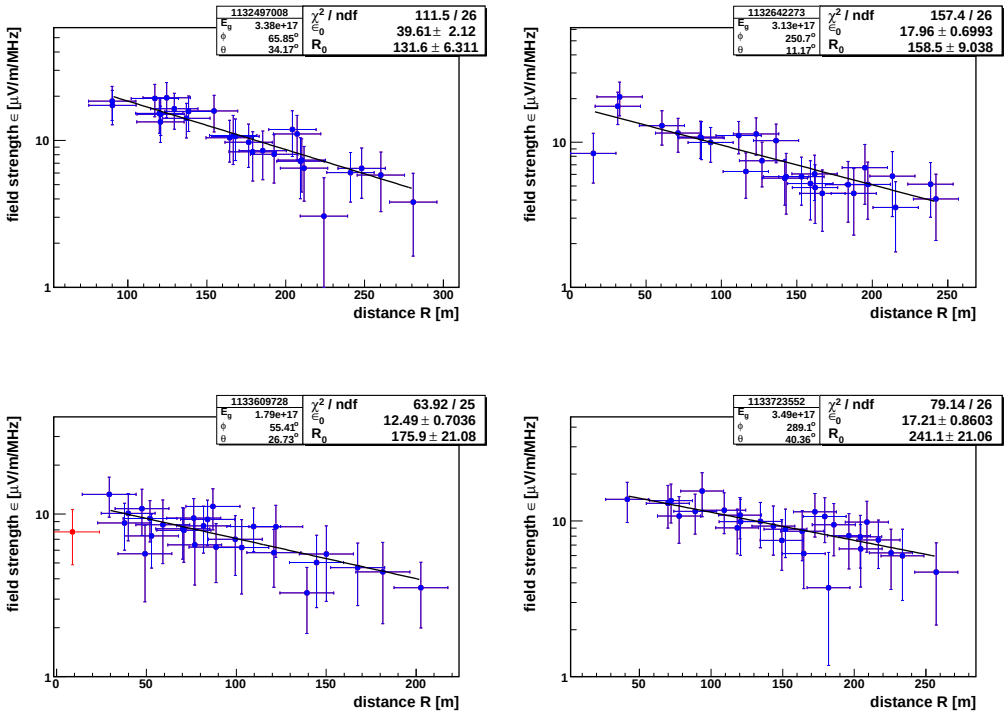

Figure B.1: Lateral distribution of single events

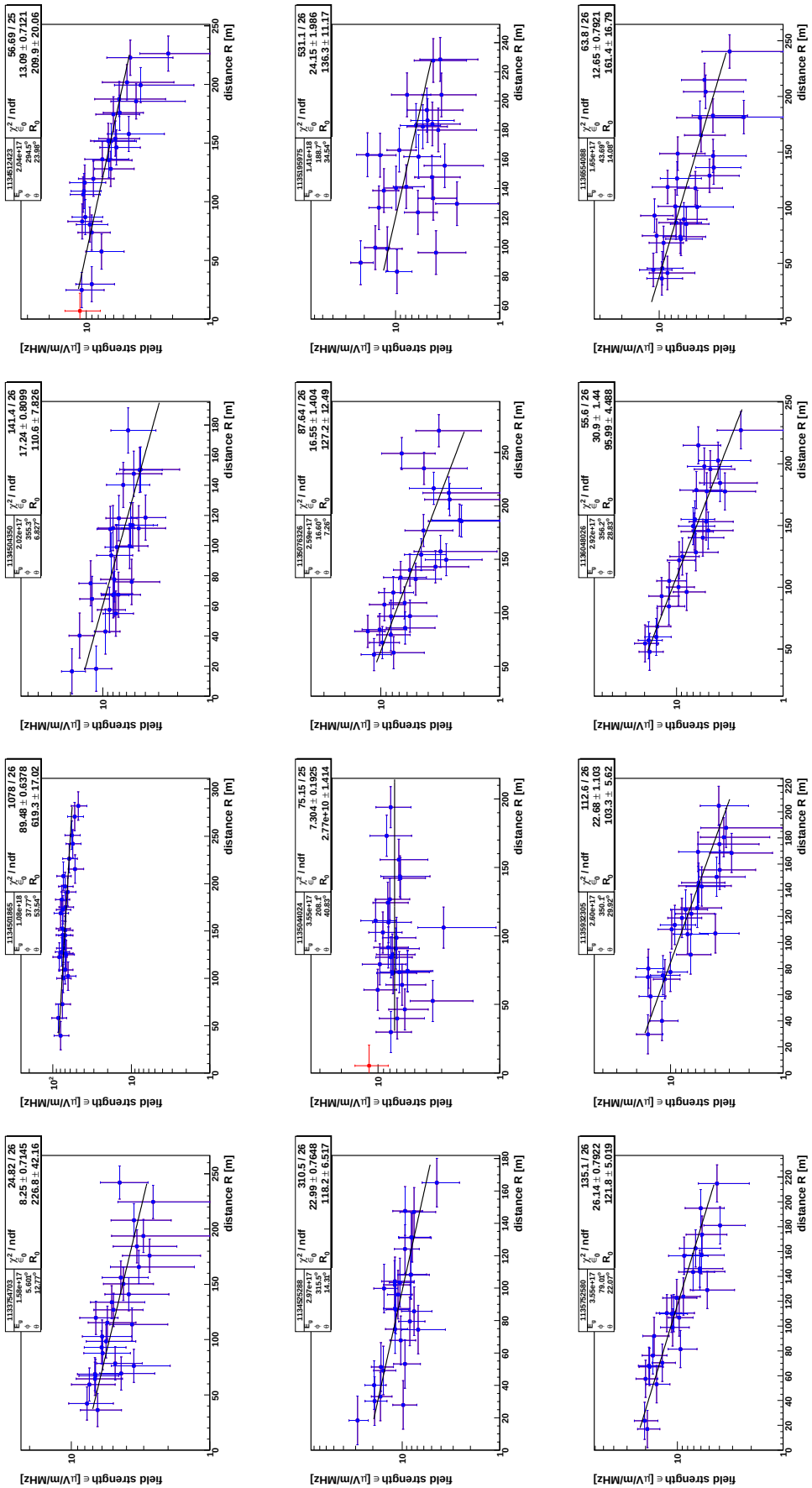

Figure B.2: Lateral distribution of single events

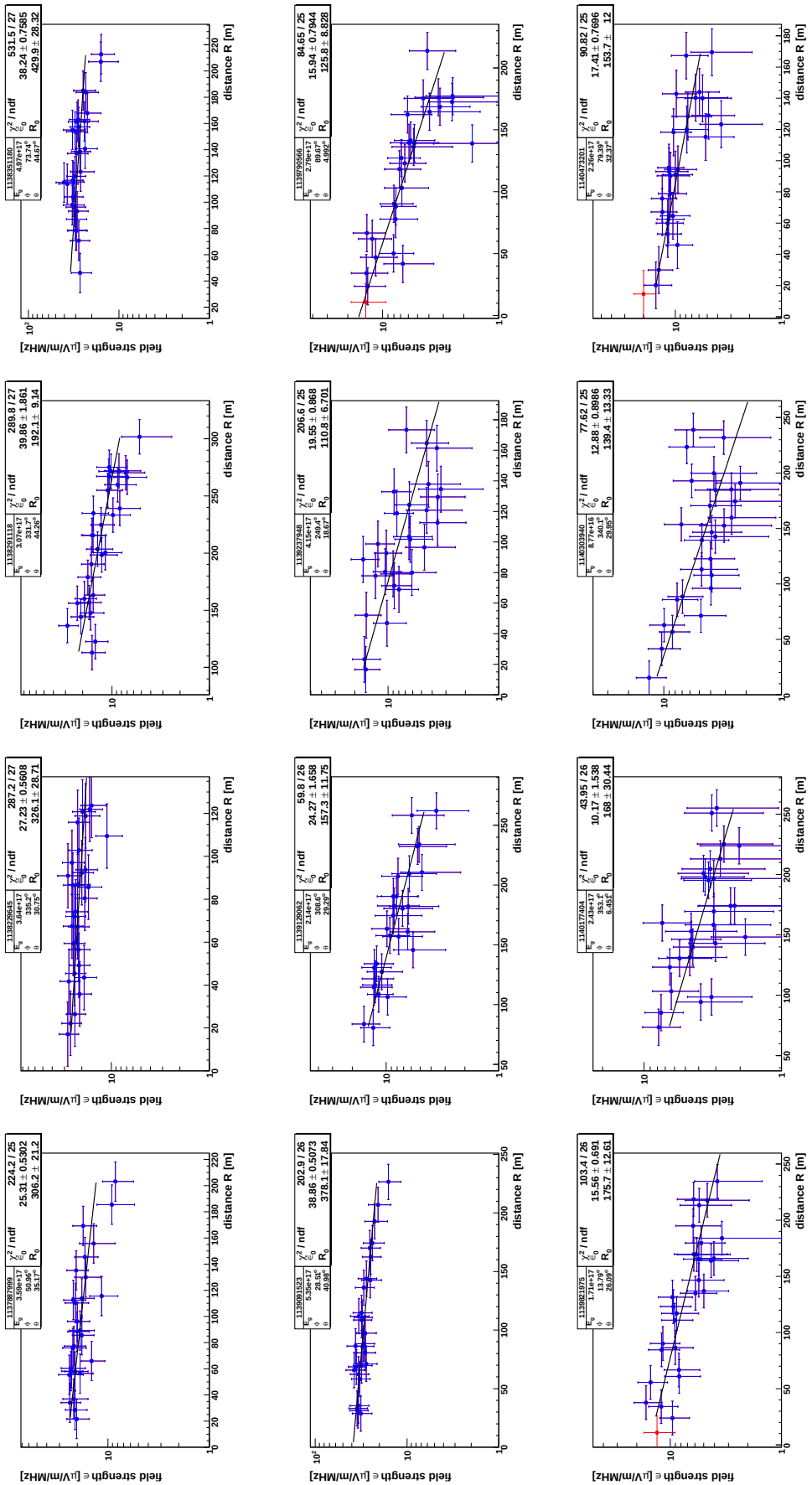

Figure B.3: Lateral distribution of single events

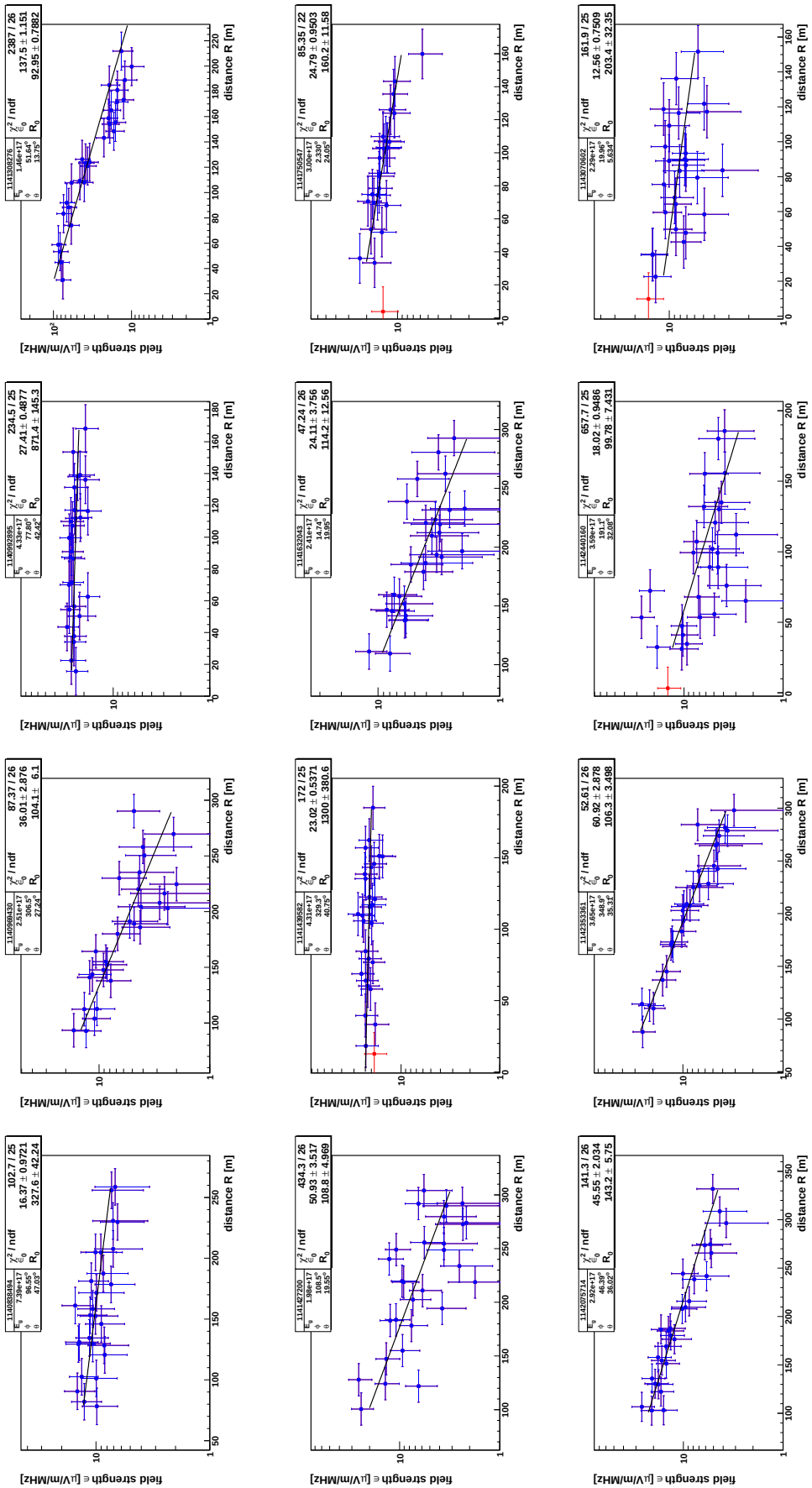

Figure B.4: Lateral distribution of single events

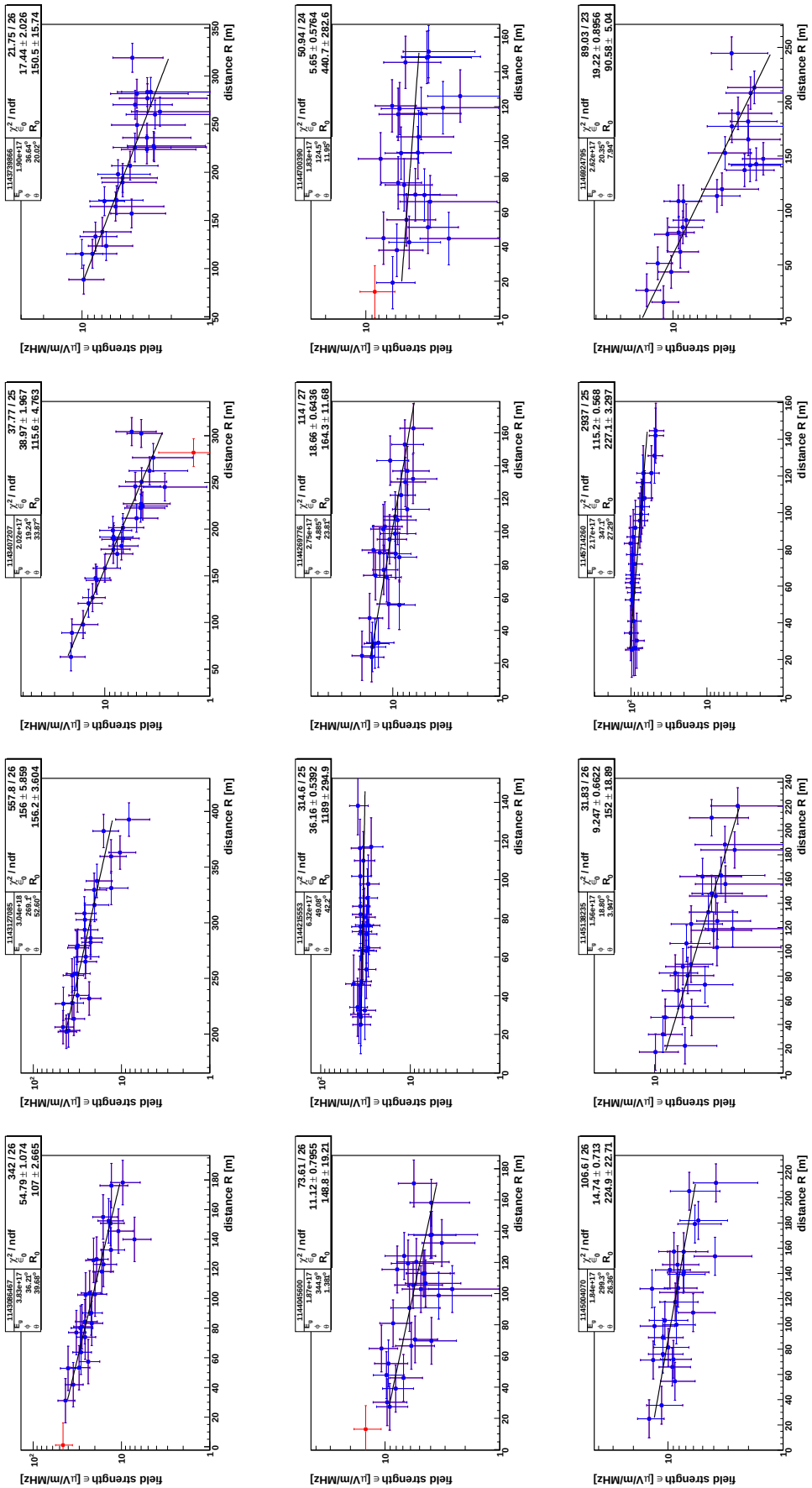

Figure B.5: Lateral distribution of single events

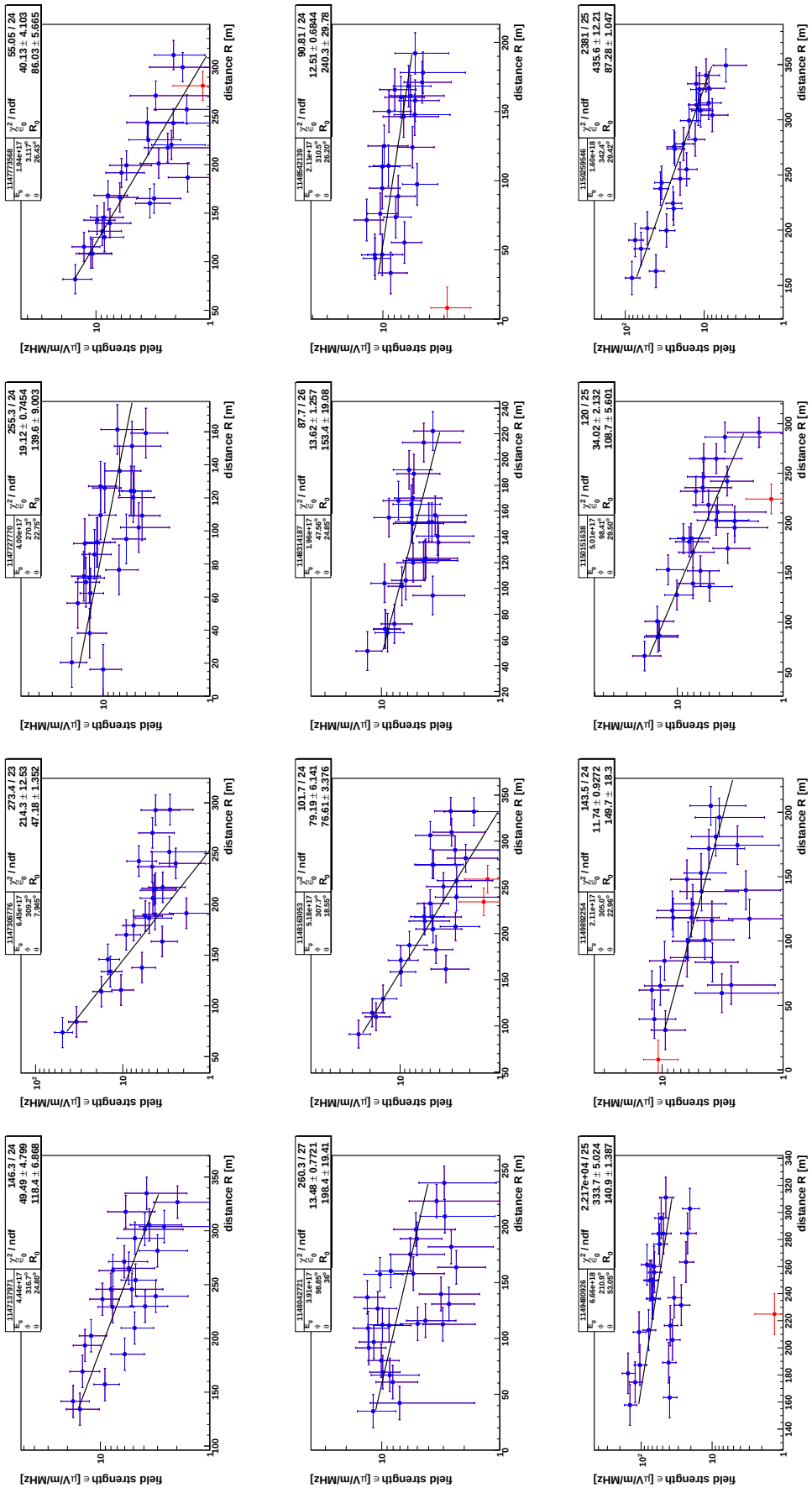

Figure B.6: Lateral distribution of single events

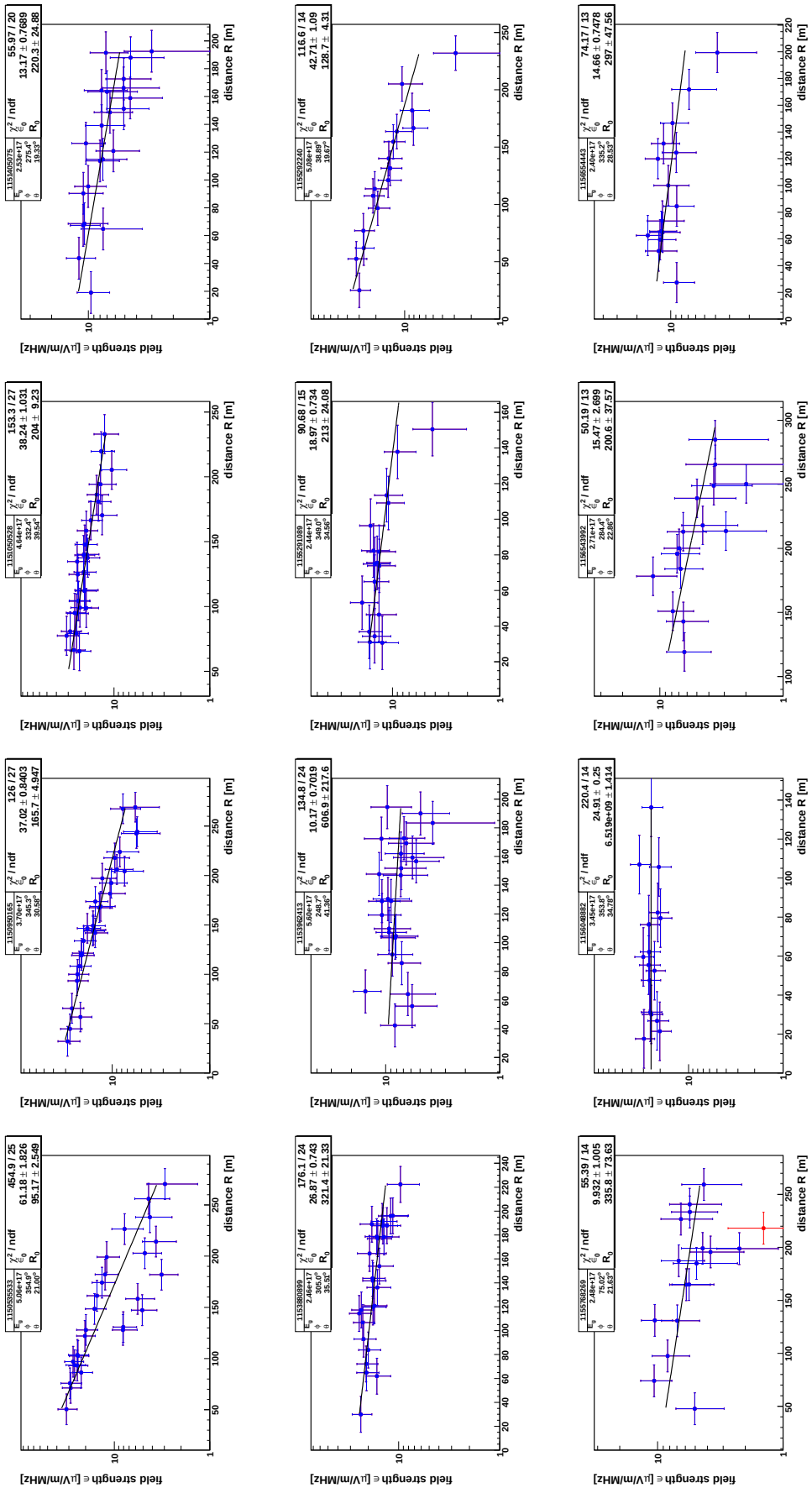

Figure B.7: Lateral distribution of single events

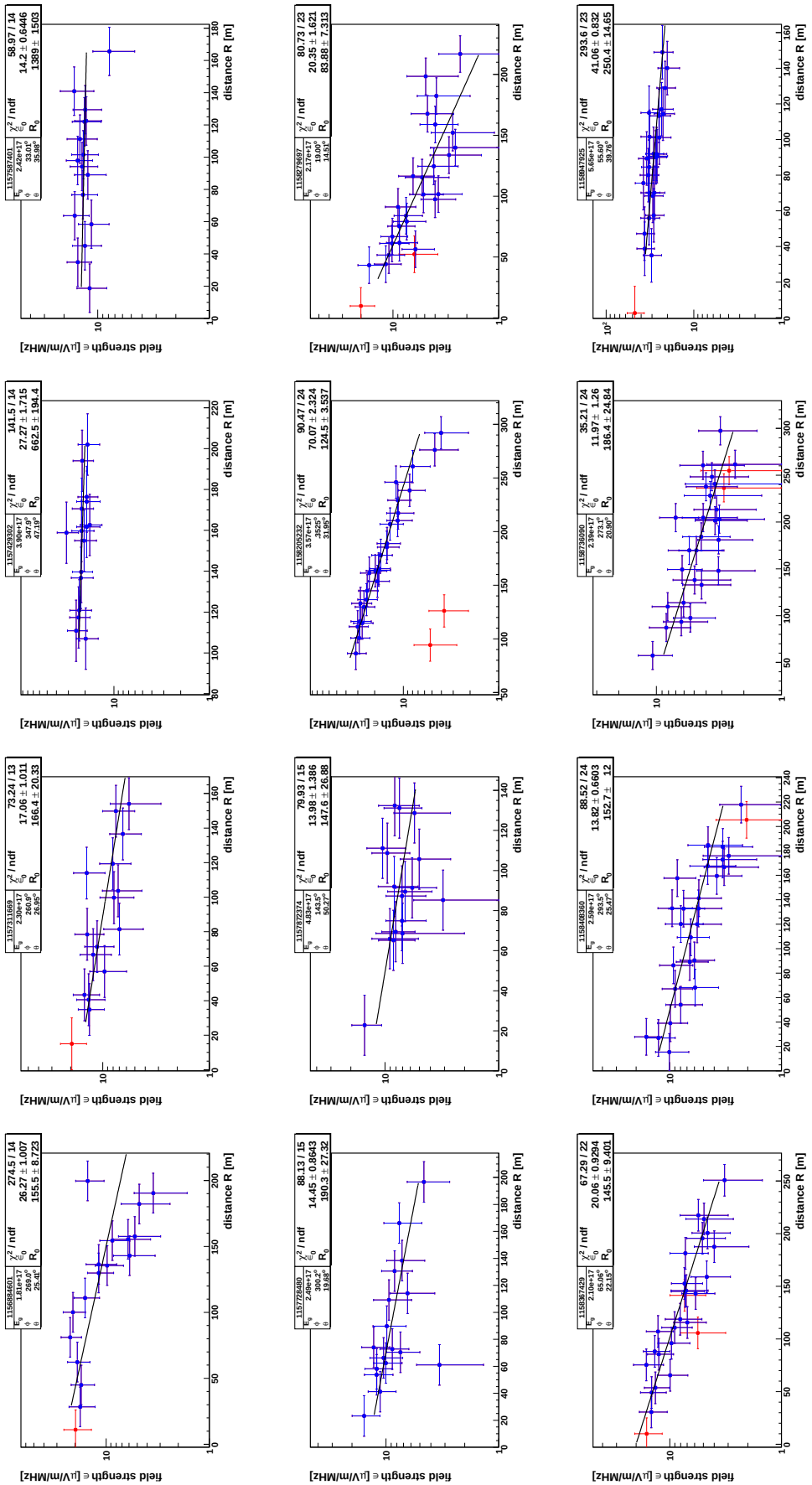

Figure B.8: Lateral distribution of single events

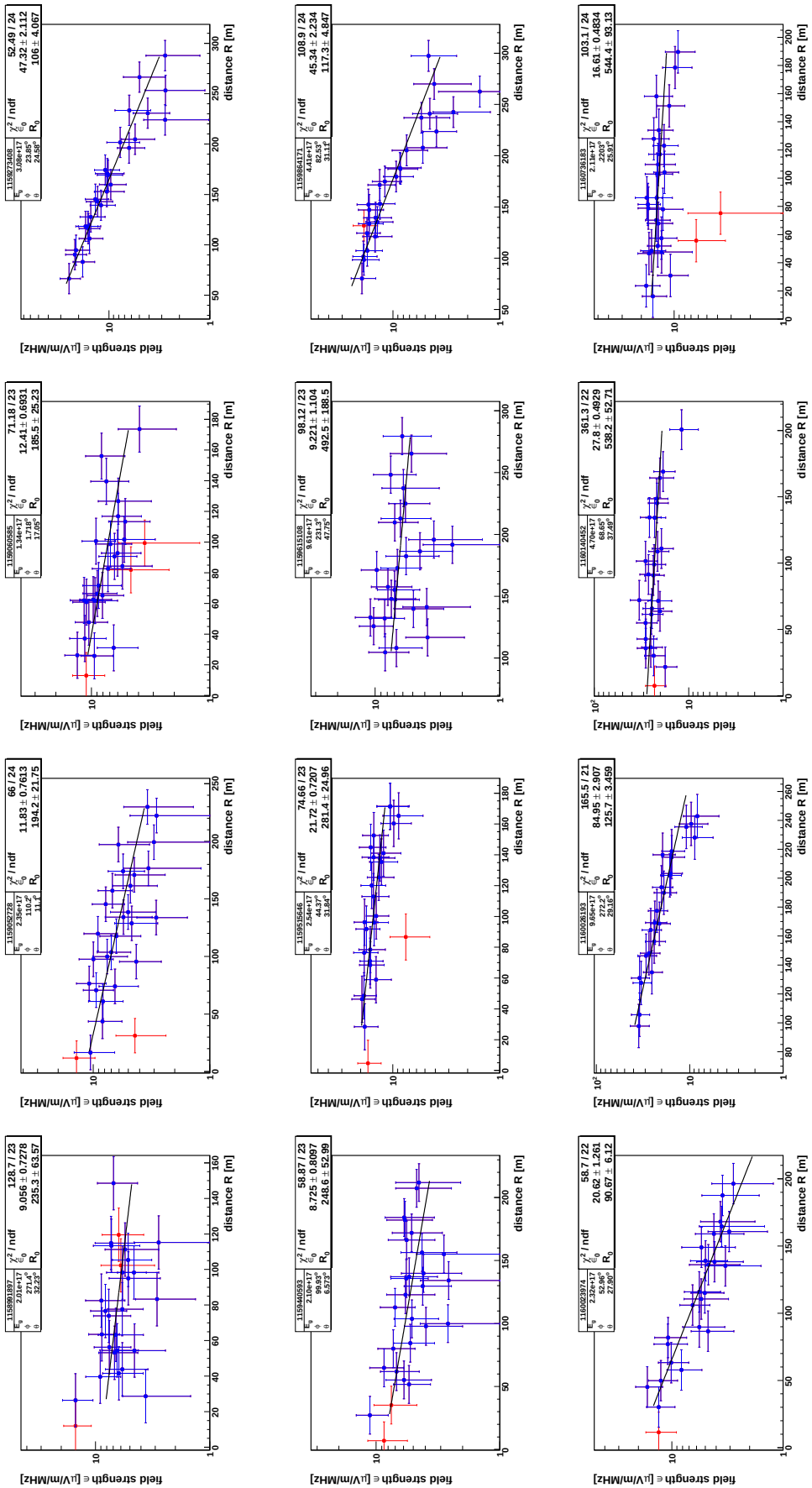

Figure B.9: Lateral distribution of single events

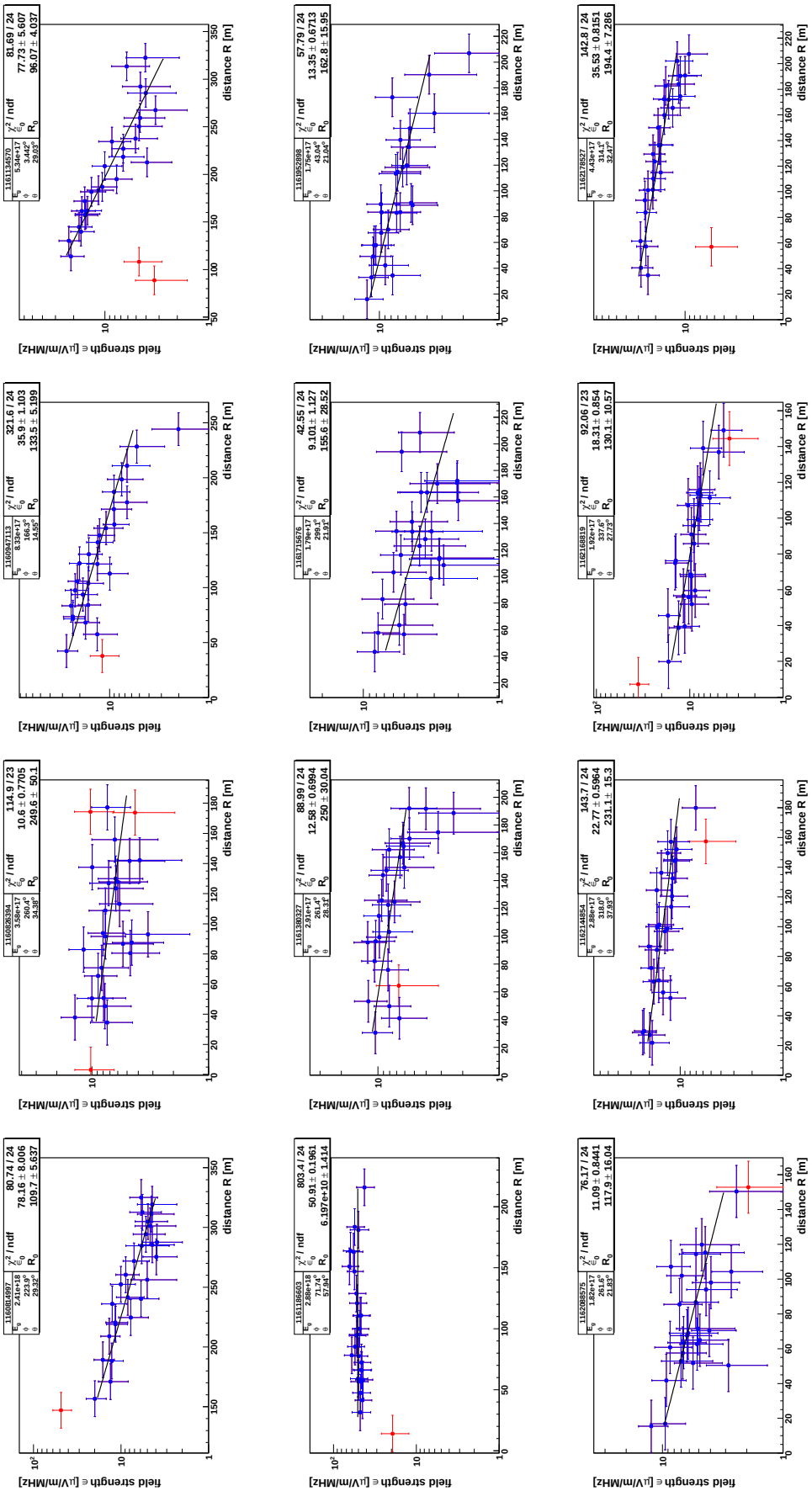

Figure B.10: Lateral distribution of single events

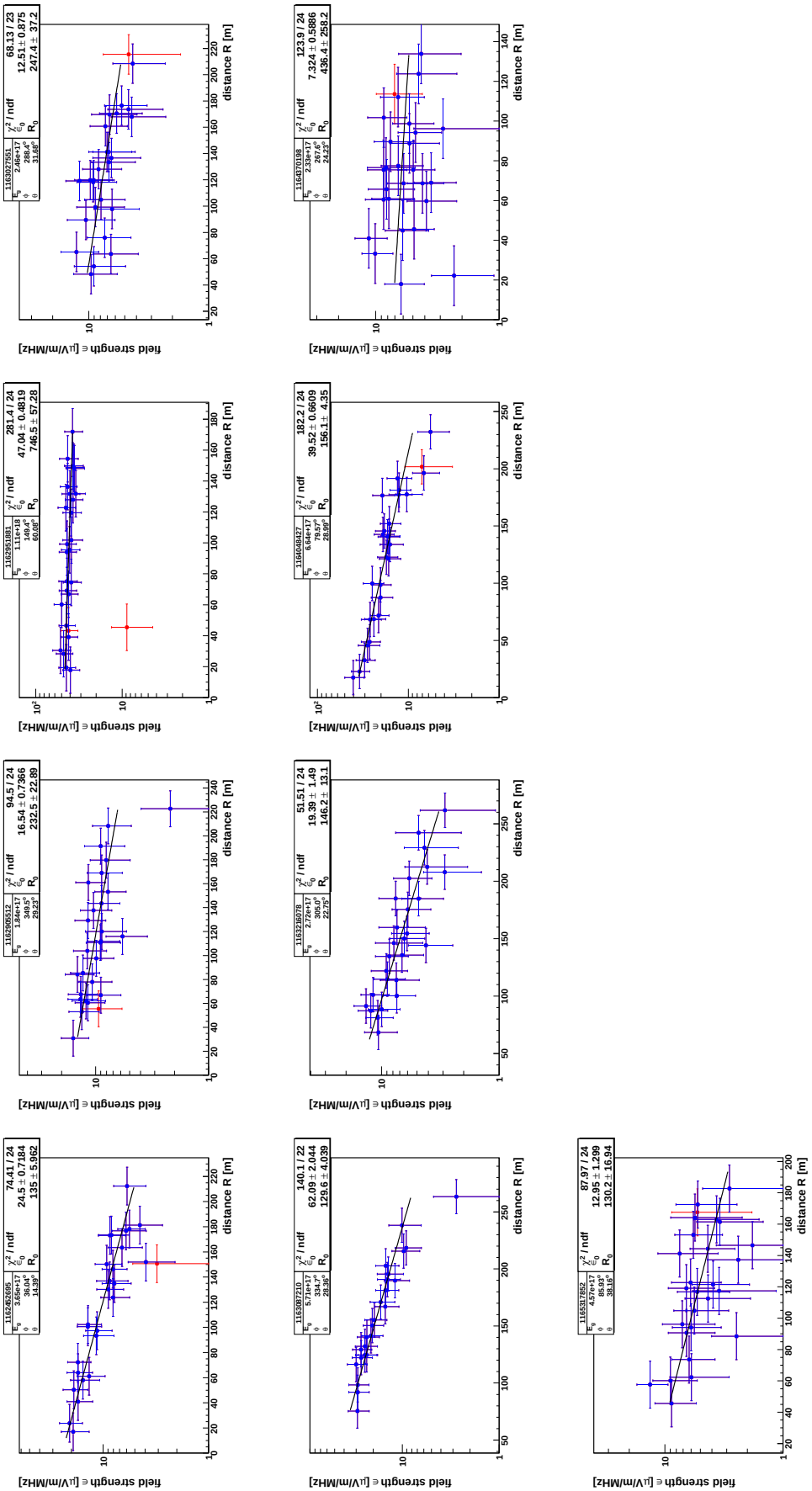

Figure B.11: Lateral distribution of single events

C. Simulation and Data Radio Emission Lateral Distributions

In this appendix exemplarily for some events the direct comparison of simulated with the measured lateral distributions is shown. The legend boxes in the figures show the reconstructed EAS parameters (left box) and the fit parameters for both lateral distributions (right boxes), whereby the upper box gives the results for the measurements (blue) and the lower box for the simulation (red). In the left box the UTC time stamp, the guess primary energy E_g, azimuth angle ϕ, and zenith angle θ are shown. For the right boxes the χ^2 of the fits, the obtained scale parameters R_0, and the maximum field strengths ϵ_0 are shown.

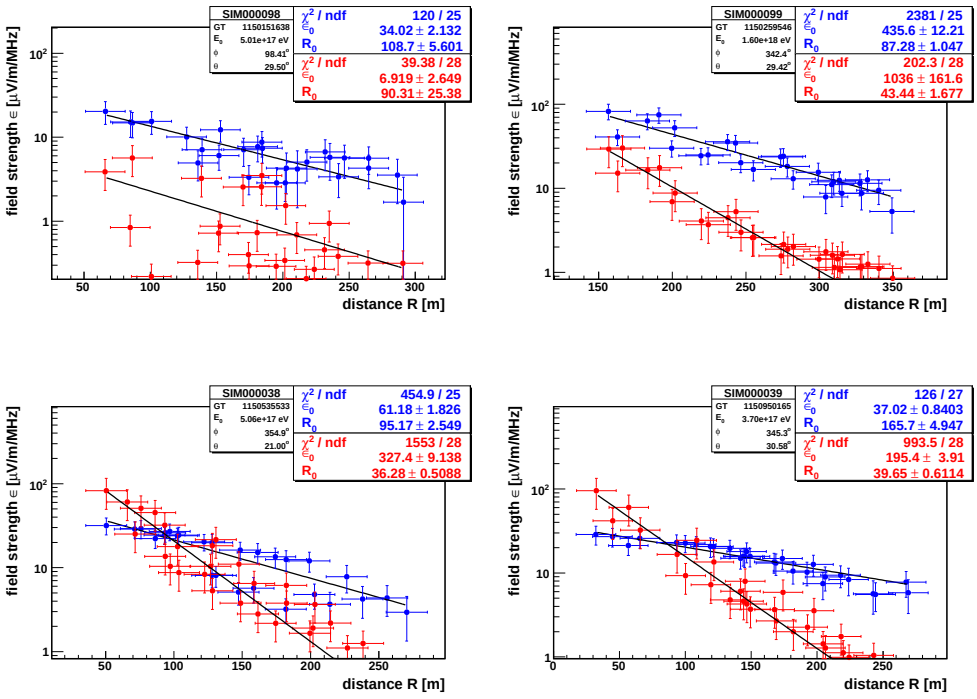

Figure C.1: Lateral distributions data - simulation

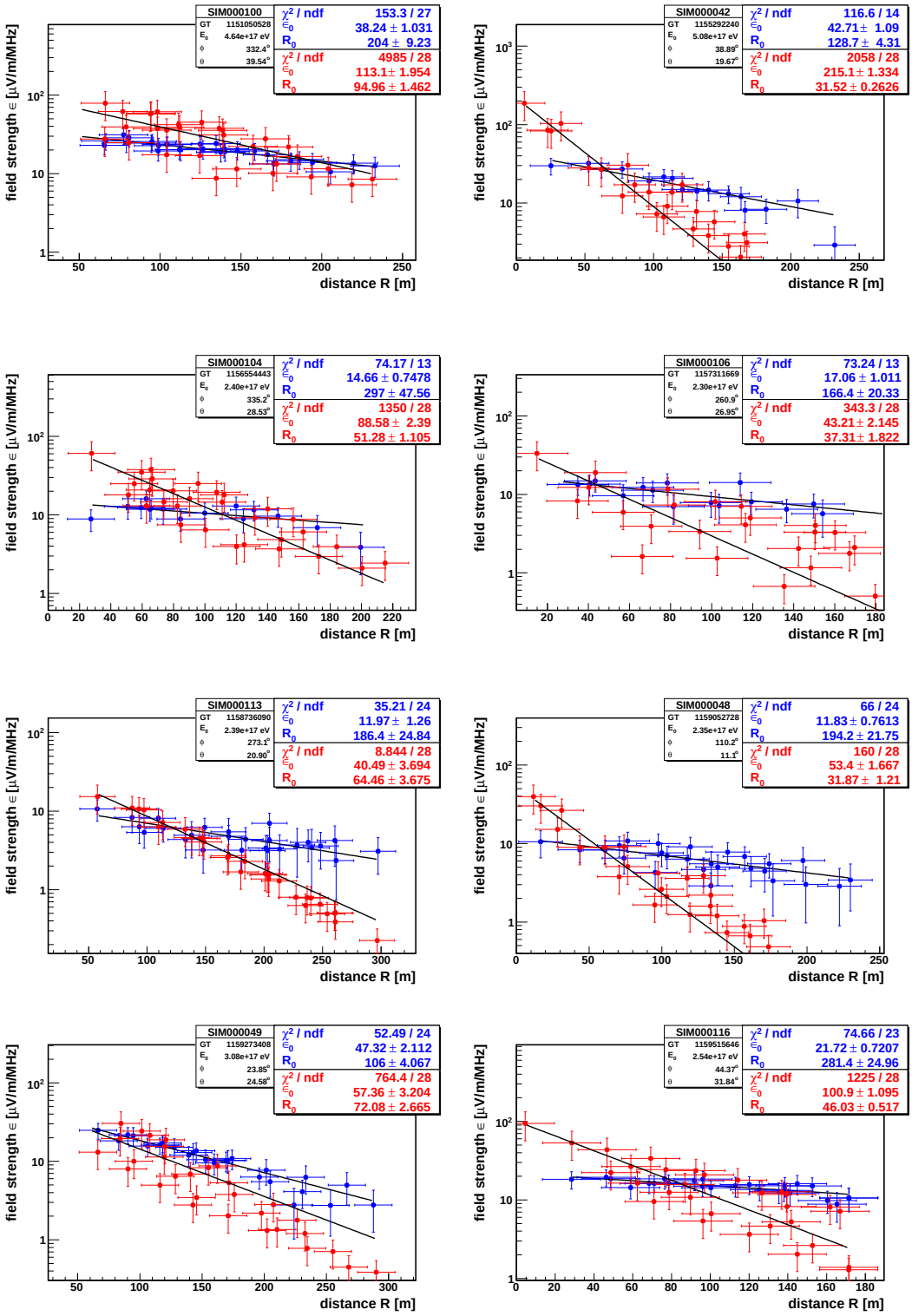

Figure C.2: Lateral distributions data - simulation

Bibliography

Abraham J., Aglietta M., Aguirre I. C., Albrow M., Allard D., Allekotte I., Allison P., Alvarez Mun˜Iz J., Do Amaral M. G., Ambrosio M., Anchordoqui L., Andrews R., Anguiano M., Dos Anjos J. C., et al., 2004, Nuc. Instr. Meth. A, 523, 50

Aharonian F. A., Akhperjanian A. G., Aye K.-M., Bazer-Bachi A. R., Beilicke M., Benbow W., Berge D., Berghaus P., Bernlöhr K., Bolz O., Boisson C., Borgmeier C., Breitling F., Brown A. M., et al., 2004, Nature, 432, 75

AIPS++ consortium 1995-2006, Technical report, AIPS++ Astronomical Information Processing System. , http://aips2.nrao.edu/docs/aips++.html

Allan H. R., 1971, Progress in Elementary Particle and Cosmic Ray Physics, 10, 171

Allen S. W., Schmidt R. W., Fabian A. C., 2002, MNRAS, 334, L11

Antoni T., Apel W. D., Badea A. F., Bekk K., Bercuci A., Blümer J., Bozdog H., Brancus I. M., Chilingarian A., Daumiller K., Doll P., Engel R., Engler J., Feßler F., Gils H. J., Glasstetter R., et al., 2005, Astropart. Phys., 24, 1

Antoni T., Apel W. D., Badea F., Bekk K., Bercuci A., Blümer H., Bozdog H., Brancus I. M., Büttner C., Chilingarian A., Daumiller K., Doll P., Engler J., Feßler F., Gils H. J., et al., 2003, Nuc. Instr. Meth. A, 513, 490

Apel W. D., Asch T., Badea A. F., Bähren L., Bekk K., Bercuci A., Bertaina M., Biermann P. L., Blümer J., Bozdog H., Brancus I. M., et al., 2006, Astropart. Phys., 26, 332

Ardouin D., Bellétoile A., Charrier D., Dallier R., Denis L., Eschstruth P., Gousset T., Haddad F., Lamblin J., Lautridou P., Lecacheux A., Monnier-Ragaigne D., Rahmani A., Ravel O., 2005, Nuc. Instr. Meth. A, 555, 148

Ardouin D., Bellétoile A., Charrier D., Dallier R., Denis L., Eschstruth P., Gousset T., Haddad F., Lamblin J., Lautridou P., Lecacheux A., Monnier-Ragaigne D., Ravel O., Saugrin T., Valcares S., 2006, Astropart. Phys., 26, 341

Askar'yan G. A., 1962, Soviet Journal of Experimental and Theoretical Physics, 14, 441

Askar'yan G. A., 1965, Soviet Journal of Experimental and Theoretical Physics, 21, 658

Atrashkevich V. B., Vedeneev O. V., Allan H. R., et al., 1978, Soviet Journal of Nuclear Physics, 28, 366

Auger P., Ehrenfest P., Maze R., Daudin J., Fréon R. A., 1939, Rev. Mod. Phys., 11, 288

Axford W. I., Leer E., Skadron G., 1977, in Proc. 15^{th} Int. Cosmic Ray Conf. Vol. 11 of International Cosmic Ray Conference, The Acceleration of Cosmic Rays by Shock Waves. pp 132–+

Barwick S. W., Beatty J. J., Besson D. Z., Clem J. M., Coutu S., DuVernois M. A., Evenson P. A., Gorham P. W., Halzen F. L., Jacobson A., Kieda D., Learned J. G., Liewer K. M., et al., 2003, in Gorham P. W., ed., Particle Astrophysics Instrumentation. Edited by Peter W. Gorham. Proceedings of the SPIE, Volume 4858, pp. 265-276 (2003). Vol. 4858 of Presented at the Society of Photo-Optical Instrumentation Engineers (SPIE) Conference, Overview of the ANITA project. pp 265–276

Beck R., Brandenburg A., Moss D., Shukurov A., Sokoloff D., 1996, ARA&A, 34, 155

Bell A. R., 1978, MNRAS, 182, 147

Bell A. R., 1992, MNRAS, 257, 493

Benjamin J., Heymans C., Semboloni E., van Waerbeke L., Hoekstra H., Erben T., Gladders M. D., Hetterscheidt M., Mellier Y., Yee H. K. C., 2007, MNRAS, 381, 702

Berezhko E. G., 2008, Advances in Space Research, 41, 429

Bergmann T., Engel R., Heck D., Kalmykov N. N., Ostapchenko S., Pierog T., Thouw T., Werner K., 2007, Astropart. Phys., 26, 420

Bernlöhr K., Carrol O., Cornils R., Elfahem S., Espigat P., Gillessen S., Heinzelmann G., Hermann G., Hofmann W., Horns D., Jung I., Kankanyan R., Katona A., Khelifi B., Krawczynski H., et al., 2003, Astropart. Phys., 20, 111

Blandford R. D., Ostriker J. P., 1978, ApJL, 221, L29

Buitink S., Apel W. D., Asch T., Badea F., Böhren L., Bekk K., Bercuci A., Bertaina M., Biermann P. L., Blümer J., Bozdog H., Brancus I. M., Brüggemann M., Buchholz P., et al., 2007, A&A, 467, 385

Bürger J., Böhm E., Suling M., 1975, in Proc. 14^{th} Int. Cosmic Ray Conf. Vol. 8 of International Cosmic Ray Conference, Energy Spectra and Production Height of Muons in EAS. pp 2784–+

Chiba M., Kamijo T., Kawaki M., Husain A., Inuzuka M., Ikeda M., Yasuda O., 2001, in Saltzberg D., Gorham P., eds, Radio Detection of High Energy Particles Vol. 579 of American Institute of Physics Conference Series, Study of Salt Neutrino Detector. pp 204–+

Dulk G. A., Erickson W. C., Manning R., Bougeret J.-L., 2001, A&A, 365, 294

F. Hess V., 1912, Physikalische Zeitschrift, 13, 1084

Falcke H., Apel W. D., Badea A. F., Bähren L., Bekk K., Bercuci A., Bertaina M., Biermann P. L., Blümer J., Bozdog H., Brancus I. M., Buitink S., Brüggemann M., Buchholz P., Butcher H., et al., 2005, Nature, 435, 313

Friis H. T., 1946, Proceedings of the Institute of Radio Engineers - Proc. IRE, 34, 254

Gaisser T. K., Hillas A. M., 1977, in Proc. 15^{th} Int. Cosmic Ray Conf. Vol. 8 of International Cosmic Ray Conference, Reliability of the Method of Constant Intensity Cuts for Reconstructing the Average Development of Vertical Showers. pp 353–+

Gemmeke H., Apel W. D., Badea F. A., Bähren L., Bekk K., Bercuci A., Bertaina M., Biermann P. L., Blümer J., Bozdog H., Brancus I. M., Brüggemann M., Buchholz P., Buitink S., Butcher H., et al., 2006, International Journal of Modern Physics A, 21, 242

Giller M., Lipski M., 2002, Journal of Physics G Nuclear Physics, 28, 1275

Glasstetter R., et al., 2005, in Proc. 29^{th} Int. Cosmic Ray Conf. Vol. 6 of International Cosmic Ray Conference, Shower Size Reconstruction at KASCADE-Grande. pp 293–+

Greisen K., 1956, Prog. Cosmic Ray Physics, 3

Greisen K., 1966, Physical Review Letters, 16, 748

Gunn J. E., Ostriker J. P., 1969, Physical Review Letters, 22, 728

Hakenjos A., 2006, Forschungszentrum Karlsruhe Report - FZKA, 7219

Haungs A., Rebel H., Roth M., 2003, Reports of Progress in Physics, 66, 1145

Hazen W. E., Hendel A. Z., Smith H., Shah N. J., 1969, Physical Review Letters, 22, 35

Heck D., Knapp J., Capdevielle J. G., Schatz G., Thouw T., 1998, Forschungszentrum Karlsruhe Report - FZKA, 6019

Hillas A. M., 1984, ARA&A, 22, 425

Horneffer A., Antoni T., Apel W. D., Badea F., Bekk K., Bercuci A., Bertaina M., Blümer H., Bozdog H., Brancus I. M., Brüggemann M., Buchholz P., Büttner C., Chiavassa A., et al., 2004, in Hough J., Sanders G. H., eds, Gravitational Wave and Particle Astrophysics Detectors. Edited by Hough, James; Sanders, Gary H. Proceedings of the SPIE, Volume 5500, pp. 129-138 (2004). Vol. 5500 of Presented at the Society of Photo-Optical Instrumentation Engineers (SPIE) Conference, LOPES: detecting radio emission from cosmic ray air showers. pp 129–138

Horneffer A., et al., 2007, in Proc. 30^{th} Int. Cosmic Ray Conf. International Cosmic Ray Conference, Primary Particle Energy Calibration of the EAS Radio Pulse Height

Huege T., Falcke H., 2003, A&A, 412, 19

Huege T., Falcke H., 2005a, A&A, 430, 779

Huege T., Falcke H., 2005b, Astropart. Phys., 24, 116

Huege T., Ulrich R., Engel R., 2007a, Journal of Physics Conference Series, 81, 2002

Huege T., Ulrich R., Engel R., 2007b, Astropart. Phys., 27, 392

Huege T., Ulrich R., Engel R., 2007c, ArXiv 0707.3763, 707

Jackson J. D., 1975, Classical Electrodynamics. 92/12/31, New York: Wiley, 1975, 2nd ed.

Jelley J. V., Fruin J. H., Porter N. A., Weekes T. C., Smith F. G., Porter R. A., 1965, Nature, 205, 327

Jones W. V., 2005, in Proc. 29^{th} Int. Cosmic Ray Conf. Vol. 10 of International Cosmic Ray Conference, Evolution of scientific research ballooning. pp 173–+

Kahn F. D., Lerche I., 1966, Royal Society of London Proceedings Series A, 289, 206

Kalmykov N. N., Konstantinov A. A., Engel R., 2006, Nuclear Physics B (Proceedings Supplements), 151, 347

Kamata K., Nishimura J., 1958, Prog. Theoret. Phys. Suppl., 6, 93

KASCADE Collaboration Antoni T., Apel W. D., Badea F., Bekk K., Bernlöhr K., Blümer H., Bollmann E., Bozdog H., Brancus I. M., Büttner C., Chilingarian A., Daumiller K., et al., 2002, Astropart. Phys., 16, 245

Keilhauer B., Blümer J., Engel R., Klages H. O., 2006, Astropart. Phys., 25, 259

Klypin A., Zhao H., Somerville R. S., 2002, ApJ, 573, 597

Knop R. A., Aldering G., Amanullah R., Astier P., Blanc G., Burns M. S., Conley A., Deustua S. E., Doi M., Ellis R., Fabbro S., Folatelli G., Fruchter A. S., Garavini G., Garmond S., Garton K., et al., 2003, ApJ, 598, 102

Kobayakawa K., Honda Y. S., Samura T., 2002, Phys. Rev. D, 66, 083004

Kravchenko I., Cooley C., Hussain S., Seckel D., Wahrlich P., Adams J., Churchwell S., Harris P., Seunarine S., Bean A., Besson D., Graham S., Holt S., Marfatia D., McKay D., Meyers J., et al., 2006, Phys. Rev. D, 73, 082002

Krömer O., 2008, Forschungszentrum Karlsruhe Report - FZKA, 7396

Krymskii G. F., 1977, Akademiia Nauk SSSR Doklady, 234, 1306

Kulikov G. V., Khristiansen G. B., 1958, Sov. J. JETP, 35, 441

Le Monnier L.-G., 1752, Memoires de l'Academie des Sciences, 2, 233

LOPES Collaboration Apel W. D., Asch T., Badea A. F., Bähren L., Bekk K., Bercuci A., Bertaina M., Biermann P. L., Blümer J., Bozdog H., Brancus I. M., Buitink S., Brüggemann M., et al., 2006, Astropart. Phys., 26, 332

Lord Kelvin S., 1889, Mathematics and Physics, 3, 491

Maus S., Macmillan S., 2005, EOS Transactions, 86, 159

Molière G., 1947, Z. Naturforsch., 2a, 133

Molière G., 1948, Z. Naturforsch., 3a, 78

Navarra G., Antoni T., Apel W. D., Badea F., Bekk K., Bercuci A., Bertaina M., Blümer H., Bozdog H., Brancus I. M., Brüggemann M., Buchholz P., Büttner C., Chiavassa A., Doll P., Engel R., et al., 2004, Nuc. Instr. Meth. A, 518, 207

Nehls S., Hakenjos A., Arts M. J., Blümer J., Bozdog H., van Cappellen W. A., Falcke H., Haungs A., Horneffer A., Huege T., Isar P. G., Krömer O., 2008, Nuc. Instr. Meth. A, 589, 350

Nigl A., Zarka P., Kuijpers J., Falcke H., Bähren L., Denis L., 2007, A&A, 471, 1099

Penzias A. A., Wilson R. W., 1965, ApJ, 142, 419

Petrovic J., Apel W. D., Asch T., Badea F., Bähren L., Bekk K., Bercuci A., Bertaina M., Biermann P. L., Blümer J., Bozdog H., Brancus I. M., Brüggemann M., Buchholz P., Buitink S., Butcher H., et al., 2007, A&A, 462, 389

Ptuskin V. S., Rogovaya S. I., Zirakashvili V. N., Chuvilgin L. G., Khristiansen G. B., Klepach E. G., Kulikov G. V., 1993, A&A, 268, 726

Rohlfs K., 1986, Tools of Radio Astronomy. Berlin and New York, Springer-Verlag, 1986, 332 p.

Rottgering H. J. A., Braun R., Barthel P. D., van Haarlem M. P., Miley G. K., Morganti R., Snellen I., Falcke H., de Bruyn A. G., Stappers R. B., Boland W. H. W. M., Butcher H. R., de Geus E. J., et al., 2006, ArXiv astro-ph/0610596

Satyapal S., Vega D., Dudik R. P., Abel N. P., Heckman T., 2008, ApJ, 677, 926

Schödel R., Ott T., Genzel R., Hofmann R., Lehnert M., Eckart A., Mouawad N., Alexander T., Reid M. J., Lenzen R., Hartung M., Lacombe F., Rouan D., Gendron E., Rousset G., Lagrange A.-M., et al., 2002, Nature, 419, 694

Scholten O., Werner K., Rusydi F., 2008, Astropart. Phys., 29, 94

Semikoz D. V., et al., 2007, ArXiv 0706.2960

Spergel D. N., Bean R., Doré O., Nolta M. R., Bennett C. L., Dunkley J., Hinshaw G., Jarosik N., Komatsu E., Page L., Peiris H. V., Verde L., Halpern M., Hill R. S., Kogut A., Limon M., Meyer S. S., Odegard N., et al., 2007, ApJS, 170, 377

Sveshnikova L. G., 2003, A&A, 409, 799

The Pierre AUGER Collaboration Abraham J., Abreu P., Aglietta M., Aguirre C., Allard D., Allekotte I., et al., 2008, Astropart. Phys., 29, 188

van Buren J., et al., 2005, in Proc. 29^{th} Int. Cosmic Ray Conf. Vol. 6 of International Cosmic Ray Conference, Muon Size Spectrum measured by KASCADE-Grande. pp 301–+

Zatsepin G. T., Kuz'min V. A., 1966, Soviet Journal of Experimental and Theoretical Physics Letters, 4, 78